

https://dspace.org/

Development of a carbon fibre swingarm

Smith, Bevan Ian

2014-09-03
http://hdl.handle.net/10539/15370

Downloaded from a DSpace repository. https://dspace.org/

Development of a Carbon Fibre Swingarm

Bevan Ian Smith

A research report submitted to the Faculty of Engineering and the Built Environment, of the University of the Witwatersrand, in partial fulfilment of the requirements for the degree of Master of Science in Engineering.

Johannesburg 2013

DECLARATION

I declare that this research report is my own unaided work. It is being submitted to the Degree of Master of Science to the University of the Witwatersrand, Johannesburg. It has not been submitted before for any degree or examination to any other University.

……

(Signature of Candidate)

…….. day of ……., ……

(day) (month) (year)

ABSTRACT

Carbon fibre has not been extensively used in the development of motorcycle swingarms. This study investigates the development of a carbon fibre swingarm with an emphasis on the structural integrity and on developing a finite element model (FEM).

The motorcycle swingarm is a critical component in the rear part of the motorcycle. The literature shows that swingarms need to be strong enough to handle various loads experienced in the field, stiff enough to increase motorcycle response and stability, and light enough to improve motorcycle performance and reduce the rear unsprung mass. To this end carbon fibre was used in the design of a swingarm for a Ducati 1098 motorcycle due to its high stiffness and strength to weight ratios. The current research presents the first step in the design process of a single-sided carbon fibre swingarm.

A test rig was developed for testing the stiffness and strength of swingarms. Vertical, lateral and torsional stiffness values of 500 kN/m, 445 kN/m and 550 Nm/deg respectively, were determined from deflection measurements. The lateral and torsional stiffness values are on the lower spectrum of stiffness values when compared with swingarms measured in the literature which suggests the swingarm will exhibit a sluggish response and reduced weave mode stability at medium to high speeds. To determine the strength, strains were measured on the swingarm. Maximum strain values of 1100 με were measured which are considerably lower than the ultimate strain of 8000 με for the material which indicates the swingarm is strong enough.

Furthermore, a finite element (FE) model was developed so that later design iterations could be completed more quickly and cheaply. The FE model showed good correlation with the vertical displacement results (difference ≈ 4%); the torsional deflection difference was approximately 28% and the lateral deflection difference, 50%. The experimental lateral loading used was 133 N, resulting in a displacement of 0.3 mm as compared to the experimental vertical loading used which was 8000 N, resulting in a displacement of 16.5 mm. The error due to lash and bedding in which is plausibly in the region of 0.15 mm is likely the cause of the poor correlation between

the measured and FE lateral deflection results. The strains calculated by the FE model showed both good (less than 10% difference) and poor (larger than 100% difference) correlation. Plausible reasons for the poor correlation results were determined to be largely due to the influence of ply overlap and to a lesser extent, gauge misalignment and gauge placement accuracy. The first iteration of the prototype carbon fibre swingarm is 1.5 kg lighter than the original aluminium swingarm. Future work will look to improve the stiffness of future swingarm designs using the FE model.

ACKNOWLEDGEMENTS

I would like to thank Dr Frank Kienhöfer for his supervising this project. He was always available to see me when I needed guidance. He also did his utmost to provide me with all the necessary tools to complete this project.

Thank you to Mr Jarryd Deiss for greatly assisting me in the setup of the swingarm for testing.

To my wife Lanie, thank you for always believing in me.

And to those gentlemen who choose to remain anonymous, thank you for your immense help.

Thank You Lord Jesus for everything and all things.

TABLE OF CONTENTS

DECLARATION i

ABSTRACT ii

ACKNOWLEDGEMENTS iv

LIST OF FIGURES viii

LIST OF TABLES xiv

LIST OF SYMBOLS xv

LIST OF ACRONYMS xvi

1. INTRODUCTION 1

1.1 Background 1

1.2 The Motorcycle Swingarm 2

1.3 Composite Materials 5

1.4 Project Overview 7

2. LITERATURE REVIEW 10

2.1 Automotive Test Rig Development 10

2.2 Swingarm Development 12

2.3 Leyni Durability Test 18

2.4 Experimental Strain Measurements on Composites 18

2.5 Finite Element Analysis on Composites 20

3. OBJECTIVES 21

4. METHODOLOGY 22

4.1 Experimental Equipment and Instrumentation 22

4.2 Experimental Rig Setup and Loading – Vertical Testing 27

4.3 Experimental Rig Setup and Loading – Torsional Testing 27

4.4 Experimental Rig Setup and Loading – Lateral Testing 32

4.5 Development of the Finite Element Model 33

4.5.1 Software 34
4.5.2 Assumptions 34
4.5.3 Model Preparation and Mesh Generation 36
4.5.4 Creation of the Layups 36
4.5.5 FE Model Boundary Conditions 40
4.6 Finite Element Analysis –Vertical Testing 43
4.7 Finite Element Analysis –Torsional Testing 44
4.8 Finite Element Analysis –Lateral Testing 45
5. RESULTS AND DISCUSSIONS 46
5.1 Swingarm Deflection 46
5.2 Strain Analysis 56
5.2.1 Strain Gauge Validation 56
5.2.2 Strain Gauge Transverse Sensitivity 56
5.2.3 Strain Measurements 58
5.3 Finite Element Analysis 69
5.3.1 Finite Element Analysis: Deflections 69
5.3.2 Finite Element Analysis: Strains 72
5.3.3 Effect of Ply Thickness on FE Model Accuracy 94
5.3.4 Finite Element Model – Conclusion 95
6. CONCLUSION AND RECOMMENDATIONS 97
6.1 Conclusions 97
6.2 Recommendations 100
7. REFERENCES 102
Appendix A Strain Gauge Validation 106
Appendix B Load Cell Calibration 110
Appendix C Ply Overlap 113
Appendix D Strain Gauge Positions and NI Data Acquisition System 114

Appendix E Test Rig Modification Calculations and Drawings 124

Appendix F Mesh Dependency 128

LIST OF FIGURES

Figure 1. Example showing the main components of a motorcycle. [4] 2
Figure 2. Example of the rear part of a motorcycle showing the swingarm. [4] 3
Figure 3. A double-sided swingarm [6]. 3
Figure 4. A single-sided swingarm [7]. 4
Figure 5. Sample carbon fibre composite sheets. [11] 5
Figure 6. Example of carbon fibre composite sketch showing different layers orientated in different directions. [17] 6
Figure 7. Single-sided carbon fibre swingarm for a Ducati 1098 motorcycle [19]. 8
Figure 8. Swingarm test rig developed to test the carbon fibre swingarm. 8
Figure 9. Durability test rig for motorcycle handlebars. [23] 10
Figure 10. Durability test rig for suspension system. [25] 11
Figure 11. Example of multi-body simulation using ADAMS® simulation software. 11
Figure 12. Loads acting on the swingarm during cornering assuming thin wheels [8]. 13
Figure 13. Loads acting on the swingarm during cornering assuming thick wheels [8]. 13
Figure 14. Lateral loading of the double-sided aluminium swingarm using spacer and spindle to simulate real loading conditions [8]. 14
Figure 15. Torsional loading of the double-sided swingarm without using a spacer and spindle. 14
Figure 16. Torque-angle curves for three swingarms [5] 16
Figure 17. Test rig showing various components. 23
Figure 18. Test rig showing various components. 23
Figure 19. Connection from swingarm to rocker-arm. 24
Figure 20. Rosette strain gauge. 25
Figure 21. Strain gauge measurement positions. 26
Figure 22. Strain gauge measurement positions. 26
Figure 23. Swingarm test rig to apply vertical load. 27
Figure 24. Rig setup to apply a torsional load on swingarm. 28
Figure 25. Test rig showing the steel arm used in the torsional test. 29
Figure 26. Schematic of deflection of steel arm during torsional loading. 31

Figure 27. Rig setup for applying lateral loads in the global z-direction. 32
Figure 28. Position of dial gauge during lateral loading test measuring the lateral deflection. 33
Figure 29. ANSYS Workbench Project Schematic showing the three parts of the simulation. 34
Figure 30. Swingarm showing the aluminium inserts. 35
Figure 31. Finite element mesh on the swingarm 36
Figure 32. Outer zone of the top arm. 37
Figure 33. Top zone of the top arm. 37
Figure 34. Inside zone of the top arm. 38
Figure 35. Zone underneath the top arm. 38
Figure 36. Zone on outside of bottom arm. 39
Figure 37. Top zone of the bottom arm. 39
Figure 38. Inside zone of the bottom arm. 40
Figure 39. Underside zone of the bottom arm. 40
Figure 40. Positions of loading and constraints on the swingarm. 41
Figure 41. Rocker arm assembly. 42
Figure 42. Rocker arm assembly. 42
Figure 43. Finite element model of swingarm showing the rocker arm. The red dots indicate the positions of the revolute joints. 43
Figure 44. FE model showing constraints applied during vertical loading. 44
Figure 45. FE model subjected to a moment about the longitudinal x-axis and a force in the motorcycle vertical direction. 45
Figure 46. FE model subjected to a load in the motorcycle lateral direction. 45
Figure 47. Vertical deflection of swingarm showing the vertical stiffness coefficient of 500 kN/m. 46
Figure 48. Schematic showing the rear spring and the swingarm as springs in series between the chassis and the wheel. 47
Figure 49. Deflection during loading and unloading of the swingarm 48
Figure 50. Deflection during loading and unloading near the zero load mark. 49
Figure 51. Torsional deflection of the swingarm. 50
Figure 52. Torsional deflection of the swingarm showing the torsional stiffness coefficient of 550 Nm/deg. 50

Figure 53. Torsional deflection of swingarm during loading and unloading during two torsional tests. 52
Figure 54. Torsional deflection during loading and unloading near the zero mark. 53
Figure 55. Lateral deflection of the swingarm. 54
Figure 56. Lateral deflection of the swingarm showing the lateral stiffness coefficient of 445 kN/m. 54
Figure 57. Strain Gauge measurement positions 58
Figure 58. Strain gauge measurement positions. 59
Figure 59. Longitudinal strain measured at positions 3 through 8. 60
Figure 60. Transverse strain measured at positions 1 through 7. 61
Figure 61. Maximum longitudinal and transverse strain at Position 3 during vertical loading. 62
Figure 62. Maximum longitudinal and transverse strain at Positions 4 and 5 during vertical loading. 62
Figure 63. Maximum longitudinal and transverse strain occurring at Positions 6 during vertical loading. 63
Figure 64. Schematic of the vertical and rotational translation of the swingarm during vertical loading. 64
Figure 65. Normalized strain on the top arm of the swingarm due to vertical loading. 64
Figure 66. Longitudinal strain due to the torsional loading. Strain gauge positions are shown on the figure. 66
Figure 67. Strain in the transverse direction due to torsional loading. 66
Figure 68. Maximum longitudinal and transverse strain at Position 3 during torsional loading. 67
Figure 69. Maximum longitudinal and transverse strain at Positions 4 and 5 during torsional loading. 67
Figure 70. Maximum longitudinal and transverse strain at Position 6 during torsional loading. 68
Figure 71. Normalized strain occurring on the top arm of the swingarm due to torsional loading. 69
Figure 72. Vertical deflection at 8000N. 70
Figure 73. Deflection measured during maximum torsional loading of 2000 N and 680 Nm. 71

Figure 74. Lateral deflection under the 135 N load. 72
Figure 75. Strain distribution for Position 2 in the gauge transverse direction at vertical load of 8000 N. 73
Figure 76. Comparison between FEA and experimental results at Position 2 in the gauge transverse direction. 74
Figure 77. Position 2 in the transverse direction with the axes rotated 75
Figure 78. Position 2 in the transverse direction with the axes rotated +2 degrees. ... 75
Figure 79. Close up of the strain distribution for Position 2 in the gauge transverse direction at vertical load of 8000 N 76
Figure 80. Strain distribution for Position 3 in the gauge longitudinal direction. 77
Figure 81. Close up of the strain distribution for Position 3 in the gauge longitudinal direction. 77
Figure 82. Comparison between FEA and experimental results at Position 3 in the gauge longitudinal direction. 78
Figure 83. Strain at Position 3 in the longitudinal direction with the axes rotated +2 degrees. 79
Figure 84. Strain distribution for Position 3 in the gauge transverse direction. 79
Figure 85. Close up of the strain distribution for Position 3 in the gauge transverse direction (vertical direction in the figure). 80
Figure 86. Comparison between FEA and experimental results at Position 3 in the gauge transverse direction. 81
Figure 87. Position 3 in the transverse direction with axes rotated -2 degrees. 81
Figure 88. Position 3 in the transverse direction with axes rotated +2 degrees. 82
Figure 89. Strain distribution for Position 4 in the gauge longitudinal direction at 8000N. 83
Figure 90. Comparison between FEA and experimental results at Position 4 in the gauge longitudinal direction. 83
Figure 91. Strain distribution for Position 4 in the gauge transverse direction at 8000N. 84
Figure 92. Comparison between FEA and experimental results at Position 4 in the gauge transverse direction. 85
Figure 93. Updated longitudinal strain at Position 4 by adding 3 plies. 86
Figure 94. Updated transverse strain at Position 4 by adding 3 plies. 86
Figure 95. Strain distribution for Position 5 in the gauge longitudinal direction. 87

Figure 96. Comparison between FEA and experimental results at Position 5 in the gauge longitudinal direction. 88
Figure 97. Strain distribution for Position 5 in the gauge transverse direction. 88
Figure 98. Comparison between FEA and experimental results at Position 5 in the gauge transverse direction. 89
Figure 99. Strain distribution for Position 6 in the gauge longitudinal direction. 90
Figure 100. Comparison between FEA and experimental results at Position 6 in the gauge longitudinal direction. 91
Figure 101. Longitudinal strain at Position 6 after adding three ±45° plies. 92
Figure 102. Strain distribution near Position 6 in the gauge transverse direction. 92
Figure 103. Comparison between FEA and experimental results at Position 6 in the gauge transverse direction. 93
Figure 104. Strain distribution for Position 6 in the gauge transverse direction with the addition of 3 ±45° plies. 94
Figure 105. Rig setup for testing the carbon fibre plate. 106
Figure 106. Axial strain gauge applied near the fixed end of the plate. 107
Figure 107. Constraints applied to the carbon fibre plate created in Ansys Composite. 108
Figure 108. Graphical FEA results for the cantilever plate. 108
Figure 109. Longitudinal strain of 499 $\mu\varepsilon$ obtained from Ansys Composite. 109
Figure 110. Top part of the load cell calibration rig showing the load cell attached to the portable crane via a steel chain. 110
Figure 111. Basket carrying weights applying a load to the load cell. 111
Figure 112. Calibration curve for the 50kN load cell. 112
Figure 113. Schematic of plies overlapping each other. 113
Figure 114. Adjacent plies without ply overlap. 113
Figure 115. Strain Gauge 1 114
Figure 116. Strain Gauge 1. 114
Figure 117. Strain Gauge 2. 115
Figure 118. Strain Gauge 2. 115
Figure 119. Strain Gauge 3. 116
Figure 120. Strain Gauge 3. 116
Figure 121. Strain Gauge 4. 117

Figure 122. Strain Gauge 4. 118
Figure 123. Strain Gauge 5. 119
Figure 124. Strain Gauge 5. 119
Figure 125. Strain Gauge 6. 120
Figure 126. Strain Gauge 6. 120
Figure 127. Strain Gauges 7 & 8. 121
Figure 128. Strain Gauge 7. 121
Figure 129. Strain Gauge 8. 122
Figure 130. NI data acquisition system connected to the strain gauges on the swingarm. 123
Figure 131. Isometric view of the top part of the steel shaft. 125
Figure 132. Top part of the steel shaft. 126
Figure 133. Bottom part of steel shaft. 127
Figure 134. Position 4 with element size of 5 mm. 128
Figure 135. Position 4 with element size of 3 mm. 128
Figure 136. Position 4 with element size of 1 mm. 129

LIST OF TABLES

Table 1. Equipment and instrumentation used in the test rig. 22
Table 2. Forces and moments applied during torsional test. 30
Table 3. Loads applied during lateral test. 33
Table 4. Material properties of the carbon fibre plies used in the FE model. 35
Table 5. Comparison of torsional stiffness values obtained from the literature. 51
Table 6. Comparison lateral stiffness values. 55
Table 7. Measured strain in the longitudinal and transverse directions at maximum load of 8000 N at Positions 3-6. 57
Table 8. Strain correction at Positions 3-6 using K_t = +5% (0.05). 57
Table 9. Strain correction at Positions 3-6 using K_t = -5% (-0.05). 57
Table 10. Comparison between experimental and FEA vertical deflection at the wheel mount. 70
Table 11. Comparison between experimental and FEA rotation at the wheel mount. 71
Table 12. Comparison between experimental and FEA lateral deflections at the wheel mount. 72
Table 13. Effect of change in thickness of plies at Position 4. 94
Table 14. Comparison of experimental and FE strain results. 99
Table 15. Load applied to cantilever plate and the resultant axial strain from experimental setup. 107
Table 16. Comparison between the measured strain and the strain calculated by ANSYS. 109
Table 17. Calibration values for the 50kN load cell. 111
Table 18. Mesh sensitivity. 129

LIST OF SYMBOLS

d	Length of moment arm [m]
F	Applied force [N]
I	Second moment of area [m^4]
K_t	Transverse sensitivity factor
k_t	Torsional stiffness coefficient [Nm/deg] or [Nm/rad]
k_{sp}	Stiffness coefficient of spring [kN/m]
k_{sw}	Vertical stiffness of swingarm [kN/m]
M	Moment [Nm]
r	Radius [m]
s	Deflection [m]
s_1	Deflection at top of arm [m]
s_2	Deflection at wheel mount [m]
y	Distance from the neutral axis [m]
ε_x	Actual strain in the gauge 0° direction [με]
ε_y	Actual strain in the gauge 90° direction [με]
ε_{mx}	Measured strain in the gauge 0° direction [με]
ε_{my}	Measured strain in the gauge 90° direction [με]
θ	Angle of rotation [rad]
υ_0	Poisson's ratio for steel
σ	Stress [Pa]

LIST OF ACRONYMS

APDL	ANSYS Parametric Design Language
CAE	Computer Aided Engineering
CFRP	Carbon Fibre Reinforced Plastic
CLT	Classical Laminate Theory
FE	Finite Element
FEA	Finite Element Analysis
FEM	Finite Element Model
FRP	Fibre Reinforced Plastic
GFRP	Glass Fibre Reinforced Plastic
MBS	Multi-Body Simulation
RVE	Representative Volume Element
SPATE	Stress Pattern Analysis by Thermal Emission

1. INTRODUCTION

1.1 Background

Carbon fibre has not been extensively used in the development of motorcycle swingarms. This study investigates the development of a carbon fibre swingarm with an emphasis on the structural integrity and on developing a finite element model (FEM). The motorcycle swingarm plays an important role in the rear part of the motorcycle. The literature shows that strength, stiffness and weight are important factors in motorcycle swingarm design. The swingarm should be strong enough to handle typical loads experienced in the field and stiff enough to increase the response and stability of the motorcycle. The weight of the swingarm should also be reduced to improve motorcycle performance and increase the road holding of the rear wheel. Most motorcycles use materials such as steel, aluminium and magnesium in their swingarm design. Carbon fibre however, offers benefits such as low weight while maintaining high stiffness and strength characteristics [1] and being able to tailor the material characteristics for specific applications [2]. The current research presents the initial phase in the design and manufacture of a carbon fibre swingarm for a Ducati 1098 motorcycle using preliminary laminates. Essentially, a swingarm was manufactured using an initial design of the carbon fibre laminates and this study proceeded to investigate the swingarm from a structural integrity point of view. The literature further shows that the development of a finite element (FE) model is important in the continued improvement of the swingarm design. To these two ends, a test rig was developed for measuring deflection (to determine stiffness) and strain (to determine strength) of swingarms and the results were used in developing an FE model. The results provided insight into further possible areas of improvement in the design of a carbon fibre swingarm. As indicated above, this research report does not present information regarding the design of the carbon fibre laminates but presents the testing of the swingarm (to determine the stiffness and strain characteristics) and the development of a FE model. Once the stiffness characteristics were obtained, it was then possible to see which areas of design (including the laminate) might need improvement.

1.2 The Motorcycle Swingarm

The motorcycle structure is made up of three main components, namely the front fork, the main frame and the swingarm [3] (Figure 1).

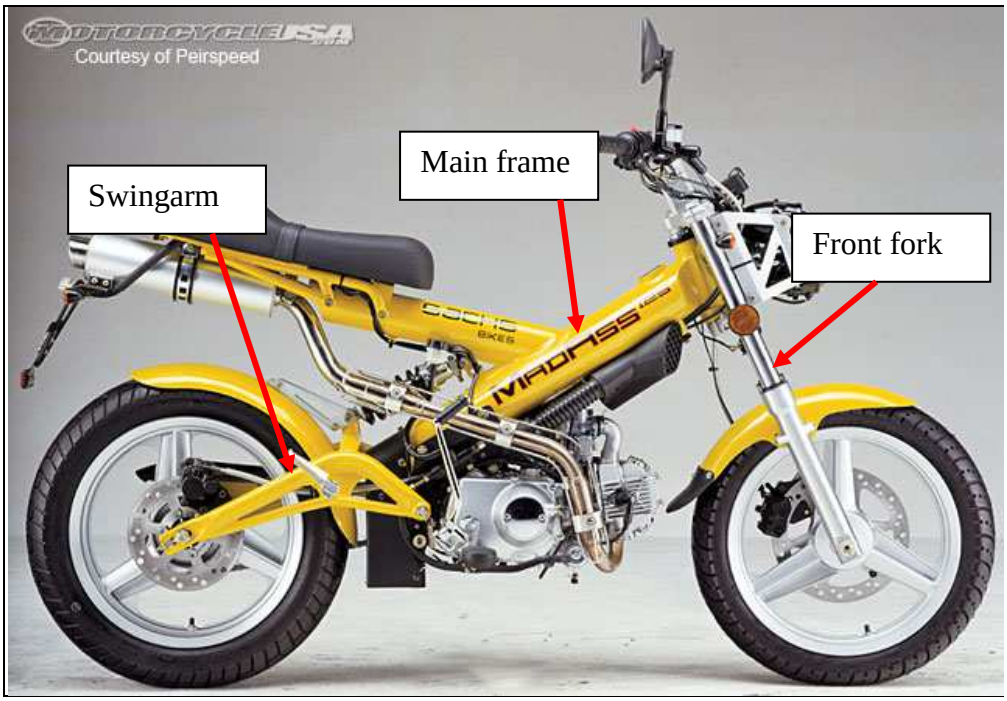


Figure 1. Example showing the main components of a motorcycle. [4]

The swingarm is the main component of the rear suspension of a motorcycle and functions to connect the rear wheel to the chassis and to regulate the rear wheel-road interaction via the spring and shock absorber [5]. Figure 2 presents an example of a rear part of a motorcycle and its swingarm.

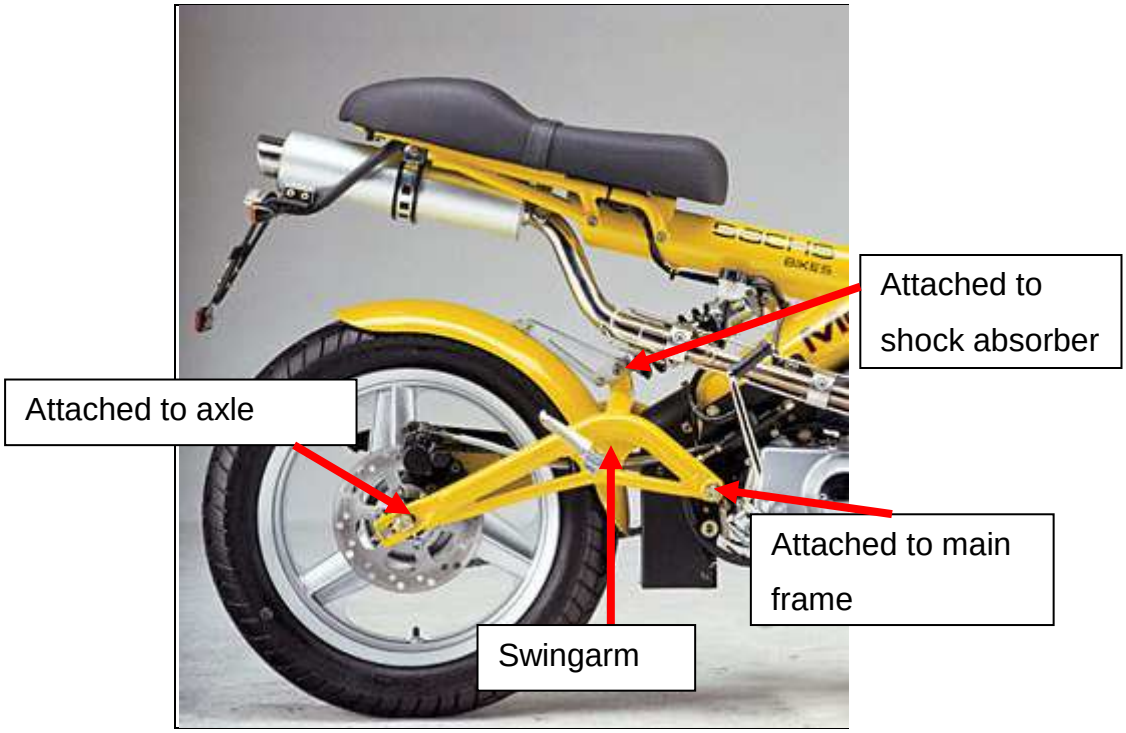


Figure 2. Example of the rear part of a motorcycle showing the swingarm. [4]

There are two basic swingarm designs, namely the double-sided, shown in Figure 3 and the single-sided, shown in Figure 4.

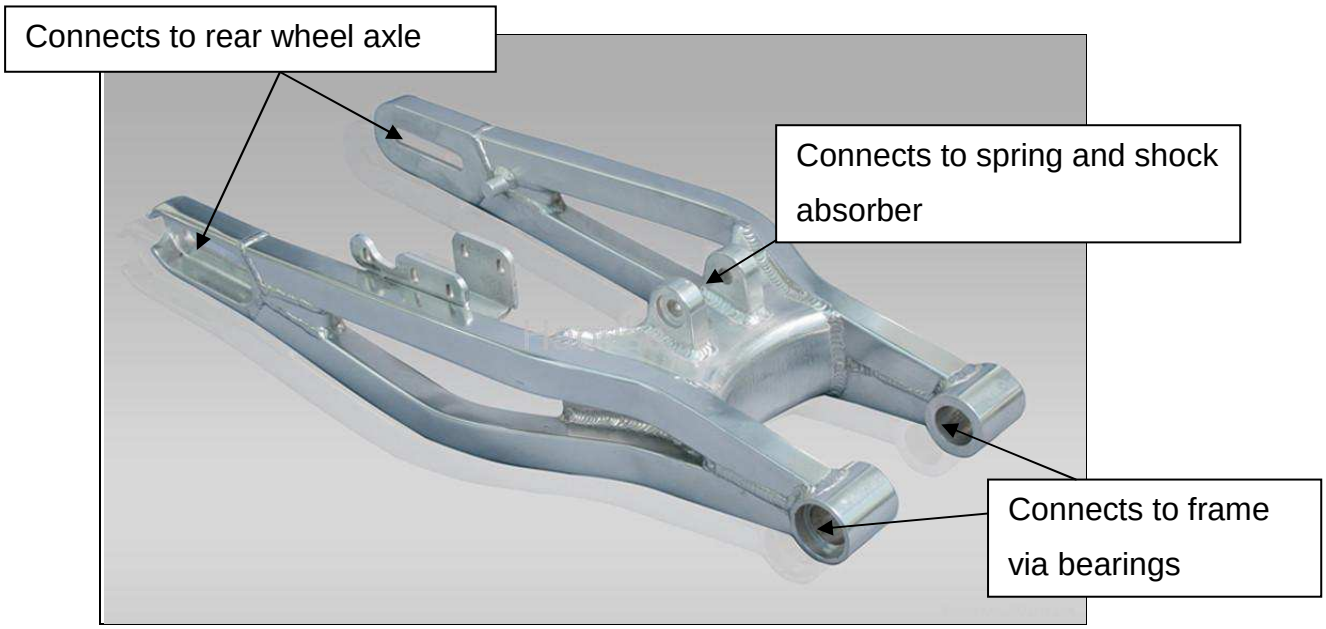


Figure 3. A double-sided swingarm [6].

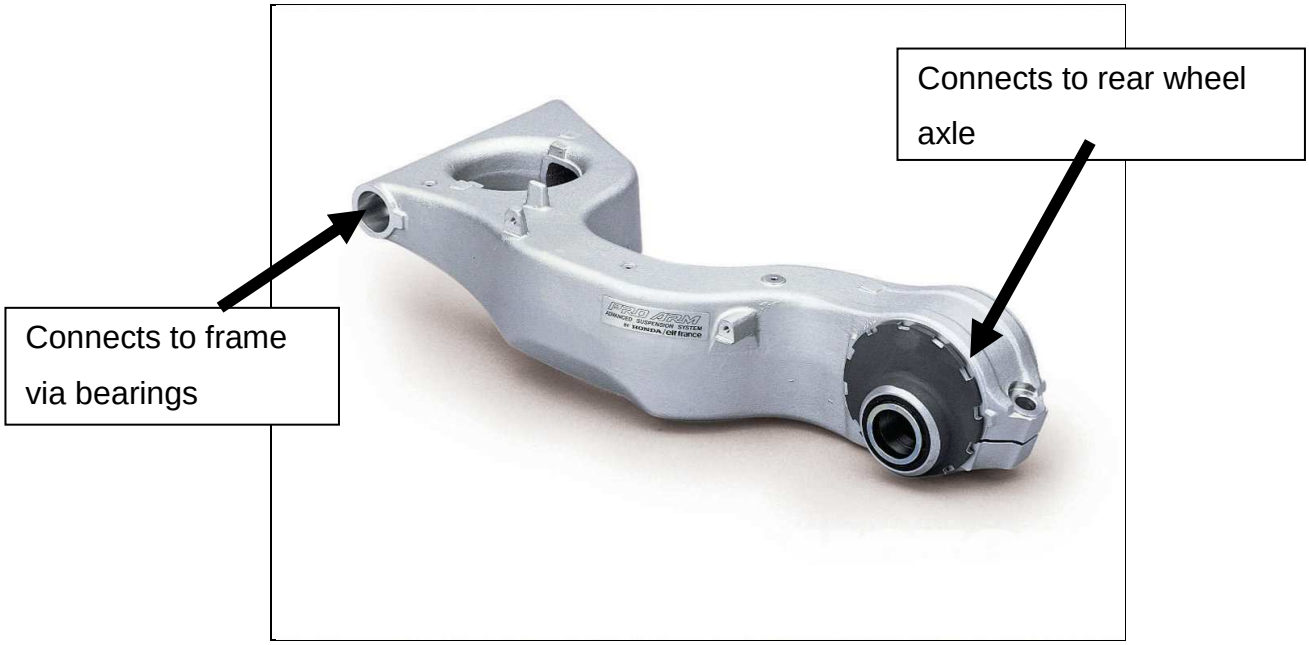


Figure 4. A single-sided swingarm [7].

A benefit of the single-sided swingarm is that it allows for easier removal of the rear wheel during racing [2]. A twisting moment acts in the single-sided swingarm which does not exist in conventional double-sided designs [2], and to maintain torsional rigidity similar to that of a double-sided swingarm, extra material may need to be added which increases the unsprung mass. This may be a disadvantage because in general a higher unsprung mass decreases the roadholding of the rear wheel. This presents the need to reduce the weight of the swingarm.

The swingarm lateral and torsional stiffness is shown to be important in swingarm design [3] [8] because they affect the side to side movement (weave mode) of the motorcycle. In general, it is desirable to maximise the swingarm stiffness to reduce the weave mode instability [9]. The vertical stiffness also plays an important role in the motorcycle setup. The swingarm and the rear suspension spring form two springs in series between the main chassis and the wheel. If not stiff enough vertically, the swingarm can change the motorcycle setup and produce unpredictable behaviour.

Although each motorcycle will require different values for swingarm rigidity, Cossalter [10] states that typical values for lateral swingarm stiffness are 800 kN/m – 1600 kN/m and 1 kNm/deg – 2 kNm/deg for torsional stiffness. No literature was found documenting typical values for vertical stiffness.

It should be noted that no standards were found that govern swingarm design. The literature essentially shows that the swingarm should be strong enough to handle the various loads, light enough to reduce the unsprung mass, and be designed to limit the dynamic instability of the motorcycle. More detail will be presented in Section 2.2 on swingarm development.

1.3 Composite Materials

The swingarm under investigation is made from carbon fibre composite (Figure 5) and this section presents a brief overview of composite materials and classical laminate theory (CLT) which governs composite design.



Figure 5. Sample carbon fibre composite sheets. [11]

A composite material consists of two or more distinct material types acting in combination. This definition can be applied to a vast range of materials but is mainly used to describe fibre reinforced plastics (FRPs) such as glass, boron and carbon fibre where carbon fibre reinforced plastic (CFRP) is increasingly being used [12] [2].

A variety of materials which are light and have high strength and rigidity have been used for swingarms, including aluminium [13] and magnesium alloy [14] with magnesium being the lightest of the various *metals* currently being used. Carbon fibre has a similar weight density to magnesium, yet due to the ease of forming these materials into complex shapes, carbon fibre can be engineered to have a much higher stiffness to weight ratio than magnesium [15]. The use of composites allows for a

range of benefits such as being able to modify the material characteristics and structural stiffness [2], and having high strength and stiffness to weight ratios [1]. In the automotive industry, composites have been used in chassis, car doors, drive shafts and leaf springs.

Although the benefits of carbon fibre over metals are well documented, developments in the application of carbon fibre reinforced plastic has not been as fast as expected [12] and in motorcycle design there has not been widespread use [13]. Reasons include high carbon fibre price, complex motorcycle shapes and general industrial challenges which indicate the supporting carbon fibre industry is not yet mature enough for mass production [13] [16].

A difficulty arises when designing a component using composite material since not only must a design of the component be carried out, but due to the anisotropic nature of composite material, the material itself must also be designed. Anisotropic materials have properties that change according to direction due to their non-homogeneous nature and differences in properties between fibres and the matrix [12].

Classical laminate theory (CLT) is used to predict the properties and behaviour of a laminate which consists of laminae (plies) orientated in different directions (Figure 6).

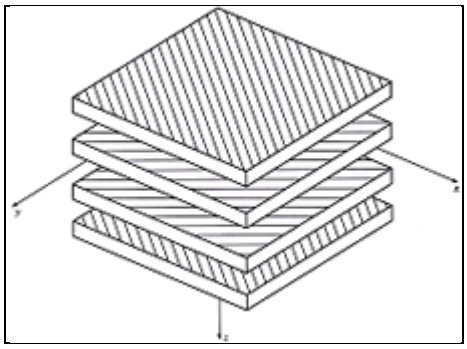


Figure 6. Example of carbon fibre composite sketch showing different layers orientated in different directions. [17]

When applying this method, the following assumptions are made [12]:

- Each lamina is macroscopically homogeneous and linearly elastic
- The plies are perfectly bonded to each other when forming the laminate
- The laminate has infinite through thickness shear stiffness. The through thickness direction is normal to the lamina surface.

- The plane sections remain plane when the laminate is bent or extended.

CLT provides a method of calculating strains and curvatures in the laminate if the forces and moments acting on the laminate are known. Conversely, if the strains and curvature are known, then the forces and moments can be calculated.

FEA is the most popular numerical technique for analysing composite structures according to Wood [18] and the finite element package ANSYS (ANSYS® Academic Research, Release 14.5, Composite PrepPost, ANSYS, Inc.) used in this study, bases its composite software on CLT. Difficulties arise when trying to obtain material properties and failure strengths for composite materials.

1.4 Project Overview

This study begins by reviewing literature to establish what research has been carried out in the following areas:

- The development of test rigs (both experimental and virtual) for the testing of automotive components.
- The design and testing of motorcycle swingarms.
- The application of finite element analysis (FEA) to composite materials.

Based on the literature review, a few points will be seen. The first is that a need exists to develop automotive components from composite materials due to their lightweight and high strength and stiffness properties. This was carried out using an initial laminate design and this study investigates this design. A single-sided carbon fibre swingarm shown in Figure 7 was developed for a Ducati 1098 motorcycle.



Figure 7. Single-sided carbon fibre swingarm for a Ducati 1098 motorcycle [19].

The second is the importance of determining the stiffness characteristics of swingarms because of their effect on the stability of the motorcycle. For fatigue and static testing of the swingarm, a durability test rig was developed (Figure 8).

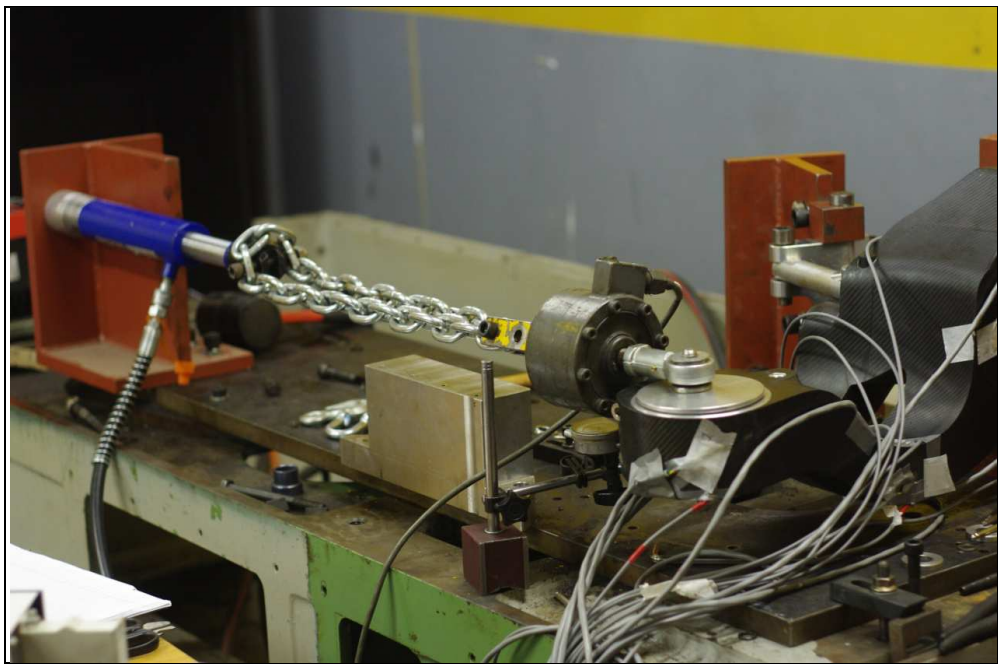


Figure 8. Swingarm test rig developed to test the carbon fibre swingarm.

The vertical, lateral and torsional stiffness characteristics of the swingarm as well as strains at various positions were determined from the experimental tests.

Lastly, there is the need to develop a finite element model of the swingarm which will facilitate cost-effective design optimisations. This research report presents a study of the stiffness characteristics and strain distribution of the swingarm as well as the development of a finite element model of a carbon fibre swingarm.

2. LITERATURE REVIEW

2.1 Automotive Test Rig Development

A considerable amount of research has been carried out in the development of test rigs for automotive component design. Product development is no longer confined to experimental testing but now also includes testing in the virtual (computer simulated) environment. Advantages of virtual testing include being able to evaluate the design early in the development process before the prototype is available and also allows for data to be obtained to help with setting up experimental testing [20]. Virtual models are best at delivering an understanding of system behaviour, interactions and sensitivity, whilst physical tests are good at identifying absolute levels of performance and the response of complex systems [21].

Durability tests have been used extensively in automotive component design. Servo-hydraulic rigs (used for durability testing) are one of the main experimental methods used in automotive design [22]. Durability test rigs have been built to test the fatigue life of motorcycle handlebars (Figure 9) [23], vehicle suspensions (Figure 10) [20] and motorcycle frames [24] to name a few. During testing, results are generally obtained by measuring strain on the component and then calculating the corresponding stresses.

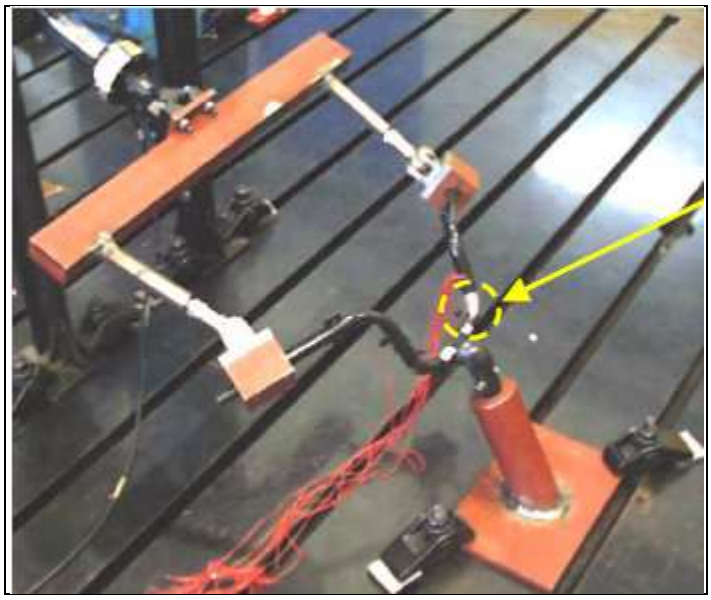


Figure 9. Durability test rig for motorcycle handlebars. [23]



Figure 10. Durability test rig for suspension system. [25]

The literature indicates that there is an increasing need to develop virtual tests that can simulate the experiments. Multi-body simulation (MBS) has been used to simulate suspension test rigs and thereby calculate accelerations, bending moments and forces in motorcycle frames (Figure 11) [20]. Forces calculated in MBS may then be used in the FEA of the component to calculate stresses and strains. In certain cases, FEA is carried out to first obtain an indication of the stress and strain distribution which then allows for more strategic strain measurements to be carried out during experimental testing [22] [23].

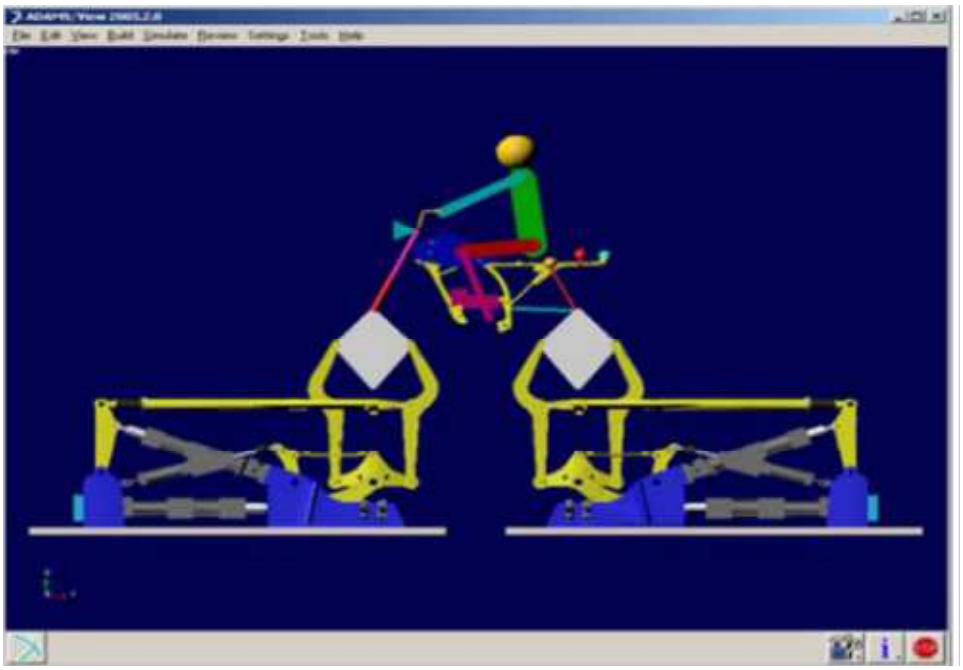


Figure 11. Example of multi-body simulation using ADAMS® simulation software.

From this discussion on test rigs, it is clear that for the successful design and testing of automotive components, there is the need to combine virtual (FEA) and experimental methods.

2.2 Swingarm Development

A survey of the literature shows that there has been limited research into the design and testing of motorcycle swingarms and even less into the development of composite swingarms. Armentani, Fusco and Pirozzi [8] determined lateral and torsional stiffness values of three double-sided aluminium swingarms by carrying out experimental tests and FEA. They claimed that the main difficulty in designing the swingarm is to obtain the right balance between the flexional and torsional stiffness, although no indication is given of what the right balance is. They initially defined the loads acting on the rear wheel during cornering. When viewed from the rear of the motorcycle (Figure 12) along the longitudinal axis, the moment caused by the centrifugal force (that tends to restore the motorcycle to the vertical position) is balanced by the moment caused by the weight of the motorcycle and rider (that tends to cause the motorcycle to fall over). Assuming that the wheels are thin, the resultant of these two forces is balanced by a resultant reaction and friction force at the wheel-road contact point that acts along the plane of the wheel.

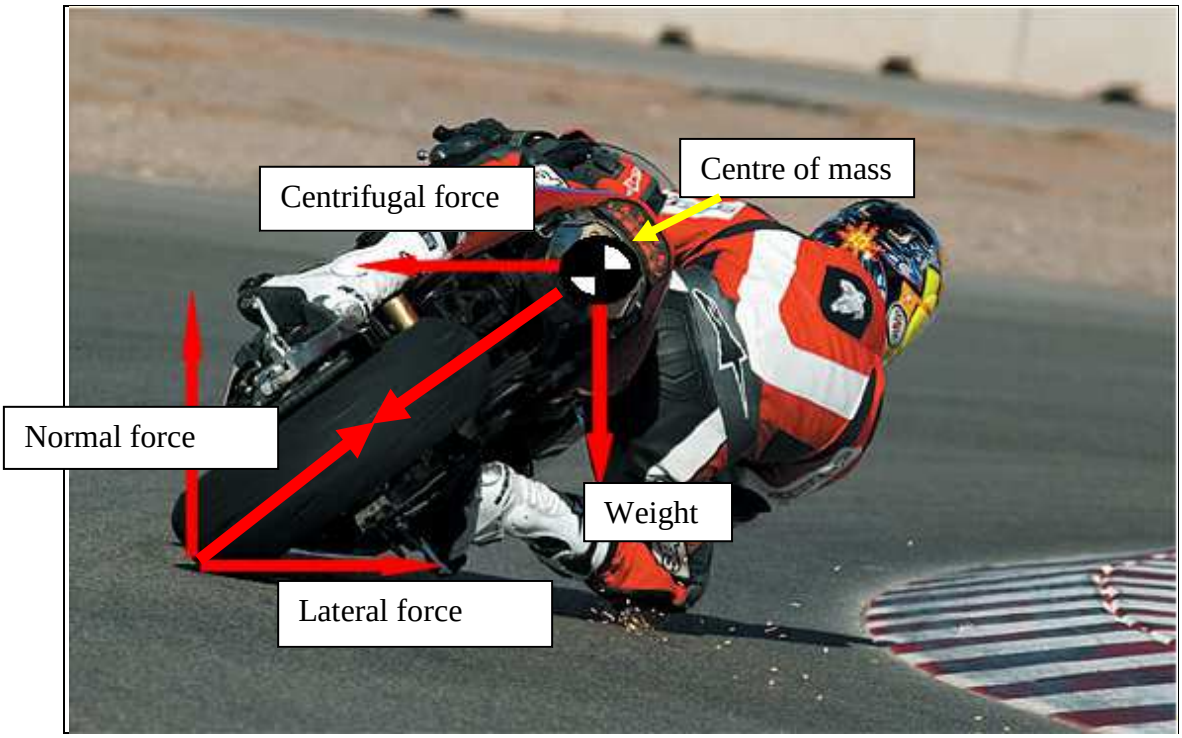


Figure 12. Loads acting on the swingarm during cornering assuming thin wheels [8].

In reality however, due to the thickness of the tyres, the resultant force does not act in the plane of the wheel but along the line connecting the centre of mass and the tyre contact point (Figure 13). This actual resultant force (R_s) has components acting parallel and perpendicular to the wheel plane. The perpendicular component will generate both a lateral force and a moment about the longitudinal axis.

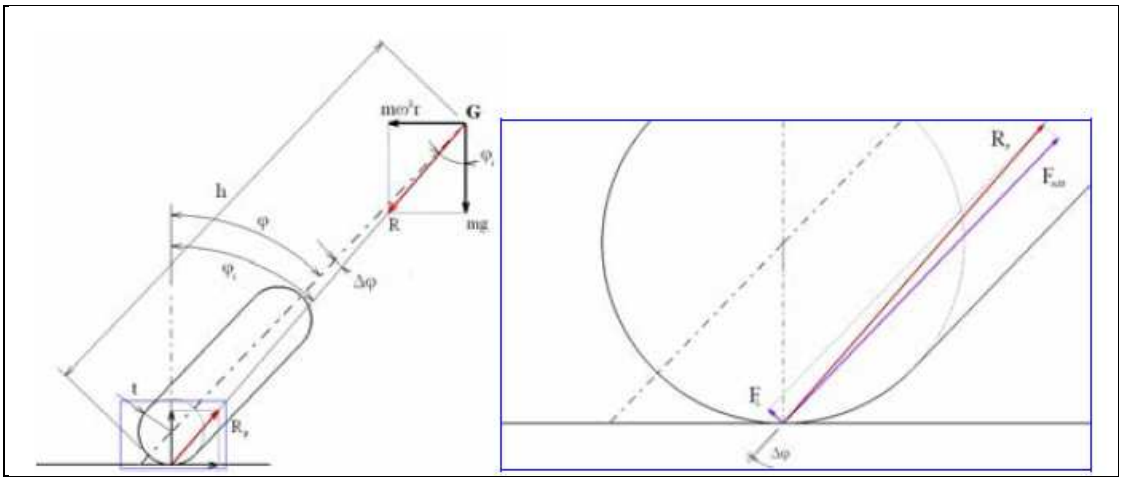


Figure 13. Loads acting on the swingarm during cornering assuming thick wheels [8].

For a motorcycle with a mass of 230 kg, Armentani et al. calculated the lateral force and moment to be 125 N and 31 Nm respectively which they applied during experimental testing and FEA. The loads were applied to three different swingarms used on a Kawasaki ZX10R, Suzuki GSX R1000 and Honda CBR1000R. To simulate real loading conditions, the lateral deflection was measured while a spacer and spindle were mounted to the wheel connection points as shown in Figure 14. Lateral stiffness values of 603 kN/m, 804 kN/m and 965 kN/m were calculated from the force and deflection measurement.

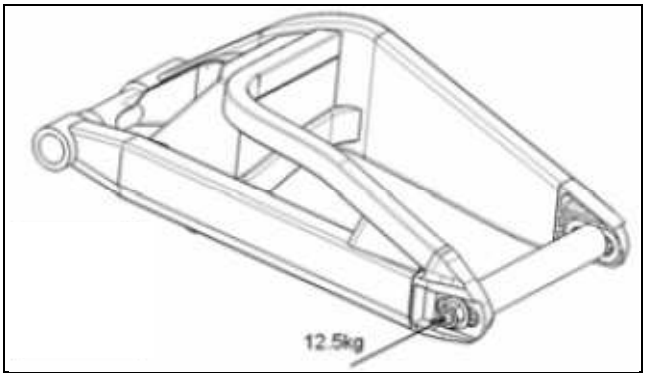


Figure 14. Lateral loading of the double-sided aluminium swingarm using spacer and spindle to simulate real loading conditions [8].

The torsional loading however, was measured without using the spacer and spindle. The moment of 31 Nm was applied via a force of 249.1 N (25.4 kg) on one of the swingarm legs as shown in Figure 15.

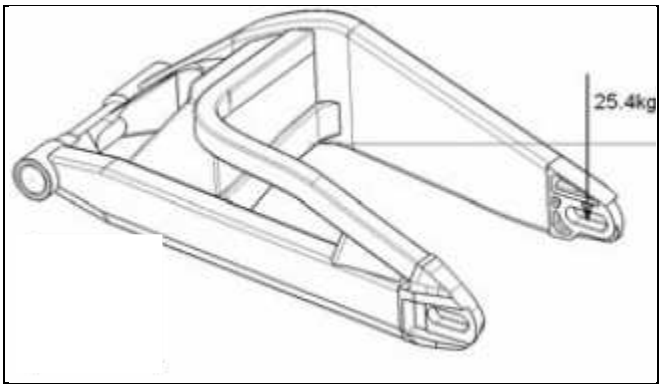


Figure 15. Torsional loading of the double-sided swingarm without using a spacer and spindle.

It is unclear why Armentani et al. did not make use of the spacer and spindle when applying the torsional loading. By applying the load only on one arm without the spacer in between, it is most likely that higher displacements were measured than if

the spacer and spindle were inserted to simulate real life conditions. By applying the load without spacer and spindle, torsional stiffness values of 5896 Nm/rad (102.9 Nm/deg), 8068 Nm/rad (140.8 Nm/deg) and 8068 Nm/rad (140.8 Nm/deg) were calculated for the Kawasaki ZX10R, Suzuki GSX R1000 and Honda CBR1000R swingarms respectively. The torsional stiffness values are therefore assumed to be less stiff than what would be measured while simulating real life conditions. It will be seen later that these torsional stiffness values are indeed much lower than other values measured in the literature.

Dragoni and Foresti [26] aimed to improve a magnesium swingarm design by using carbon-epoxy composite material. They claimed that the structural behaviour of magnesium is satisfactory but sought to reduce the mass of the arm while maintaining a similar stiffness. Before investigating the composite design, an FE model of the original magnesium model was verified by simulating the torsional response and comparing it with experimental values. They state that the torsional response is the single most important feature of the swingarm from a structural point of view. The finite element package ALGOR was used to build the FE model of the composite design because it supports anisotropic plate elements suited for laminate structures. Three models were built based on three designs. A pure-torsional load was applied to each of them, and the laminate thickness was adjusted to obtain similar stiffness values to the magnesium design. No detail is provided as to the magnitudes of the loads. Normalised results show that the final composite design had an increased torsional stiffness of 10%, a reduced mass of 30% and a reduced mass moment of inertia of 40%.

Risitano, Scappaticci, Grimaldi and Mariani [5] aimed to link objective data such as swingarm stiffness and natural frequencies with subjective information such as handling and comfort perceived by riders. They claimed that to characterize the swingarm, it is important to look at the torsional stiffness. The less stiff the swingarm is, the heavier the motorcycle feels to the driver and the more difficult manoeuvring becomes. The stiffer the swingarm, the quicker the response is during cornering. Risitano et al. tested the torsional rigidity and symmetrical behaviour of three double-sided aluminium swingarms. A rig was built that could apply a purely torsional load to the swingarm and measure the twist angle about the longitudinal axis. This was

done in both clockwise and counterclockwise directions. No explanation was given for how the magnitudes of the torsional loads (between 0 and 400 Nm) were derived, and it is assumed that the loading was applied simply to obtain the stiffness characterization. The loads were applied by hydraulic jacks and deflections were measured via potentiometers. From the tests, torsional stiffness values of 670 Nm/deg, 890 Nm/deg and 1330 Nm/deg were found for the three swingarms (Figure 16).

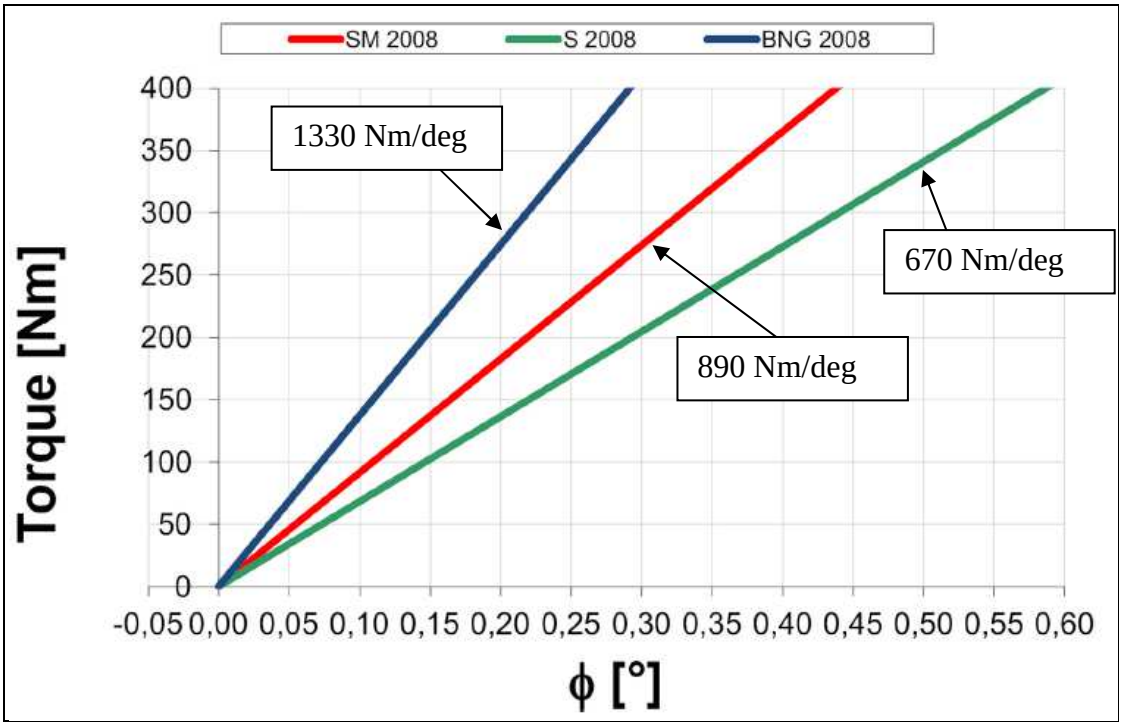


Figure 16. Torque-angle curves for three swingarms [5]

An FE model was built in ANSYS Workbench and similar tests were simulated. The average difference between the FE and experimental results was under 4%.

Cossalter, Lot and Massaro [27] studied the effect the swingarm has on the weave mode stability of a 150 cc scooter. The weave mode describes the side to side oscillation of the motorcycle which is due to yaw and roll effects of the motorcycle. Cossalter et al. showed that from 0 m/s to 18 m/s (65 km/h), the degree of torsional and lateral rigidity has negligible effect on the weave mode stability. However, as the torsional stiffness increases, the weave mode stability increases at speeds higher than 18 m/s. The weave mode stability also increases as the lateral stiffness increases, but only up until 36 m/s (130 km/h). At speeds above 130 km/h an increase in lateral stiffness shows a decrease in weave mode stability. Therefore at speeds greater than

130 km/h, the torsional and lateral stiffness affects the weave mode stability in a contradictory manner.

Lake, Thomas and Williams [28] summarized work carried out by various researchers on the effect that swingarm stiffness has on the motorcycle weave mode and found conclusions that matched Cossalter et al. [27] above. Lake et al. state that it is obvious that the increase in torsional stiffness increases the weave mode stability but asked *what are acceptable values of swingarm torsional stiffness*? They showed that Sharp [29] claimed that a torsional stiffness value of 209 Nm/deg would approach an absolutely rigid swingarm. However recent designs have significantly higher swingarm stiffness values. For example, Cossalter [10] stated that modern swingarms have stiffness values of between 1000 Nm/deg and 2000 Nm/deg as discussed earlier. Risitano et al. [5], also discussed above, determined values of 670 Nm/deg and higher. The values calculated by Armentani et al [8] (discussed earlier) of between 102.9 Nm/deg and 140.8 Nm/deg, appear to be unusually low for swingarms and even lower than what was suggested by Sharp [29] and the possible reasons for their low stiffness values were discussed earlier. Lake et al. [28] conclude their study on torsional stiffness by saying that the reported torsional stiffness on contemporary swingarm designs is not consistent.

Iwasaki, Mizuta, Hasegawa and Yoshitake [14] developed a magnesium swingarm due to the growing concern over improving fuel efficiency in motorcycles. Four finite element models of the swingarm were built using MSc–Nastran. The first was a conventional aluminium design and the other three designs were of magnesium. The torsional rigidity of the designs was analysed using finite element models and a test rig. The redesigned swingarms were 10% lighter and 60% more torsionally rigid.

Dragoni (discussed above) [26], Airoldi & Bertolie [2] and O'Dea [13] carried out designs of swingarms using composite materials. The latter two investigated methods of designing the swingarm by optimising the stacking sequence of the laminates in the composite. Airoldi et al. carried out a redesign of a single-sided swingarm using carbon fibre composite. The goal was to compare a composite swingarm design with an existing aluminium design. They aimed to minimize the torsional, lateral and vertical deflections as well as the mass by investigating the stacking sequences of the

plies. Genetic algorithms were used to identify a lamination sequence that gave the desired stiffness properties. FEA was only carried out on the original aluminium design and not on the composite arm which was designed using an optimisation algorithm (implemented in Matlab). O'Dea redesigned and manufactured a double-sided swingarm from a Honda CRF450 using carbon fibre epoxy composite moulded in metal inserts. The method of design was carried out using the Composite Modeler ply modelling and fibre simulation software developed by Simulayt Ltd [30]. Composite Modeler allows the user to specify the design of the plies and then simulate the manufacturing process to highlight any possible manufacturing problems.

2.3 Leyni Durability Test

Thus far the literature has focussed on determining lateral and torsional stiffness of swingarms. The only literature found that looked at vertical loading of swingarms was the Leyni Durability Test used by Gaiani [31] that carried out fatigue tests on an aluminium single-sided swingarm in the vertical direction. The Leyni Test rig consists of a drum with a 300 mm high step on it and turns with a speed of 20 km/h and rotational frequency of 3.7 Hz. The rear wheel of a motorcycle is mounted on the drum and as the drum rotates it applies an impulse load to the wheel every time the step passes. During the cyclic loading, the initial static load due to the driver and passenger was 1960 N and a maximum applied loading of 5900 N occurred when the step impacted the wheel. Therefore although the current research is based on static loading, the magnitude of the vertical loads applied in the Leyni Test were taken into account.

2.4 Experimental Strain Measurements on Composites

Due to the swingarm being made from carbon fibre it was necessary to study literature discussing measuring strain on orthotropic[1] materials. Tuttle and Brinson [32] studied strain gauge transverse-sensitivity effects and errors due to gauge misalignment when measuring strain on orthotropic materials. The transverse-sensitivity refers to a strain gauge responding to a strain field that is perpendicular to the gauge's major axis. This response is undesirable because the reading obtained is not the actual strain in that direction but a combination of axial and transverse strain. The effect of transverse

[1] A material whose properties differ in the x-,y- and z-directions.

sensitivity should always be considered when strain is being measured in a biaxial stress field and if the error due to this phenomenon is significant, then correction should be made. A full discussion on correcting for transverse sensitivity can be seen in [33] but the basic equations for correcting transverse sensitivity are presented in Equations 2-1 and 2-2 which can be used when a rosette strain gauge is applied to measure strain.

$$\varepsilon_x = (1 - \upsilon_0 K_t)(\varepsilon_{mx} - K_t \varepsilon_{my}) \quad (2\text{-}1)$$

$$\varepsilon_y = (1 - \upsilon_0 K_t)(\varepsilon_{my} - K_t \varepsilon_{mx}) \quad (2\text{-}2)$$

Where ε_{mx}, ε_{my} = Strains measured along the x and y axes,

K_t = Transverse sensitivity factor calculated by dividing the transverse gauge factor by the axial gauge factor, normally between -0.05 and +0.05,

ε_x, ε_y = Corrected or true strains in the x- and y-directions, and

υ = Poisson's ratio of the material on which the manufacturer's gauge factor was measured, normally 0.285.

Concerning gauge misalignment, due to the orthotropic nature of carbon fibre composites, the principal strain direction does not always coincide with the principal stress directions. Therefore if a gauge is intended to measure strain along a specific direction and there is slight misalignment, errors may occur which are larger than that for an isotropic[2] material. The error is dependent on the following:

- misalignment of the gauge with the intended direction of measurement, and
- angle between the fibre direction and the measurement direction.

Tuttle and Brinson [32] looked at the effect of gauge misalignment at plus and minus 2 and 4 degrees with reference to the intended axis of measurement on a unidirectional graphite epoxy composite. It was found that the largest errors occurred when the angle between the gauge direction and the fibre direction was 8°. Errors of 15% and 30% occurred for the 2° and 4° misalignment. Therefore when comparing

[2] A material whose properties are the same in all directions.

the FE results with the experimental values in Section 5.3.2, the effect of gauge alignment is discussed.

2.5 Finite Element Analysis on Composites

As presented in Section 2.2, only a few papers were found that directly investigated composite swingarms. It was necessary therefore to briefly look at literature focussing on the use of FEA for general composite applications.

Ali [34] studied the performance of FE techniques by analyzing structures where the theoretical solutions were available. These structures included an axially loaded plate and a simply supported plate and beam. A fundamental difficulty with FE systems is their inability to accurately define the orientation of composite materials which are anisotropic. Stresses are discontinuous at the interface of two plies. The stress-strain relationship for a laminate can be synthesized from the properties of all the plies making up the laminate. The entire stack of plies can therefore be modelled with a single shell finite element because the material properties of the laminate are completely reflected in the elastic moduli matrices for the element. These matrices can be calculated if the thickness, material properties and relative orientation is known for each ply in the laminate.

Yinhuan and Zhigao [35] analysed the mechanical characteristics of a glass fibre leaf spring using ANSYS software. Glass fibre reinforced plastics (GFRP) are orthotropic materials and the SOLID 46 laminated element was used in the finite element model. This element allows for up to 250 layers where the material properties, thicknesses and orientations can be specified for each layer.

Mian, Wang and Dar Zhang [36] investigated the proper fibre orientation and laminate thickness for three composites, namely S-glass/epoxy, Kevlar/epoxy and Carbon/epoxy used in pressure vessel design. The ANSYS Parametric Design Language (APDL) and Design Optimization module was used in the analysis and the numerical results were verified using Matlab code based on classical lamination theory and Tsai-Wu failure criteria. Tsai-Wu failure criteria were used to predict first ply failure of a composite laminate.

3. OBJECTIVES

This study took the initial step in the design of a carbon fibre swingarm. The following objectives were set:

1. Determine the vertical, lateral and torsional stiffness and strain characteristics of a prototype swingarm through experimental testing.
2. Develop an FE model of prototype carbon fibre swingarm which would be validated using the strains and displacements measured during experimental testing. The loads used during experimental testing were applied to the FE model during validation.

4. METHODOLOGY

A carbon fibre swingarm was developed using an initial laminate design. To determine which areas on the swingarm are inadequate from a design point of view, it was necessary to determine stiffness and strain characteristics from deflection and strain measurements and also to develop a FE model. This section describes the following:

1. The setup of the test rigs
2. The experimental tests
3. The development of the FE model
4. The FE simulations carried out on the swingarm

4.1 Experimental Equipment and Instrumentation

This section presents the equipment and instrumentation used in the vertical, lateral and torsional tests. The torsional and lateral tests have slight variations which are discussed in Sections 4.3 and 4.4. Table 1 presents the equipment and instrumentation used during testing and the figures that they appear in. The design and manufacture of the test rig was presented by Chacko [37].

Table 1. Equipment and instrumentation used in the test rig.

Component	Figures
Hydraulic jack for applying loads	17
Three brackets for rigidly mounting the swingarm	17 & 18
Two plummer block bearings	18
Chain for transmitting the load between the hydraulic jack and the load cell and swingarm	17
Load cell (50 kN) that provided the load readings. For the load cell calibration, see Appendix B.	17
Rosette strain gauges (120 Ω) for measuring strain in the 0°, 45°, and 90° directions	20 and 115 to 129
NI data acquisition hardware	130
LabView software for reading and recording strain measurements	-
Computer	-
Dial gauges for measuring deflection	17

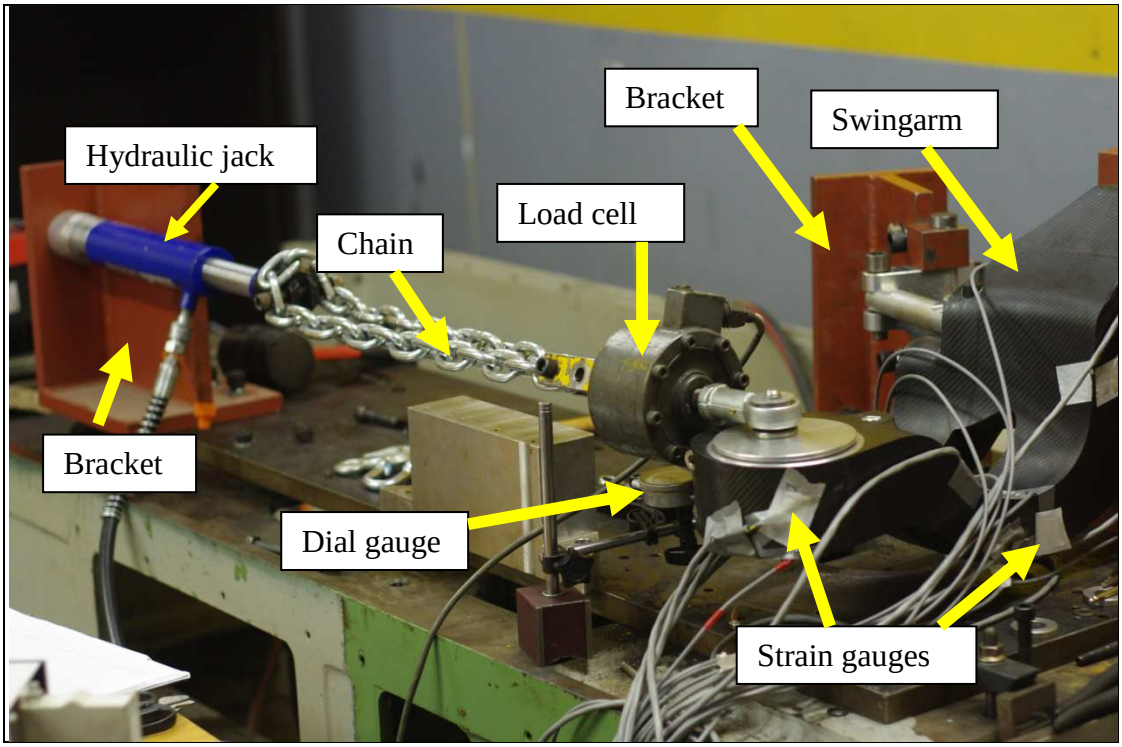


Figure 17. Test rig showing various components.

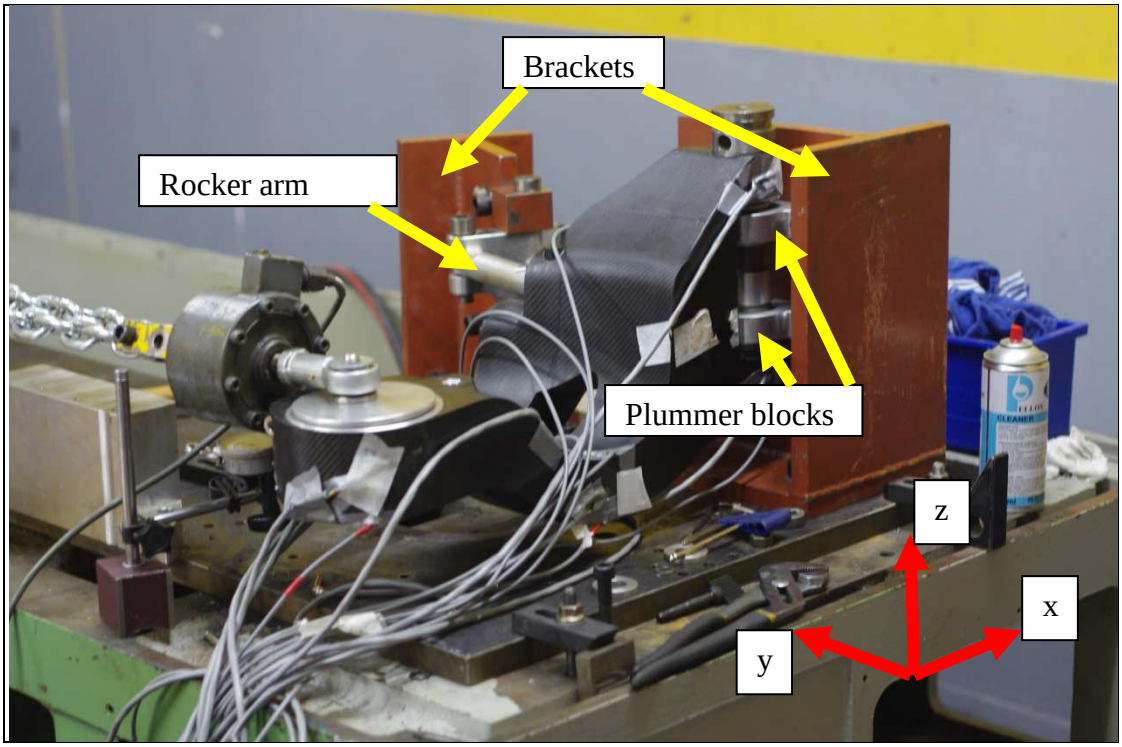


Figure 18. Test rig showing various components.

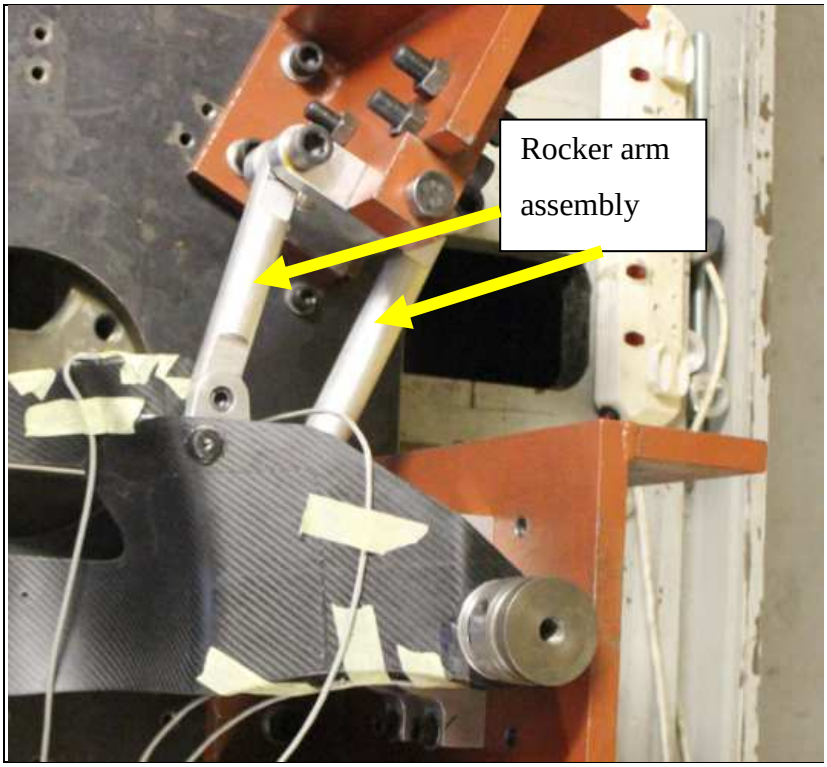


Figure 19. Connection from swingarm to rocker-arm.

The positioning of strain gauges is often based on the strain distribution obtained from FEA. In general, gauges are placed in areas showing a uniform and high strain field. In this case, due to the complexity of building an FE model of the swingarm, this approach was not taken. This was because it was not known if the FE model would present accurate enough results on which to base the positioning of the strain gauges. Therefore the gauge positioning was based on the following:

- Comparing the strain at the aluminium inserts with the strain in the middle of the swingarm.
- Looking at the type (tensile or compressive) and magnitude of the strain at the lower and upper arms of the swingarm.
- Assuming that the highest strains would generally occur on the top arm which is potentially the furthest distance from the neutral axis.

Rosette strain gauges (see Figure 20) were used to measure strain on the swingarm.

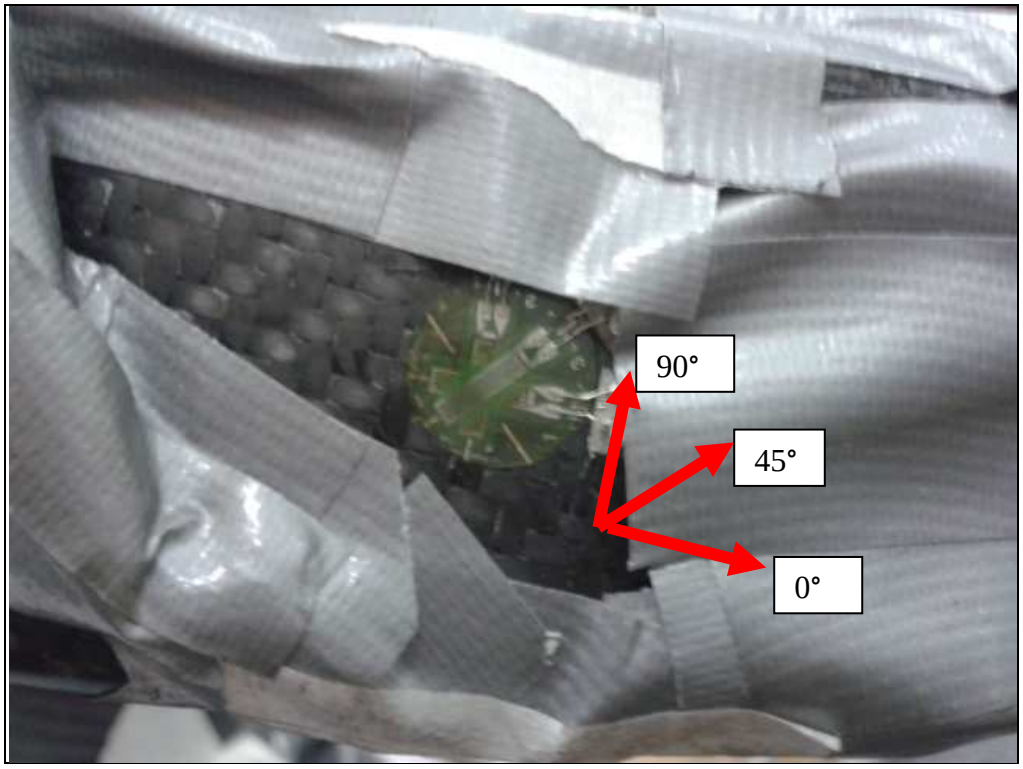


Figure 20. Rosette strain gauge.

Rosette strain gauges measure strains at zero, forty-five and ninety degrees which allows for measuring the strains along the zero degree and ninety degree axes of the carbon fibre laminate. These two directions correspond to the longitudinal and transverse directions of the fibre. As shown in Figures 21 and 22, the gauges were mounted at 8 positions on the swingarm.

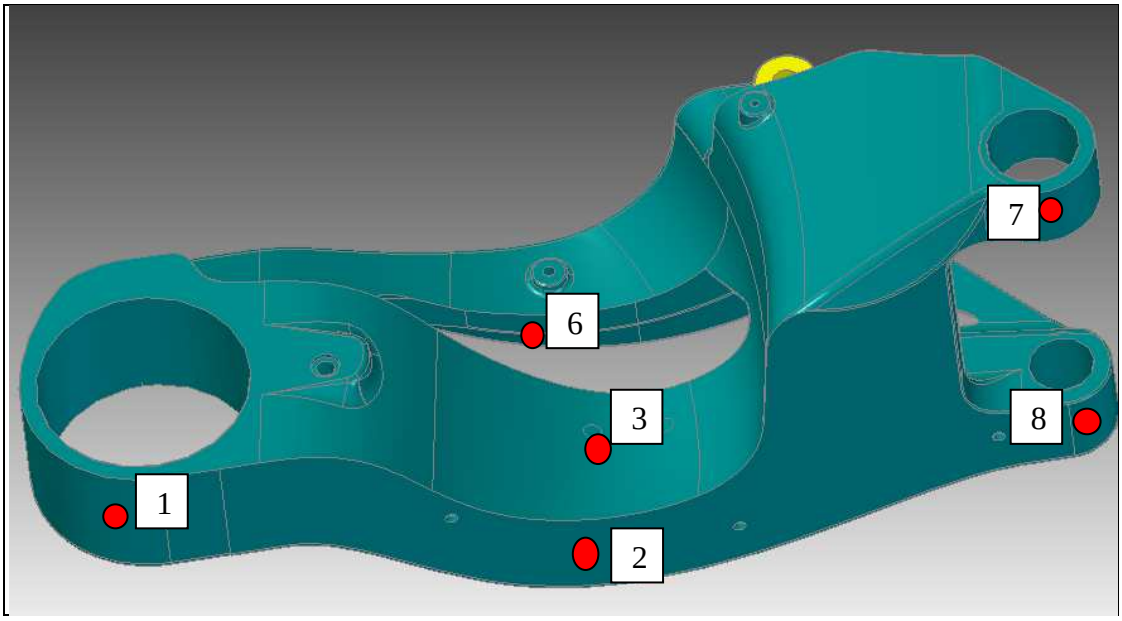


Figure 21. Strain gauge measurement positions.

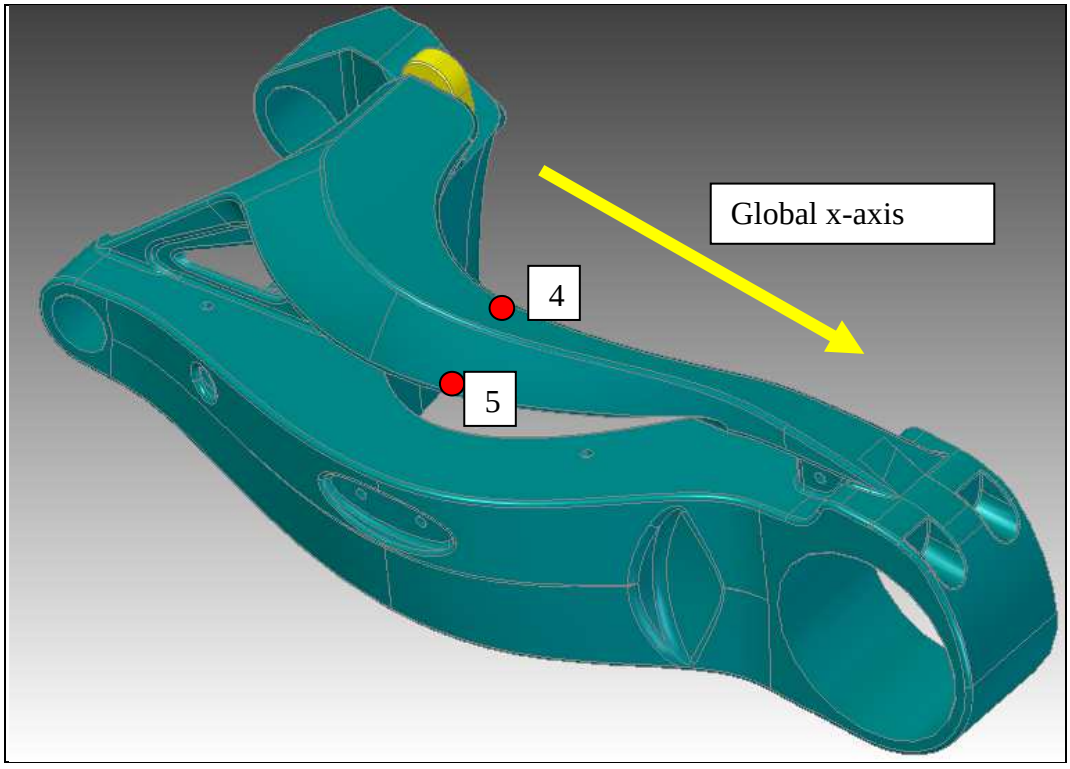


Figure 22. Strain gauge measurement positions.

Each strain gauge had its own local coordinate system. The zero degree (longitudinal) direction for each gauge was lined up with the global x-axis which corresponds to the longitudinal axis of the swingarm (Figure 22). The ninety degree (transverse) direction was aligned perpendicular to the longitudinal gauge direction and parallel to the surface on which the gauge was placed. The positioning of the strain gauges can be seen in more detail in Appendix D.

4.2 Experimental Rig Setup and Loading – Vertical Testing

This section describes the set-up of the test rig that applied loading to the swingarm in the swingarm vertical plane. The test rig is shown in Figure 23. Although it shows the loads being applied to the swingarm in the horizontal plane via the hydraulic jack, it actually simulates the vertical swingarm loads because the swingarm is rotated through 90° on the test rig.

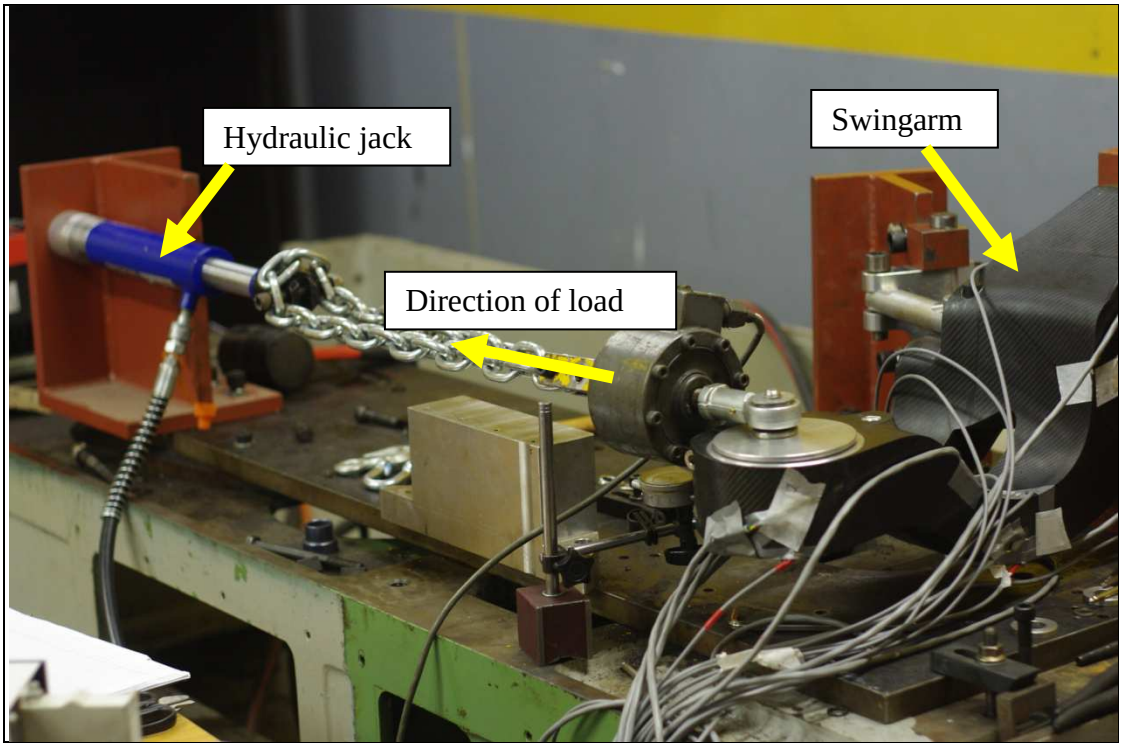


Figure 23. Swingarm test rig to apply vertical load.

More detail with respect to the manner in which the swingarm was attached to the rig is discussed under Section 4.5.5 when describing the constraints for the FE model. In the vertical test, loads of between 0 N and 8000 N were applied in increments of 1000 N. The aim was to include the range of loads in the Leyni Test and also to apply a wider range of vertical loads on the swingarm to determine the stiffness characteristics.

4.3 Experimental Rig Setup and Loading – Torsional Testing

This section describes the setup of the rig during torsional loading of the swingarm (see Figure 24). The aim of this test was to apply a torsional load to the swingarm in order to calculate the torsional stiffness and to measure strain. The equipment, instrumentation and positions of the strain gauges are the same as that used during the

vertical loading. The difference here is that a vertical steel shaft[3] was attached to the wheel mount and the hydraulic jack was elevated in order to apply the loads at a distance from the longitudinal axis. This resulted in a moment about the longitudinal axis of the swingarm. From the reader's perspective, the longitudinal axis goes into the page.

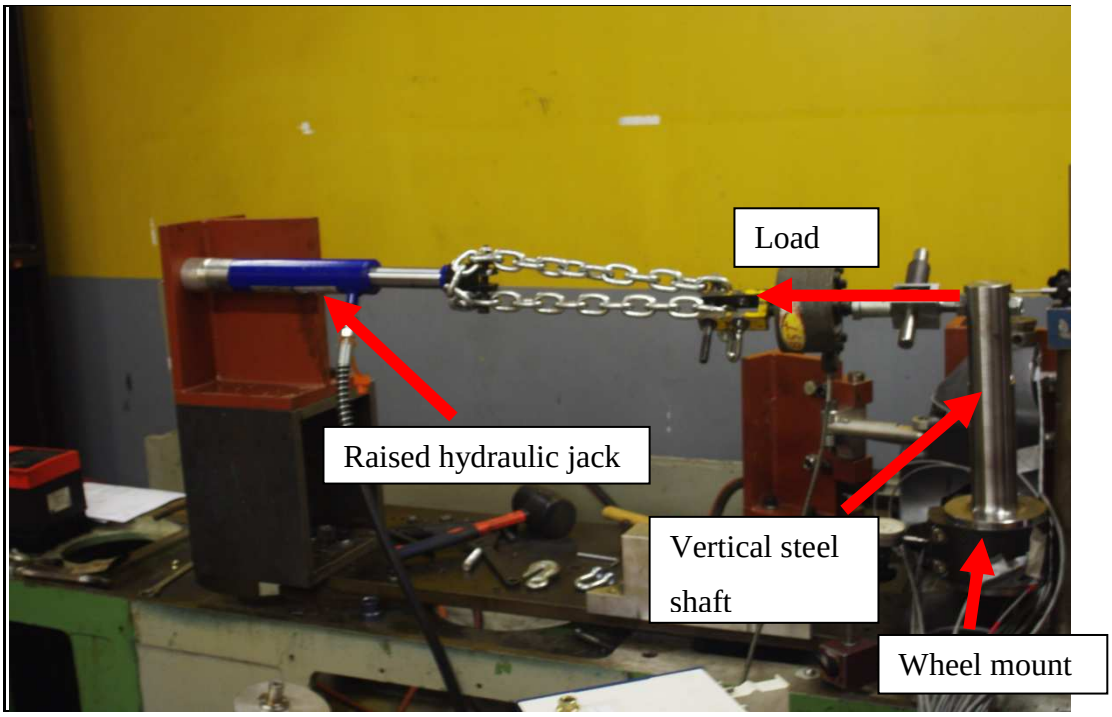


Figure 24. Rig setup to apply a torsional load on swingarm.

The torsional loading was based on the work carried out by Risitano et al. [5] and the aim of these tests was to determine the torsional stiffness of the swingarm by applying a moment and calculating the angle of rotation. Risitano et al. applied loads of between 0 and 400 Nm and measured the deflection angle for each load application. The loads applied during the current test included this range but went up to 680 Nm. Figure 25 shows that due to a single force being applied at a perpendicular distance from the longitudinal axis, a force and couple moment act at the wheel mount [38].

[3] For more detail on the design of the vertical steel shaft, see Appendix E.

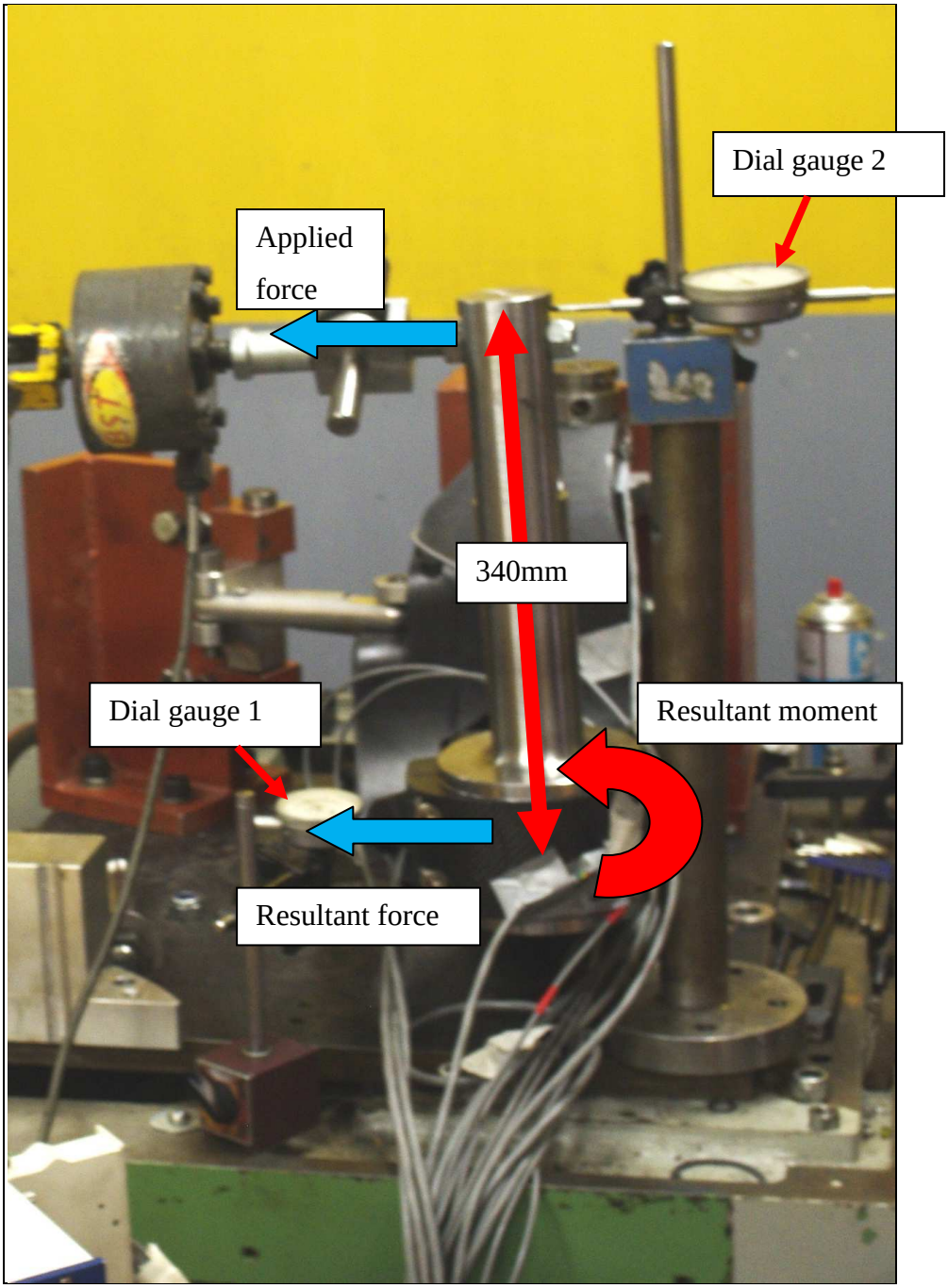


Figure 25. Test rig showing the steel arm used in the torsional test.

The length of the moment arm was 340 mm and the range of forces was between 0 N and 2000 N in increments of 100 N. Equation 4-1 presents a sample equation showing how the moment was calculated using a force of 100 N.

$$M = Fd$$
$$= 100 \times 0.34 \qquad (4\text{-}1)$$
$$= 34 \text{ Nm}$$

Where: M = Moment [Nm],

F = Load applied on the vertical steel arm [N], and

d = Length of moment arm [m].

Therefore based on the methodology above, Table 2 presents the range of forces and moments that were applied.

Table 2. Forces and moments applied during torsional test.

Force [N]	Moment [Nm]	Force [N]	Moment [Nm]
100	34	1100	374
200	68	1200	408
300	102	1300	442
400	136	1400	476
500	170	1500	510
600	204	1600	544
700	238	1700	578
800	272	1800	612
900	306	1900	646
1000	340	2000	680

As discussed earlier, due to the applied force not being a couple[4], a resultant force occurs at the wheel mount. Therefore a deflection not only occurs at the top of the arm but also at the wheel mount. When measuring the angle of rotation, the deflection at the top of the steel arm and the deflection at the wheel mount were both taken into account (hence the need for two dial-gauges shown in Figure 25). To present the method of calculating the angle of rotation, a schematic is presented in Figure 26. During loading, both the top of the steel arm and the wheel mount deflect

[4] A couple is defined as two parallel forces that have the same magnitude but opposite directions and are separated by a perpendicular distance [34].

to the left. In order to obtain the net deflection at the top of the arm, the deflection s_1 at the wheel mount, was subtracted from the deflection s_2 at the top of the arm. The two dial-gauges were used to measure deflection at the bottom and at the top.

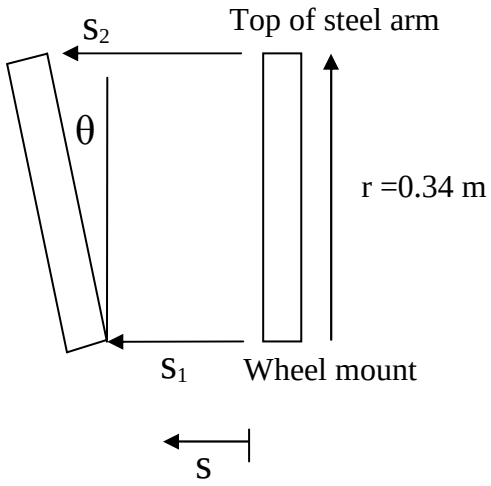


Figure 26. Schematic of deflection of steel arm during torsional loading.

The resultant deflection was divided by the radius 0.34 m as shown in Equation 4-2 to calculate the angle of rotation.

$$\theta = \frac{(s_2 - s_1)}{r} \tag{4-2}$$

Where: θ = Angle of rotation [rad],
s_1 = Deflection measured at wheel mount [m],
s_2 = Deflection measured at top of steel arm [m], and
r = Radius [m].

The torsional stiffness was then calculated using Equation 4-3

$$k_t = \frac{M}{\theta} \tag{4-3}$$

Where: k_t = Torsional stiffness [Nm/rad],
M = Moment [Nm], and
θ = Angle of rotation according to Equation 4-2 [rad].

The units of the the torsional stiffness were converted to Nm/deg by multiplying by π [rad]/180 [deg].

4.4 Experimental Rig Setup and Loading – Lateral Testing

Due to the swingarm being rotated 90° about the longitudinal axis, in order to simulate a lateral load, a vertical load was applied at the wheel mount. As shown in Figure 27, the hydraulic jack was disconnected and weights were simply placed on the wheel mount which would apply a load vertically downwards.

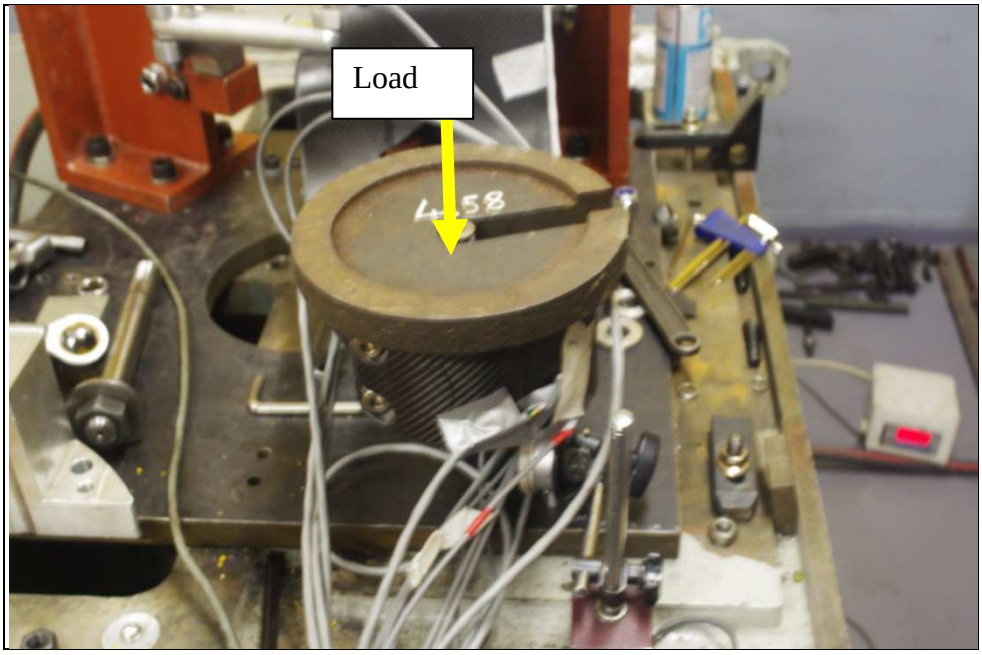


Figure 27. Rig setup for applying lateral loads in the global z-direction.

The range of loads was based on work carried out by Armentani et al. [8] who calculated a maximum lateral load of 125 N. In the current test, a load of up to 133.4 N was applied. Three mass pieces of 4.58 kg, 4.53 kg and 4.49 kg were used to apply increasing loads as shown in Table 3. The deflection was measured at each load increment using a dial gauge positioned at the bottom of the wheel mount as shown in Figure 28.

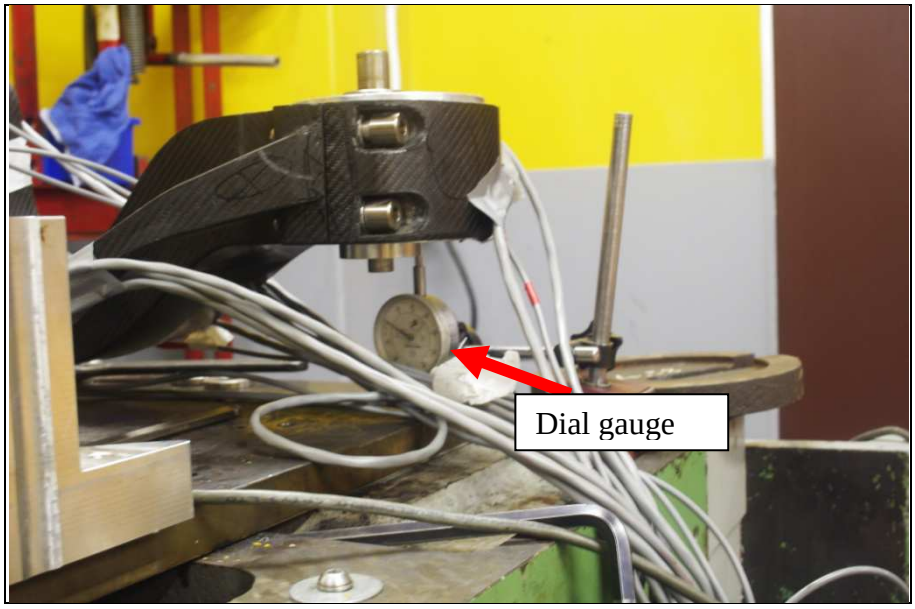


Figure 28. Position of dial gauge during lateral loading test measuring the lateral deflection.

Table 3. Loads applied during lateral test.

Load	Total mass [kg]	Total weight [N]
1	4.58	44.9
2	4.58+4.53 = 9.11	89.4
3	9.11 + 4.49 = 13.6	133.4

4.5 Development of the Finite Element Model

The carbon fibre swingarm is an intricately manufactured component. The laminae are laid up by hand and several different areas, or zones, occur on the swingarm with different layups. A layup (or stackup) is a number of laminae (or plies) overlaid on each other, each potentially having a different fibre orientation and type of weaving (such as unidirectional or woven). For example, a layup could have three unidirectional plies with fibre orientations of -45°, 0°, 45° where the angle is measured according to a reference axis. The carbon fibre swingarm has a number of different layups consisting mainly of two types of carbon fibre plies, a 300 g/m^2 unidirectional fibre and a 380 g/m^2 woven fibre.

4.5.1 Software

ANSYS Composite PrepPost together with ANSYS Static Structural was used in the FEA (Figure 29). ACP (Pre) was used for pre-processing (creating the composite layups) and ANSYS Static Structural was used to apply the mesh and boundary conditions, to solve the simulations, and also to view the deflection and strain results.

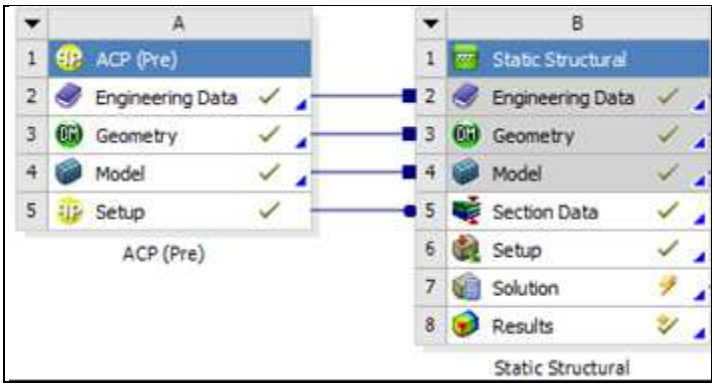


Figure 29. ANSYS Workbench Project Schematic showing the three parts of the simulation.

4.5.2 Assumptions

To develop the finite element model, it was necessary to first determine the various zones on the swingarm and the type of layup that made up each zone. Once that information was obtained, various initial assumptions were made:

- Only the most significant zones with their layups were modelled. Due to the complex shape of the swingarm and the large number of zones, to simplify the modelling, the smaller zones (which had slight differences in layup to the larger more significant zones) were modelled with the same layup as the larger zones.
- Lamina overlap was not modelled due to its complexity. Plies were modelled essentially assuming butt joints. For more discussion on ply overlap, see Appendix C.
- The aluminium inserts (shown in Figure 30) were not modelled. The aim of the simulation was to get an overall impression of the effects of the loadings and the aim of leaving out the inserts was to simplify the FE model.



Figure 30. Swingarm showing the aluminium inserts.

Furthermore, the supplier supplied limited information on the material properties and therefore standard properties for both the unidirectional and woven plies were assumed which are presented in Table 4. The approximate thickness of each ply is also given.

Table 4. Material properties of the carbon fibre plies used in the FE model.

Material	E_1 [GPa]	E_2 [GPa]	G_{12} [GPa]	υ	Thickness [mm]
Unidirectional (300 g/m^2)	135	10	5	0.3	0.3
Woven (380 g/m^2)	70	70	10	0.1	0.38

4.5.3 Model Preparation and Mesh Generation

ANSYS DesignModeler was used for modifying and preparing the swingarm solid model for FEA in ANSYS. First the solid model was transformed into a surface model to allow for later modelling of shell elements. Further preparation included repairing holes, sharp angles and edges which allowed for a better FE mesh to be created. The model was also sectioned for modelling the various layups and applying the various loads using the Named Selection function in ANSYS. After model preparation, the mesh was generated as shown in Figure 31. The mesh consisted of triangular and quadrilateral shell elements with 51,694 nodes and 52,295 elements.

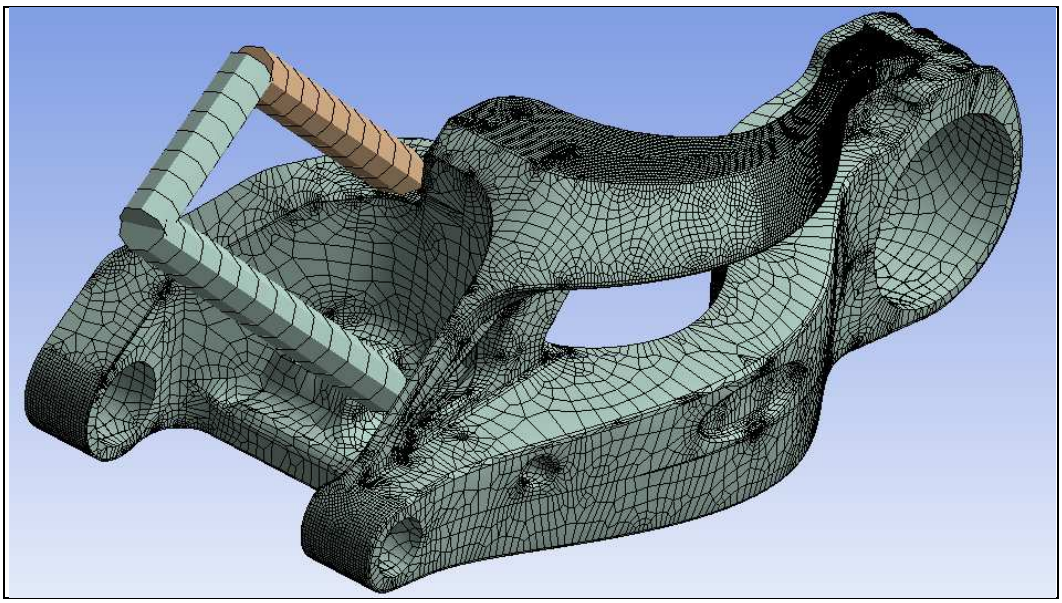


Figure 31. Finite element mesh on the swingarm

The element type used in the mesh was a SHELL181 which is a 4-node structural shell suitable for analyzing thin to moderately thick shell structures. It has six degrees of freedom at each node: translation in the x-, y- and z-directions, and rotations about the x-, y- and z-axes. The element is used for layered applications for modelling composite shells.

4.5.4 Creation of the Layups

The various zones made it possible to create the carbon fibre layups in ANSYS ACP (Pre). Before creating the layups, the types of material used in the layups, namely the 380 g/m^2 woven fibre and 300 g/m^2 unidirectional fibre, were defined with their material properties. Thereafter a specific layup for each zone was created based on the number of plies used, the type of plies and each ply's orientation. The main zones

covering the top and bottom arms[5] of the swingarm are presented in Figures 32 through 39. As discussed earlier, the smaller zones with their layups were included in these larger more significant zones with their layups shown in these figures.

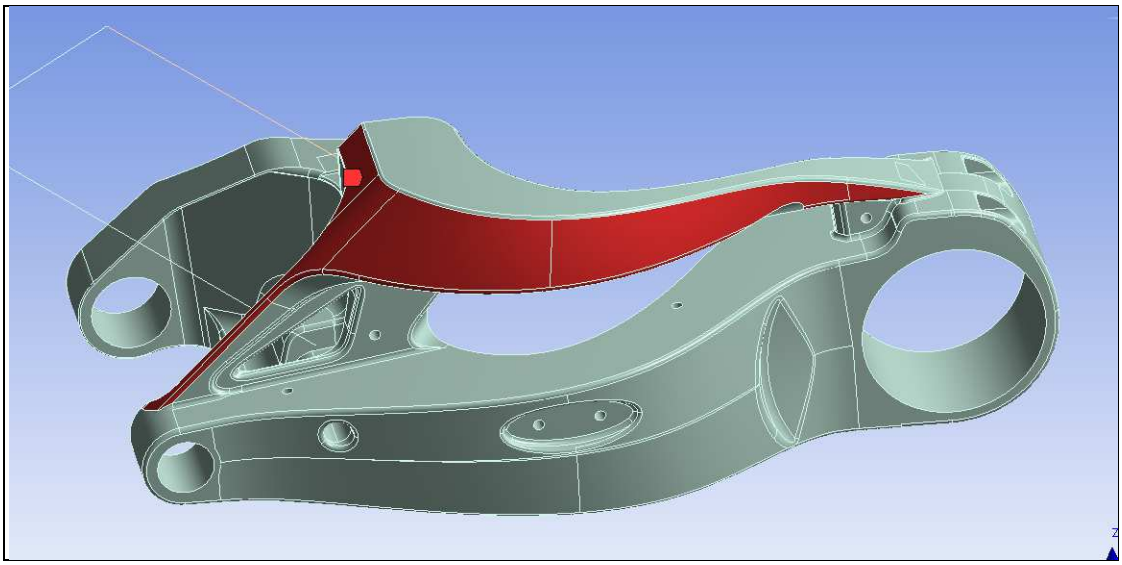


Figure 32. Outer zone of the top arm.

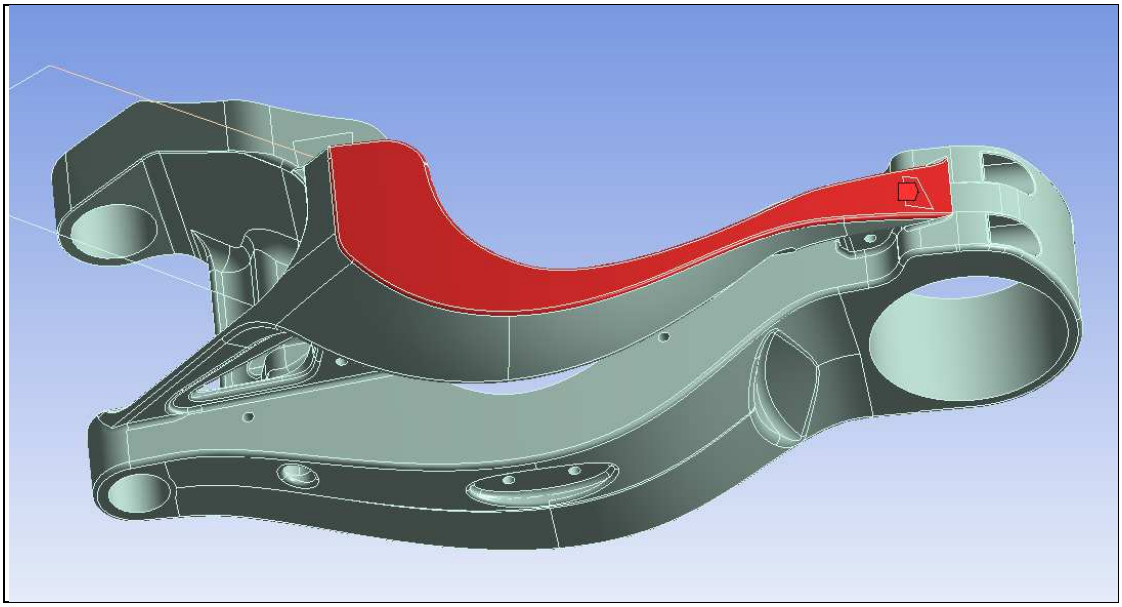


Figure 33. Top zone of the top arm.

[5] Not all the zones are shown here. The aim is to give the reader an indication of the method of zoning to create layups in those areas.

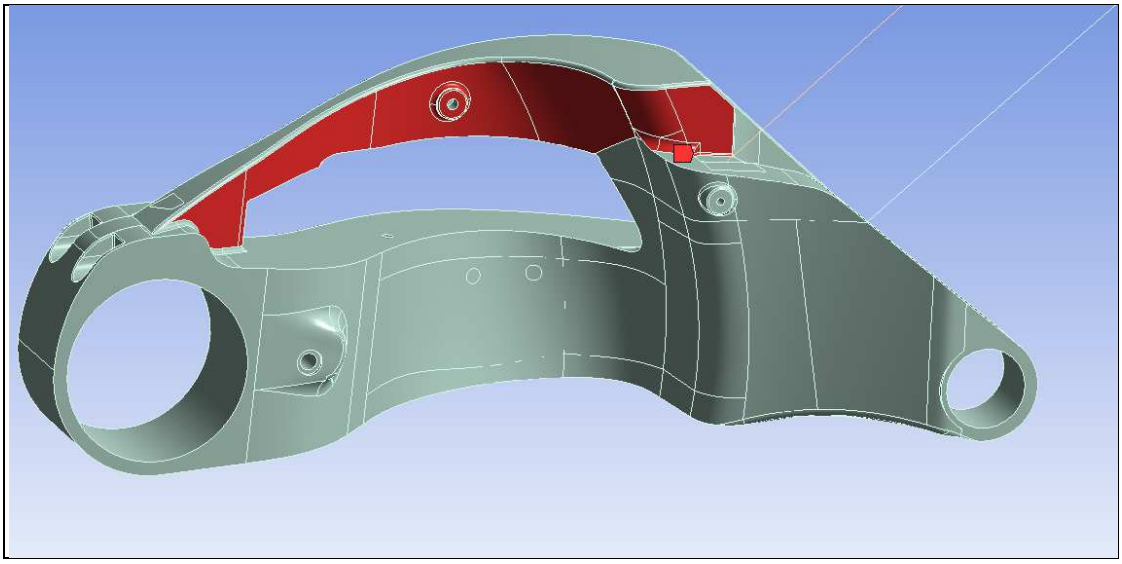


Figure 34. Inside zone of the top arm.

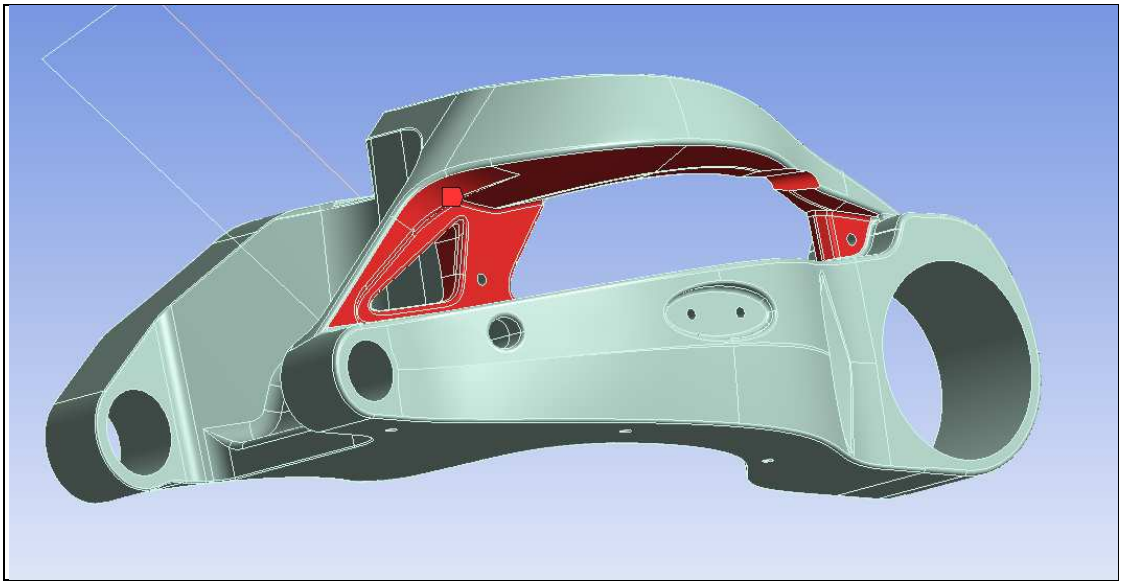


Figure 35. Zone underneath the top arm.

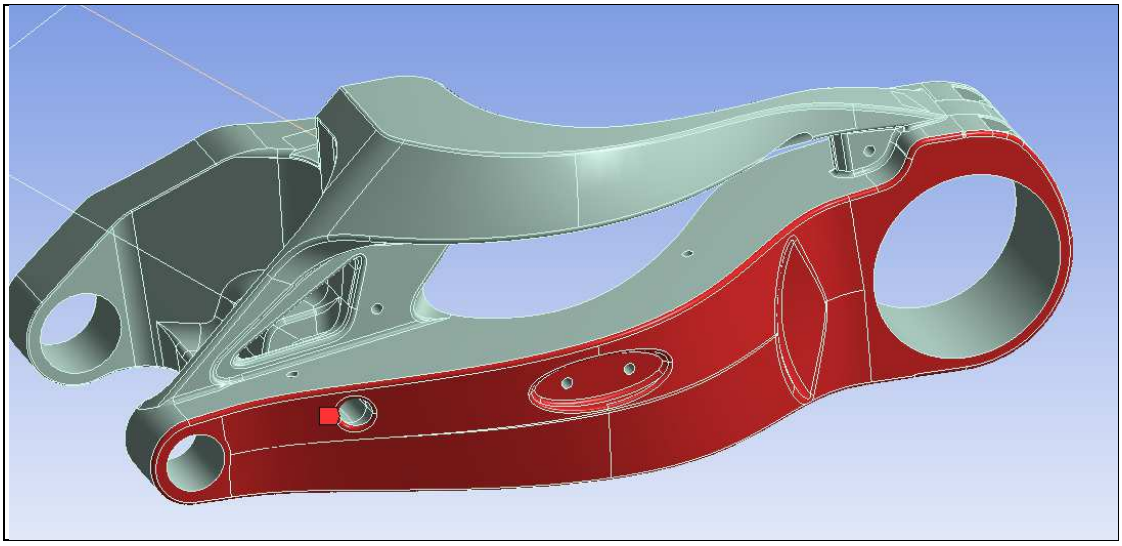


Figure 36. Zone on outside of bottom arm.

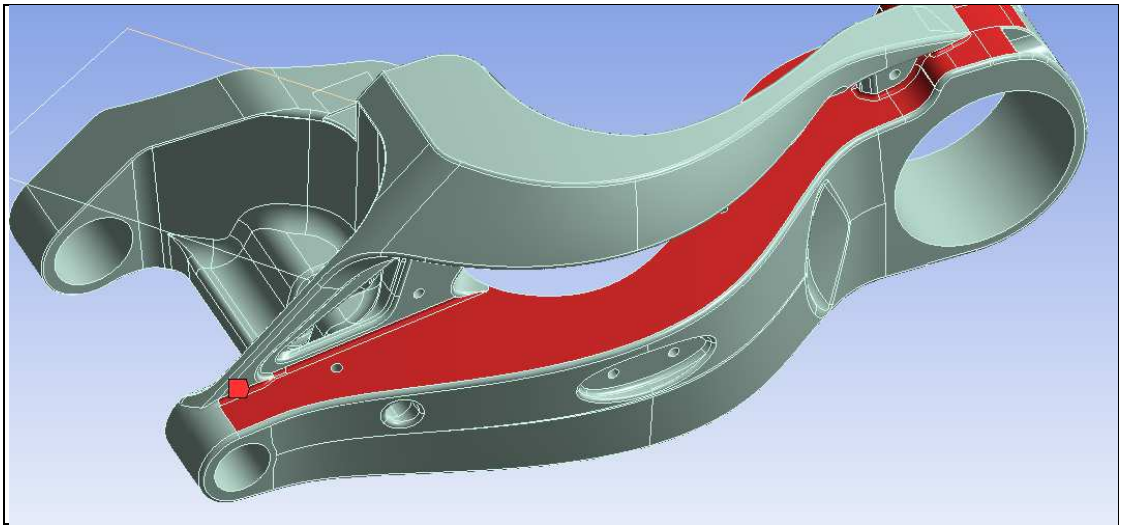


Figure 37. Top zone of the bottom arm.

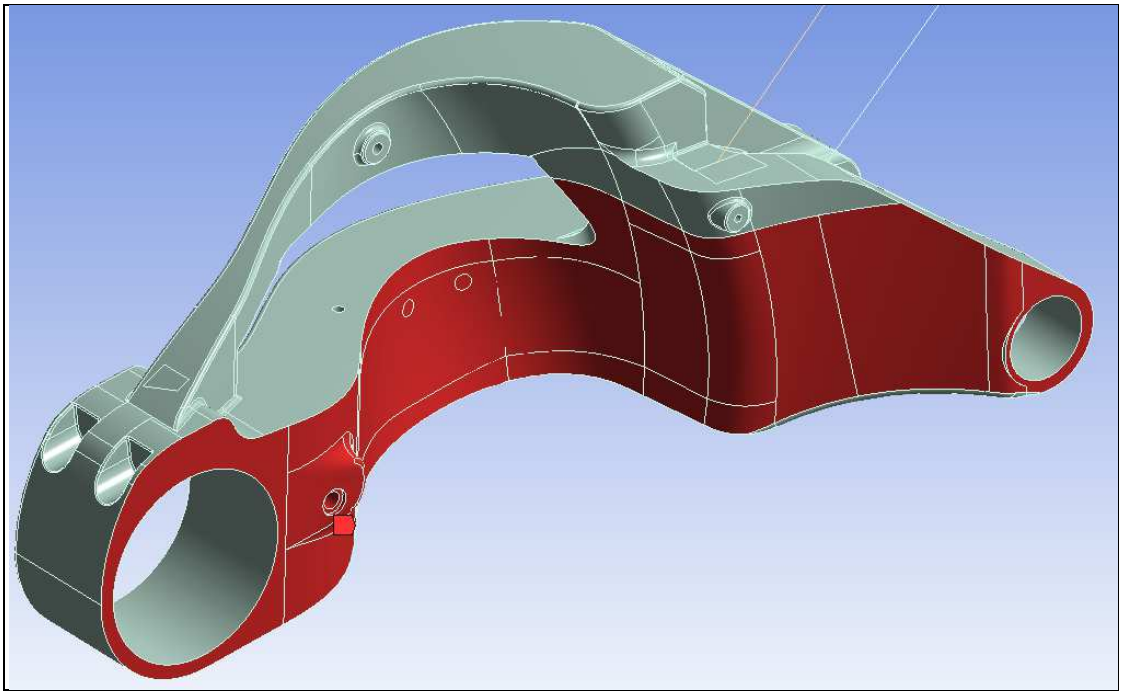


Figure 38. Inside zone of the bottom arm.

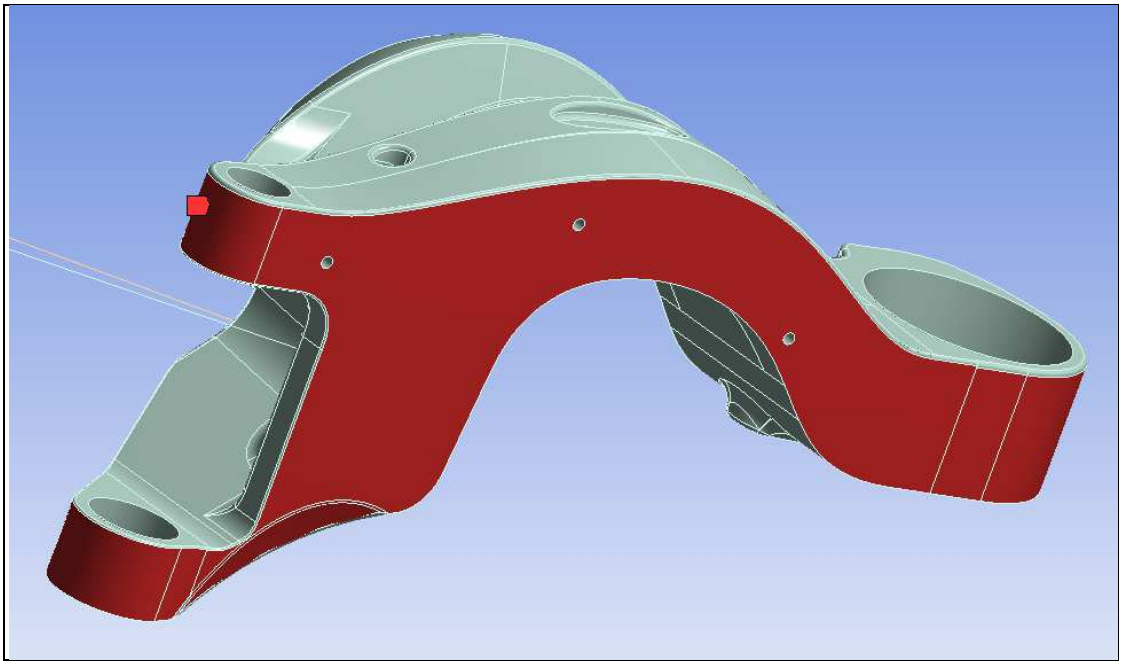


Figure 39. Underside zone of the bottom arm.

4.5.5 FE Model Boundary Conditions

Figure 40 shows a solid model of the test rig assembly with the aim being to present the constraints on the swingarm and how they were applied in the FE model. The rig

was built to simulate how the swingarm is mounted to the motorcycle. Point A shows the wheel mount position where the vertical, lateral or torsional loads were applied

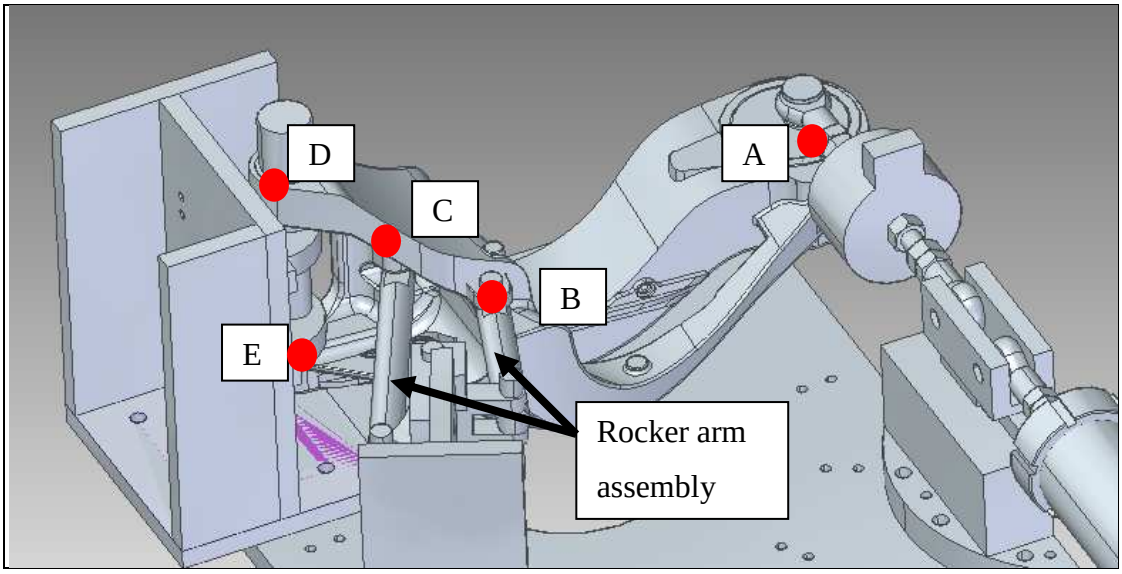


Figure 40. Positions of loading and constraints on the swingarm.

Points D and E represent where the swingarm is mounted to the main motorcycle chassis via bushes. These constraints were modelled in the FE model as cylindrical supports which only allow rotation about the pivot axis and no translation in any direction. The pivot axis here is essentially from Point D to E which is the axis about which the swingarm pivots. Points B and C indicate where the swingarm was connected to the rocker arm assembly via revolute joints. Figures 41 and 42 show close-ups of the rocker arm assembly which consists of two rigid aluminium links connected to an aluminium cross member.

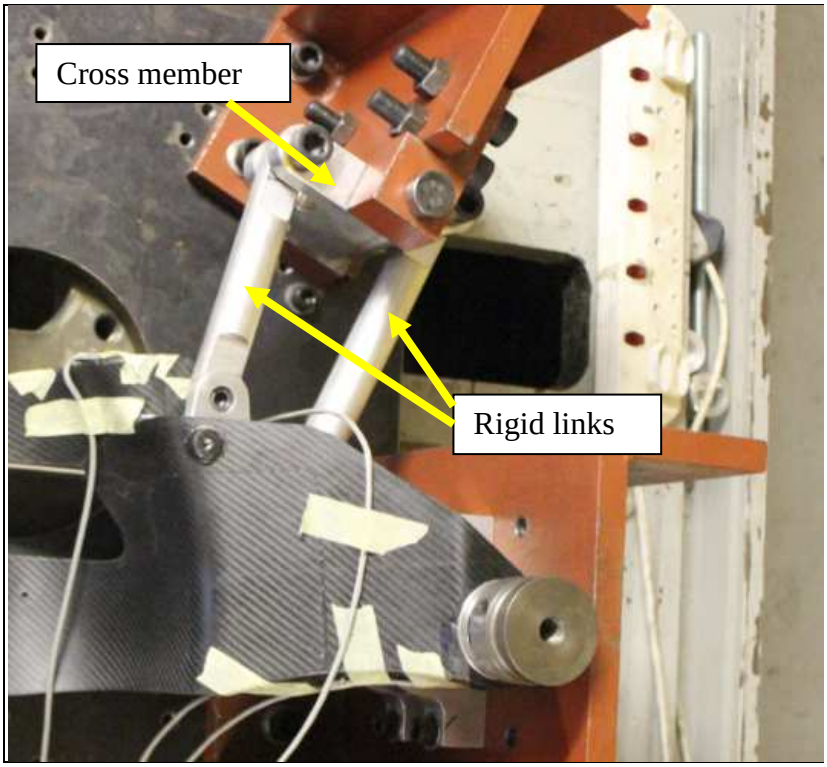


Figure 41. Rocker arm assembly.

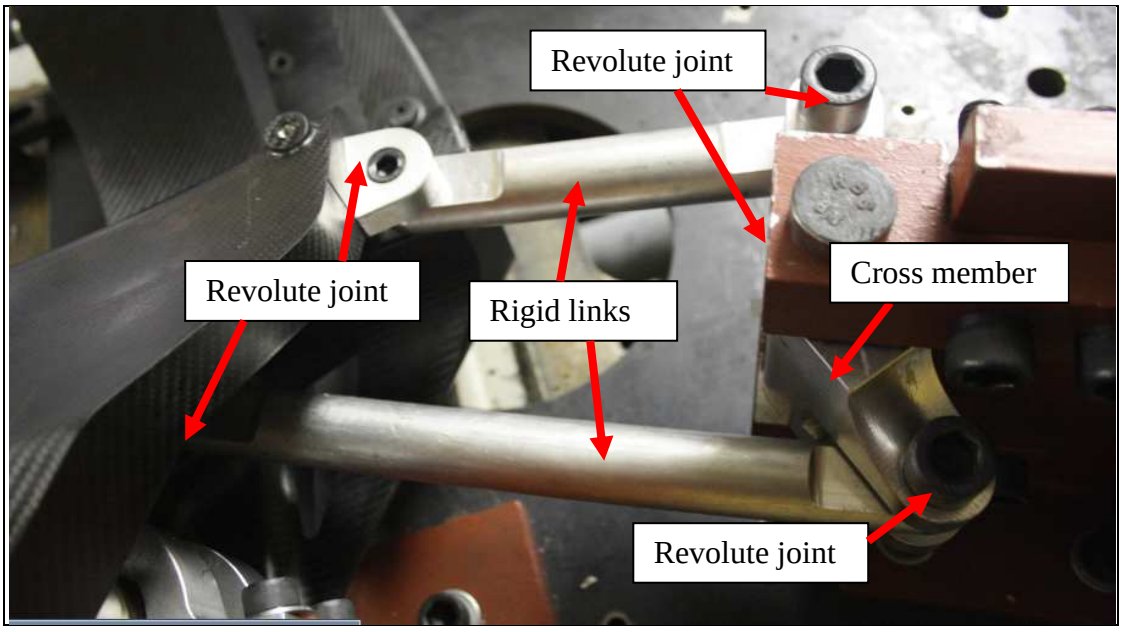


Figure 42. Rocker arm assembly.

It is important to note that the centre of the cross member also acts as a pivot point where only rotation about the axis coming out of the page is free. Every other rotation and translation is fixed.

The rocker arm was modelled using line bodies and each line body was designated a certain length, material and cross section to simulate the aluminium links in the rocker

arm assembly. Figure 43 shows the FE model with the line bodies representing the rocker arm assembly. The parallel rocker arm links were attached to the main swingarm using revolute joints which allow the links to rotate about an axis parallel to the swingarm pivot axis. The parallel arms were attached to the cross member also with revolute joints allowing rotation about the pivot axis. The cross member was then attached to ground also via a revolute joint at its centre. The revolute joint allows for rotation about the axis parallel to the pivot axis and is constrained in every other translational and rotational direction. The figure presents the revolute joints as red dots and the centre of the cross member is attached to ground.

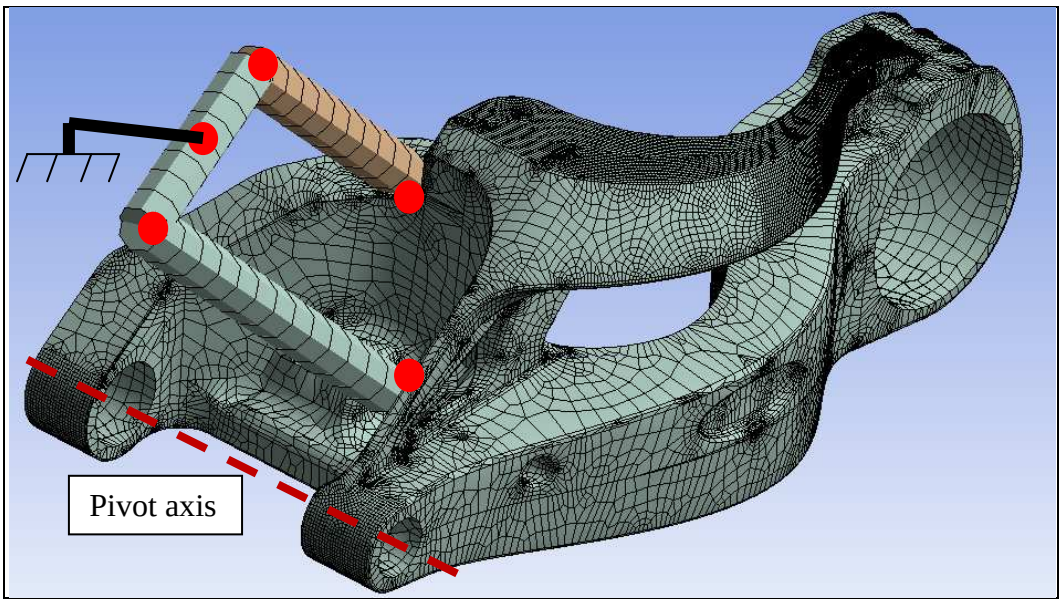


Figure 43. Finite element model of swingarm showing the rocker arm. The red dots indicate the positions of the revolute joints.

4.6 Finite Element Analysis –Vertical Testing

During the vertical loading simulations, due to being linear, the FE model was subjected to the maximum load of 8000 N in the vertical plane as shown in Figure 44 and deflection and strains were determined. The results were compared with the deflection and strain measurements obtained during experimental testing.

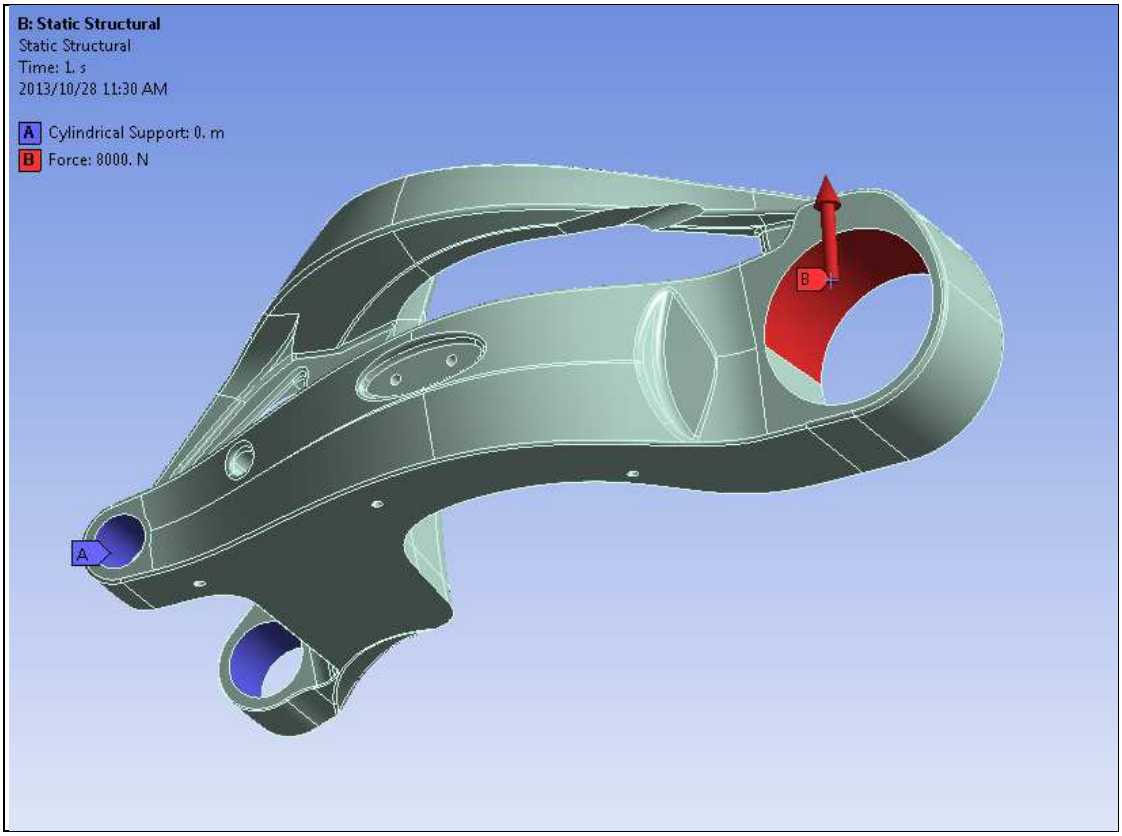


Figure 44. FE model showing constraints applied during vertical loading.

4.7 Finite Element Analysis –Torsional Testing

The FE model was subjected to the maximum moment of 680 Nm about the longitudinal x-axis as discussed in Section 4.3. Due to the force applying both a moment about the longitudinal axis and a resultant force in the motorcycle vertical direction, both a force and a moment were applied as shown in Figure 45. The aim of this simulation was to calculate the strains and deflection due to the torsional load and compare it with the experimental values.

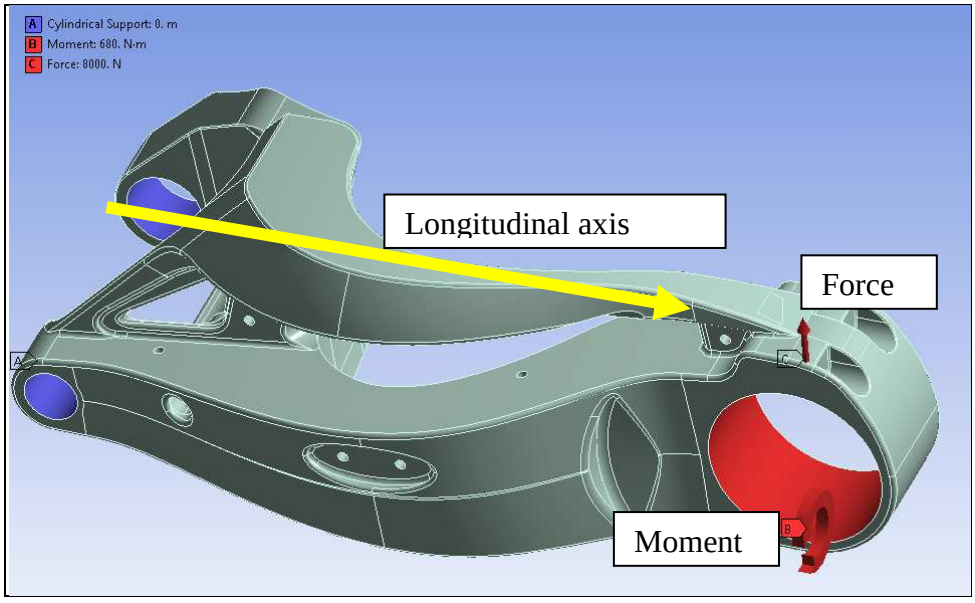


Figure 45. FE model subjected to a moment about the longitudinal x-axis and a force in the motorcycle vertical direction.

4.8 Finite Element Analysis –Lateral Testing

The maximum lateral force of 133.4 N was applied to the FE model to simulate the maximum load applied in Section 4.4. The FE model is shown in Figure 46. The aim of this simulation was to compare the lateral deflection with the experimentally measured lateral deflection.

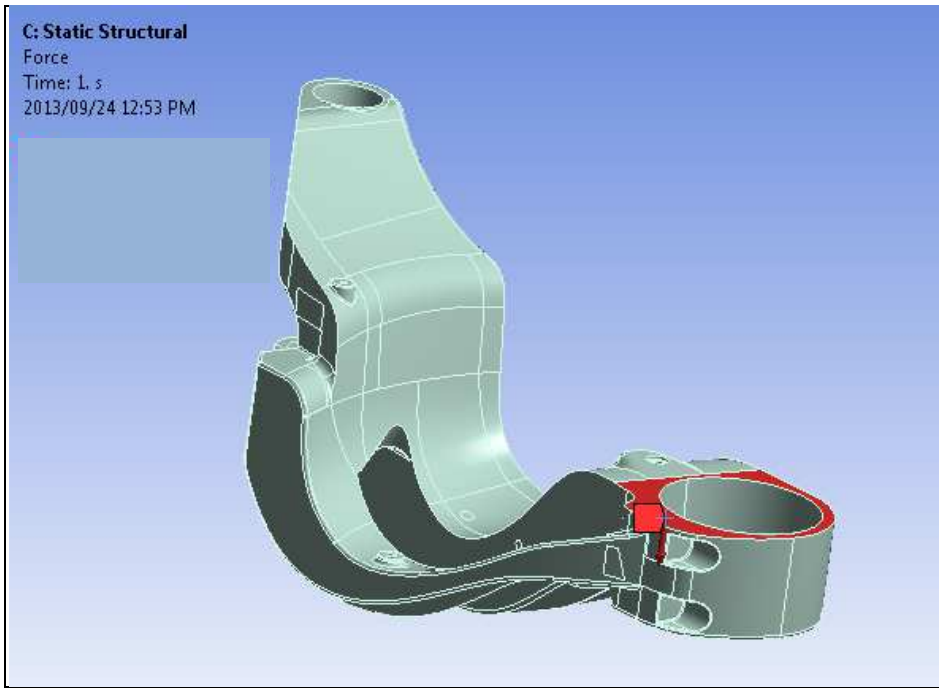


Figure 46. FE model subjected to a load in the motorcycle lateral direction.

5. RESULTS AND DISCUSSIONS

This section presents and discusses first the results from the experimental deflection and strain measurements. Thereafter the results from the FEA are discussed and compared with the experimental results.

5.1 Swingarm Deflection

The vertical deflection of the swingarm is shown in Figure 47 and is based on the experimental set-up discussed in Section 4.2. The first observation is that the swingarm exhibits a linear relationship between force and deflection within the range of loads applied. A maximum deflection of 15.85 mm was measured at the maximum load of 8000 N. Furthermore, Figure 47 shows the slope of the curve to be approximately 500 N/mm or 500 kN/m which represents the stiffness coefficient of the swingarm in the vertical direction.

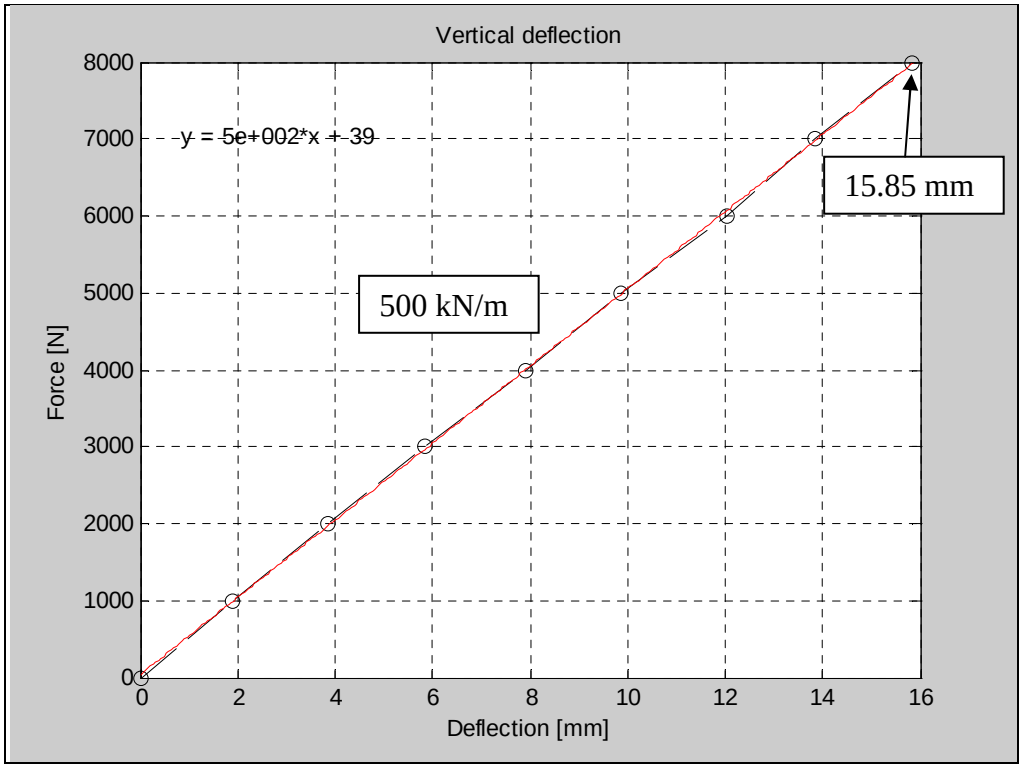


Figure 47. Vertical deflection of swingarm showing the vertical stiffness coefficient of 500 kN/m.

As discussed earlier, the swingarm and the spring of the rear suspension form two springs in series between the chassis and the wheel. The swingarm must therefore be rigid enough to not negatively affect the effective stiffness between the chassis and

the wheel. Consider two springs in series as shown in Figure 48, where k_{sp}, k_{sw} and k_{eff} represent the stiffness coefficients of the rear spring, swingarm and effective stiffness between the chassis and wheel, respectively. Typical values for rear springs on the Ducati are between 50 kN/m and 100 kN/m. Assuming a rear spring value of 50 kN/m the equation calculating the effective stiffness is as follows: $1/k_{sp} + 1/k_{sw} = 1/k_{eff}$. The effective stiffness is calculated as 45 kN/m. The swingarm therefore needs to have vertical rigidity considerably higher than that of the rear spring, in the region of ten times higher. Therefore it can be safely assumed that the effect that the carbon fibre swingarm will have on the effective stiffness between the chassis and the wheel will be minimal. This indicates that the larger the difference in the vertical stiffness between the rear spring and the swingarm, the closer the effective stiffness will be to that of the rear spring. Essentially the lower spring stiffness dominates the effective stiffness. It is concluded therefore that the swingarm has a sufficiently high rigidity to not negatively affect the rear spring.

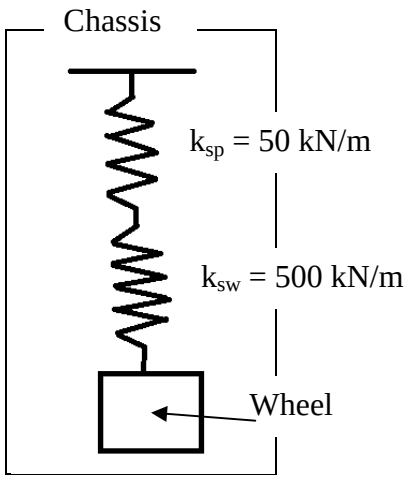


Figure 48. Schematic showing the rear spring and the swingarm as springs in series between the chassis and the wheel.

The vertical deflection of the swingarm was also measured during unloading, i.e. once the maximum load of 8000 N was reached, the load was decreased by 1000 N increments and the corresponding deflections were recorded. Figure 49 shows the vertical deflection during loading and unloading for two sets of tests that were carried out.

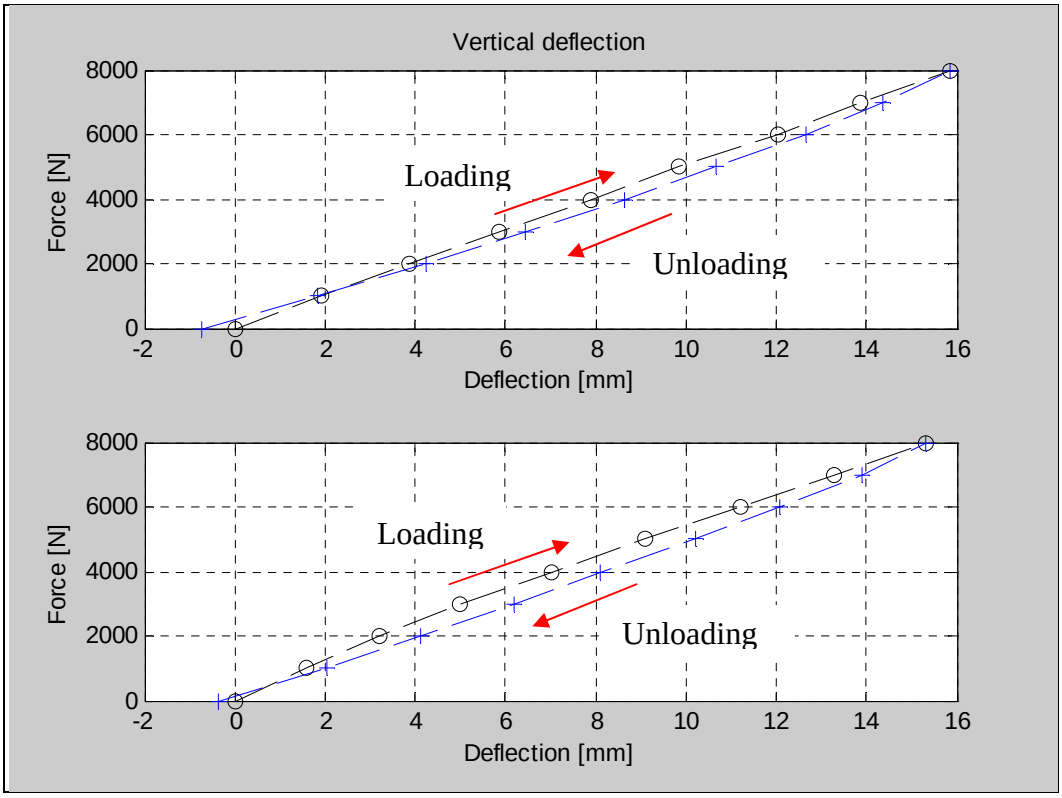


Figure 49. Deflection during loading and unloading of the swingarm

It can be seen that the loading and unloading curves exhibit a form of hysteresis. The unloading graphs show higher strains at the same load. What is interesting to see is that during the step from 1000 N to zero, both tests show that the swingarm deflection moves to a negative deflection from where it started (Figure 50). It would be expected that due to hysteresis there would be permanent strain in the swingarm. The reason for this may be due to slight play in the rig setup and possible overshoot due to inertial effects. The slight overshoot is approximately half a millimetre compared with the total deflection of approximately 16 mm.

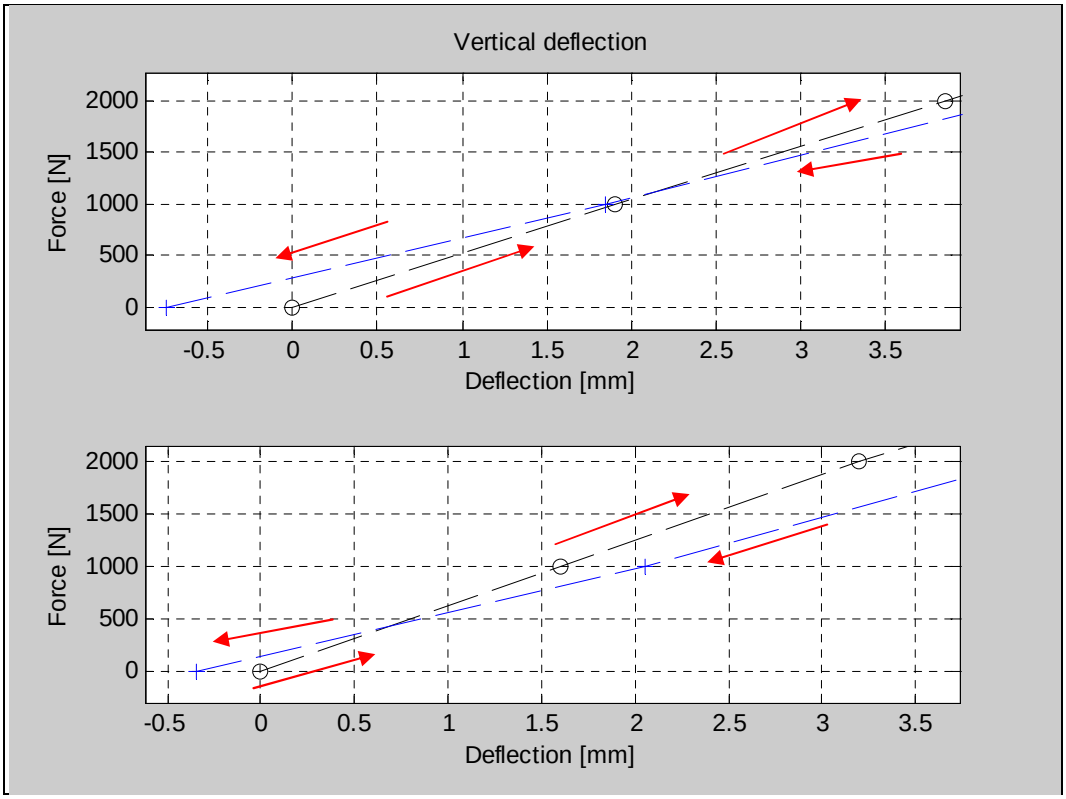


Figure 50. Deflection during loading and unloading near the zero load mark.

Figures 51 and 52 present the torsional deflection results based on the experimental set-up discussed in Section 4.3. Figure 52 shows a linear trendline to approximate the slope of the curve as 550 Nm/deg which represents the torsional stiffness coefficient of the swingarm.

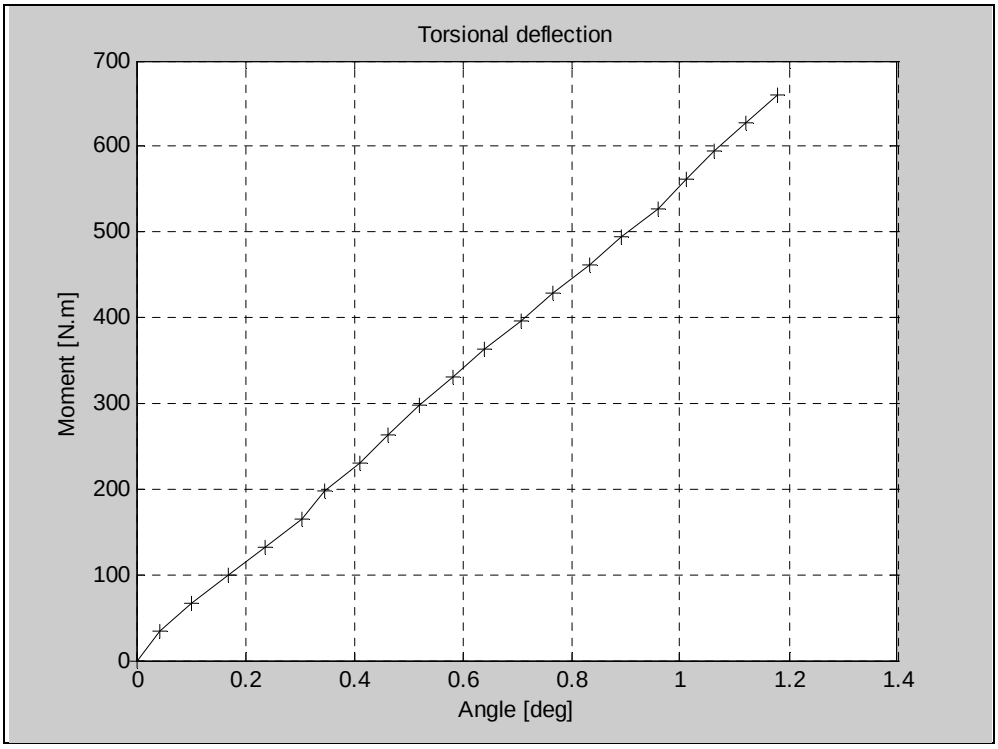


Figure 51. Torsional deflection of the swingarm.

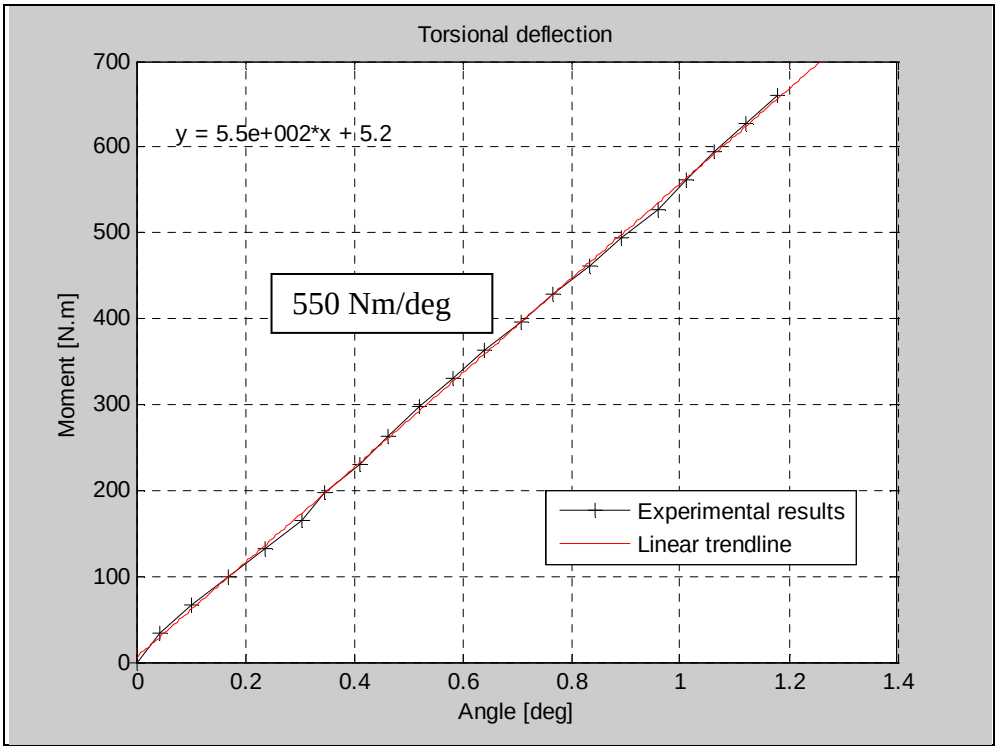


Figure 52. Torsional deflection of the swingarm showing the torsional stiffness coefficient of 550 Nm/deg.

This value appears to be approximately in the middle of the spectrum of values found in the literature (see Table 5).

Table 5. Comparison of torsional stiffness values obtained from the literature.

Designation	Torsional stiffness [Nm/deg]
Kawasaki ZX10R (Armentani et al.)	102.9
Suzuki GSX R1000 (Armentani et al.)	140.8
Honda CBR 1000R (Armentani et al.)	140.8
Sharp	209
Ducati Carbon Fibre	**550**
S2008 (Risitano et al.)	670
SM 2008 (Risitano et al.)	890
BNG 2008 (Risitano et al.)	1330
Cossalter	1000 - 2000

The 550 Nm/deg is higher than the 102.9 Nm/deg and 140.8 Nm/deg determined by Armentani et al. [8] and the 209 Nm/deg suggested by Sharp [29]. It is lower than those obtained by Risitano et al. [5] of 670 Nm/deg, 890 Nm/deg and 1330 Nm/deg and also lower than the typical values presented by Cossalter et al. of between 1000 Nm/deg and 2000 Nm/deg [10]. As discussed in Section 2.2, the values calculated by Armentani et al. were calculated without using a spacer and spindle to simulate real conditions. It was felt that the deflections calculated by Armentani et al. were higher than if real life conditions were simulated which means their stiffness values were lower. Due to the uncertainty of the torsional stiffness values calculated by Armentani et al., the carbon fibre swingarm was rather compared with the value of 209 Nm/deg by Sharp and the higher stiffness values mentioned above. This uncertainty shows the need to develop a standard method of testing both single-sided and double-sided swingarms to determine the stiffness characteristics.

Based on the value suggested by Sharp, the carbon fibre swingarm is stiff enough. However, when compared with the higher values determined by Risitano et al. and Cossalter, the rider may experience a “heavier” ride due to the lower torsional stiffness. Furthermore, as was discussed by Cossalter et al., lower torsional rigidity reduces weave mode stability at higher speeds. Therefore the results suggest the

carbon fibre swingarm may cause the motorcycle to experience lower stability in the weave mode at higher speeds than the other motorcycles.

Figures 53and 54 show the torsional loading and unloading for two different tests. Hysteresis is shown to occur in the swingarm which could add to the torsional damping.

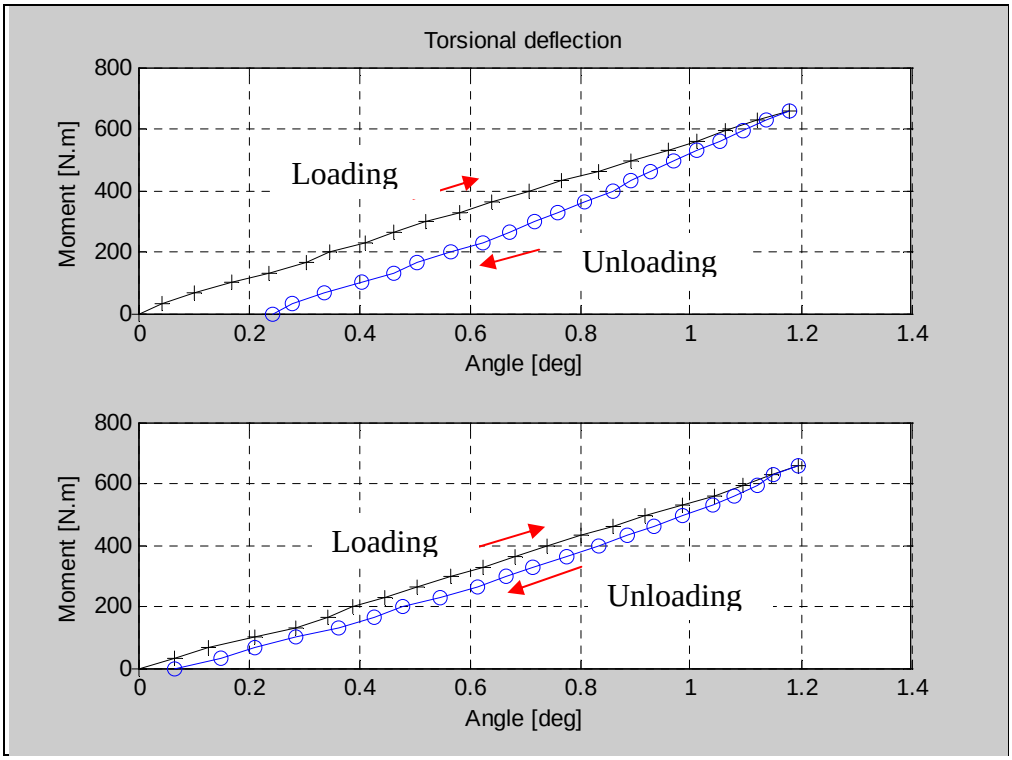


Figure 53. Torsional deflection of swingarm during loading and unloading during two torsional tests.

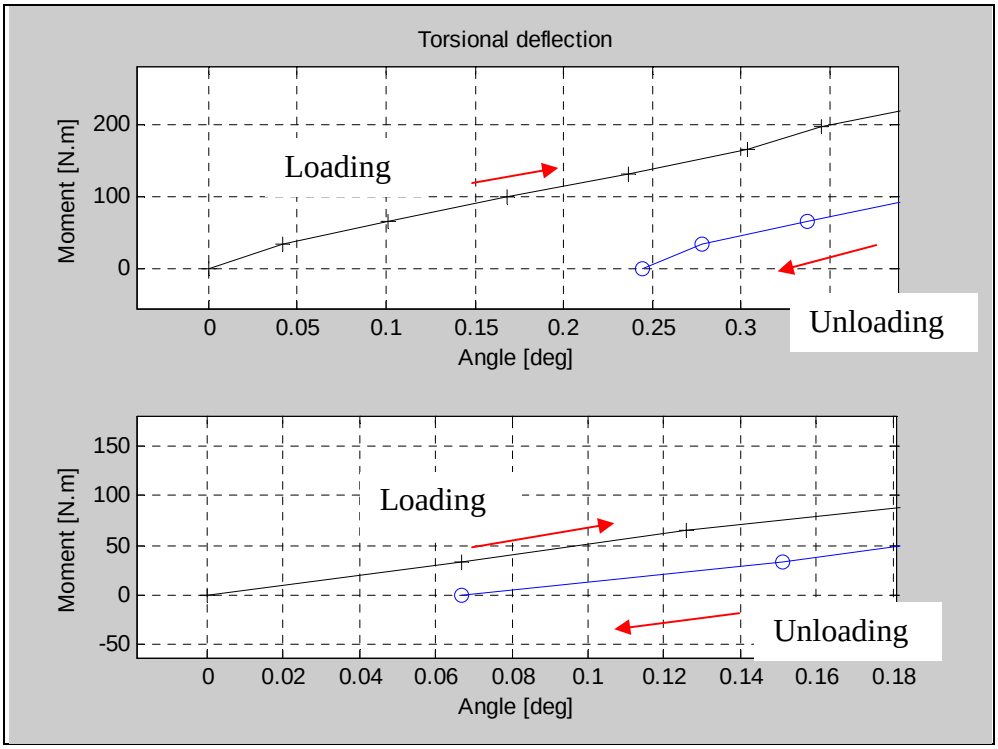


Figure 54. Torsional deflection during loading and unloading near the zero mark.

The lateral deflection (based on Section 4.4) of the swingarm is presented in Figures 55 and 56 with Figure 56 adding a linear trendline approximating the slope of the curve. The slope of the curve represents the lateral stiffness coefficient equal to approximately 445 N/mm (445 kN/m).

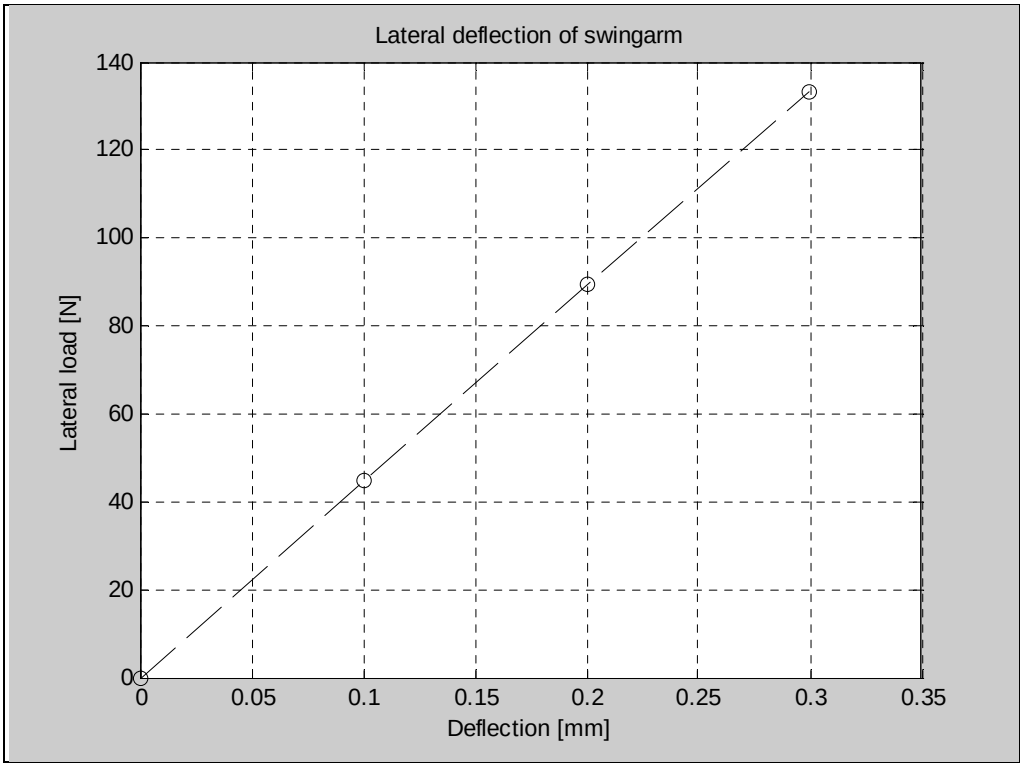


Figure 55. Lateral deflection of the swingarm.

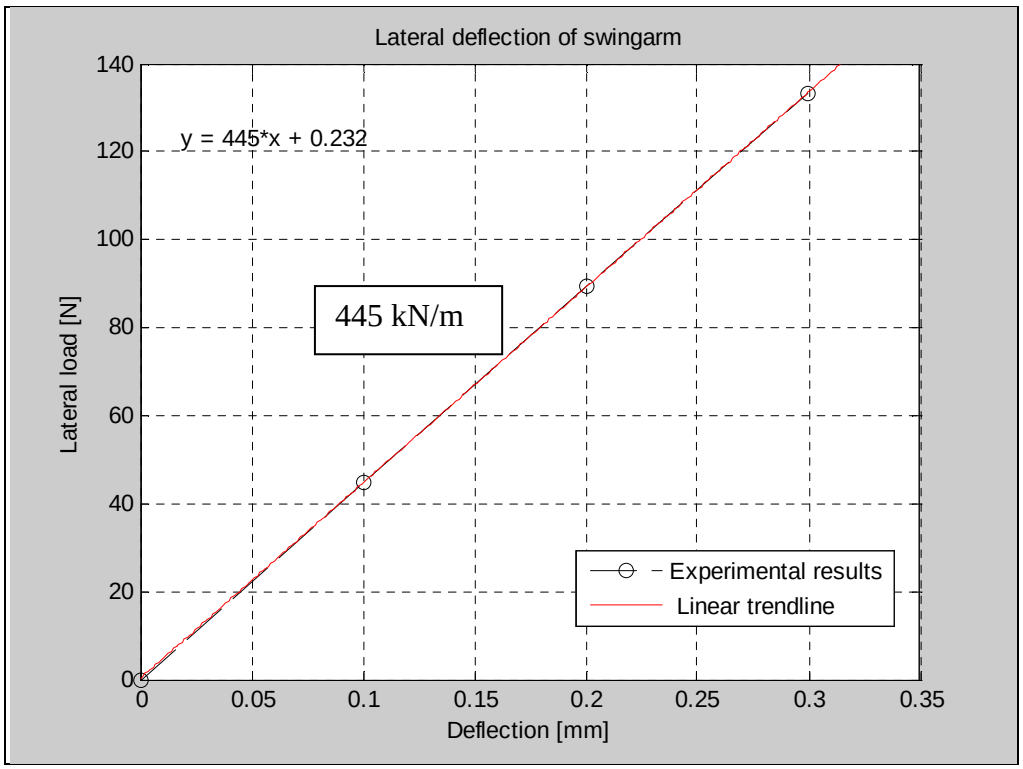


Figure 56. Lateral deflection of the swingarm showing the lateral stiffness coefficient of 445 kN/m.

Comparing this result to those obtained by Armentani et al. [8] and typical values stated by Cossalter [10] (Table 6), it can be seen that the swingarm lateral stiffness of 445 kN/m is on the lower end of the spectrum. In a similar manner to the torsional rigidity, the lower lateral stiffness may cause the rider to experience a "heavier" ride due to the slower response time. The lower stiffness (compared with other values) may also reduce weave mode stability at medium to higher speeds. However as shown by Cossalter et al. [27], the lower lateral stiffness may increase the weave mode stability at high speeds.

Table 6. Comparison lateral stiffness values.

Designation	Torsional stiffness [kN/m]
Ducati Carbon Fibre	**445**
Kawasaki ZX10R (Armentani et al.)	603
Suzuki GSX R1000 (Armentani et al.)	804
Honda CBR 1000R (Armentani et al.)	965
Cossalter	800-1600

Although the results show the torsional and lateral stiffness values of the carbon fibre swingarm to be generally lower than other swingarm stiffness values, it is difficult to state whether the swingarm will certainly affect the cornering response time and weave mode stability as suggested. In comparing swingarms, a few points should be noted. First, the affect that swingarm stiffness has on weave mode was studied on a 150 cc scooter (Cossalter et al. [27]). The question to ask here is, can the results from a scooter be compared with that of a much larger racing motorcycle? Second, which follows on from the first, is it appropriate to directly compare swingarm stiffness values of different motorcycles with one another? Each motorcycle consists of a number of different components such as wheels, frame and suspensions, each with a certain mass, stiffness and damping. Each motorcycle potentially has a different overall dynamic system. A direct comparison of stiffness values may not provide the overall picture of how the swingarm affects the system as a whole.

The discussion suggests that it is better to compare swingarms that have motorcycles with similar overall dynamic systems. To determine the actual effect that the carbon

fibre swingarm stiffness would have on the motorcycle would require firstly a comparison with the stiffness values of a standard aluminium Ducati 1098 swingarm. Furthermore, it is recommended to carry out experimental acceleration and strain measurements on both the original aluminium swingarm and the carbon fibre swingarm while the motorcycle is being operated through typical driving conditions at increasing speeds. Only then could more conclusive statements be made regarding the effect that the swingarm has on the motorcycle. This study however, has successfully characterized the stiffness of the carbon fibre swingarm.

5.2 Strain Analysis

The results and discussions of strain measurements on the swingarm are presented next.

5.2.1 Strain Gauge Validation

Before the strain gauges were mounted on the swingarm and measurements were made, an axial strain gauge was mounted on a cantilever rectangular plate and loads were applied. The strain was measured and compared with the FEA carried out on the plate (Appendix A). The aim of this exercise was to validate the strain measurements with classical laminate theory used in the FEA. Differences of less than 2% were found between the FEA and strain gauge readings showing that the measured values corresponds well with the results obtained using FEA.

5.2.2 Strain Gauge Transverse Sensitivity

Strain gauge transverse sensitivity was discussed in Section 2.4 where equations were presented that calculate the actual strain along a gauge axis based on the strain measured axially and perpendicular to gauge axis. These equations were applied to the measured strain in the 0° and 90° axes where the x-direction corresponds to 0° and the y-direction corresponds to 90°. Table 7 shows the measured strains ε_{mx} and ε_{my} at the maximum vertical load of 8000 N. Furthermore, only Positions 3 through 6 were taken into account because the data acquisition system only captured both the x- and y-direction strains needed to calculate the error due to transverse sensitivity at Gauges 3-6. Tables 8 and 9 show the actual strain (ε_x and ε_y) using transverse sensitivity

factors of K_t = +5% (0.05) and -5% (-0.05) respectively. The Poisson's ratio υ_0 for steel was taken as 0.285 [39].

Table 7. Measured strain in the longitudinal and transverse directions at maximum load of 8000 N at Positions 3-6.

Position	ε_{mx} [$\mu\varepsilon$]	ε_{my} [$\mu\varepsilon$]
3	-592	831
4	-1090	660
5	1050	-884
6	725	-394

Table 8. Strain correction at Positions 3-6 using K_t = +5% (0.05).

Position	ε_x [$\mu\varepsilon$]	% error x-direction	ε_y [$\mu\varepsilon$]	% error y-direction
3	-625	-5.5	848	-2
4	-1109	-1.7	702	-6.4
5	1077	-2.6	-923	-4.4
6	734	-1.2	-424	-7.6

Table 9. Strain correction at Positions 3-6 using K_t = -5% (-0.05).

Position	ε_x [$\mu\varepsilon$]	% error x-direction	ε_y [$\mu\varepsilon$]	% error y-direction
3	-558	5.7	813	2.1
4	-1072	1.7	614	6.9
5	1020	2.9	-843	4.6
6	715	1.4	-363	7.9

The maximum error due to transverse gauge sensitivity was approximately -7.6% and +7.9% for Strain Gauge 6 in the y-direction. Based on these results, it was assumed that the errors were small enough to ignore when presenting the experimental results in this section. It should be noted that the aim in this section was to obtain an indication of the type and magnitude of the strains and therefore errors of less than 8% were considered small enough to ignore. However, when comparing experimental

and FE results in Section 5.3.2, the errors due to transverse sensitivity *were* taken into account when attempting to minimize the error between the FE and experimental results. The following section presents the strain results as measured.

5.2.3 Strain Measurements

For the sake of clarity, the strain gauge measurement positions on the swingarm are presented again in Figures 57 and 58. The lower arm refers to the part of the swingarm that contains Positions 2 and 3; the top arm refers to the region where Positions 4, 5 and 6 are situated; Position 1 is on the wheel mount and Positions 7 and 8 are on the pivot points.

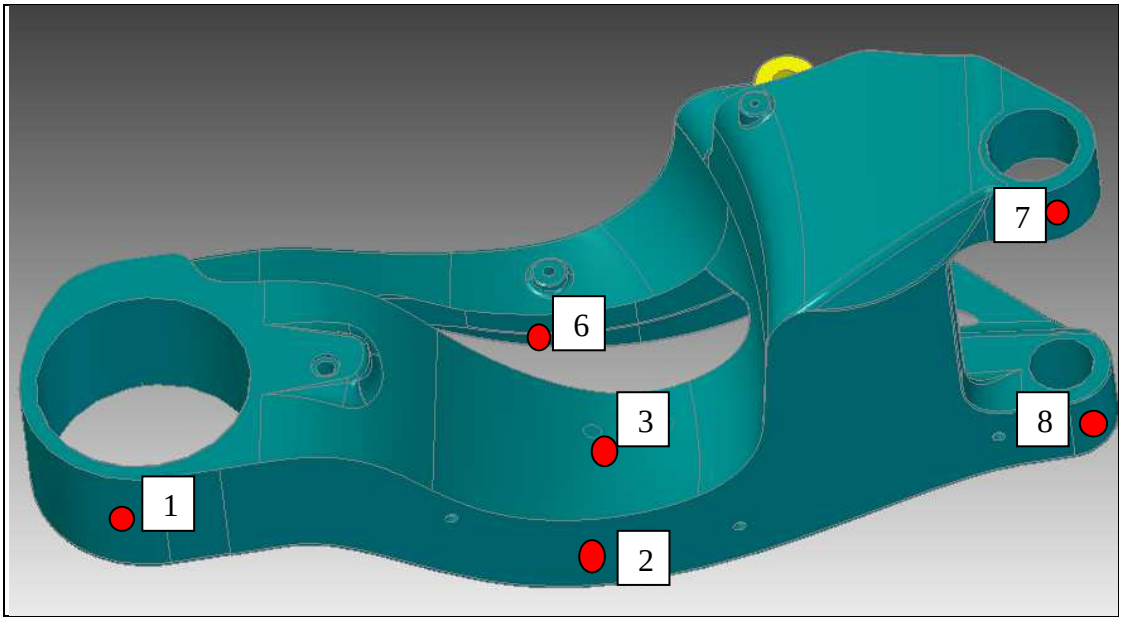


Figure 57. Strain Gauge measurement positions

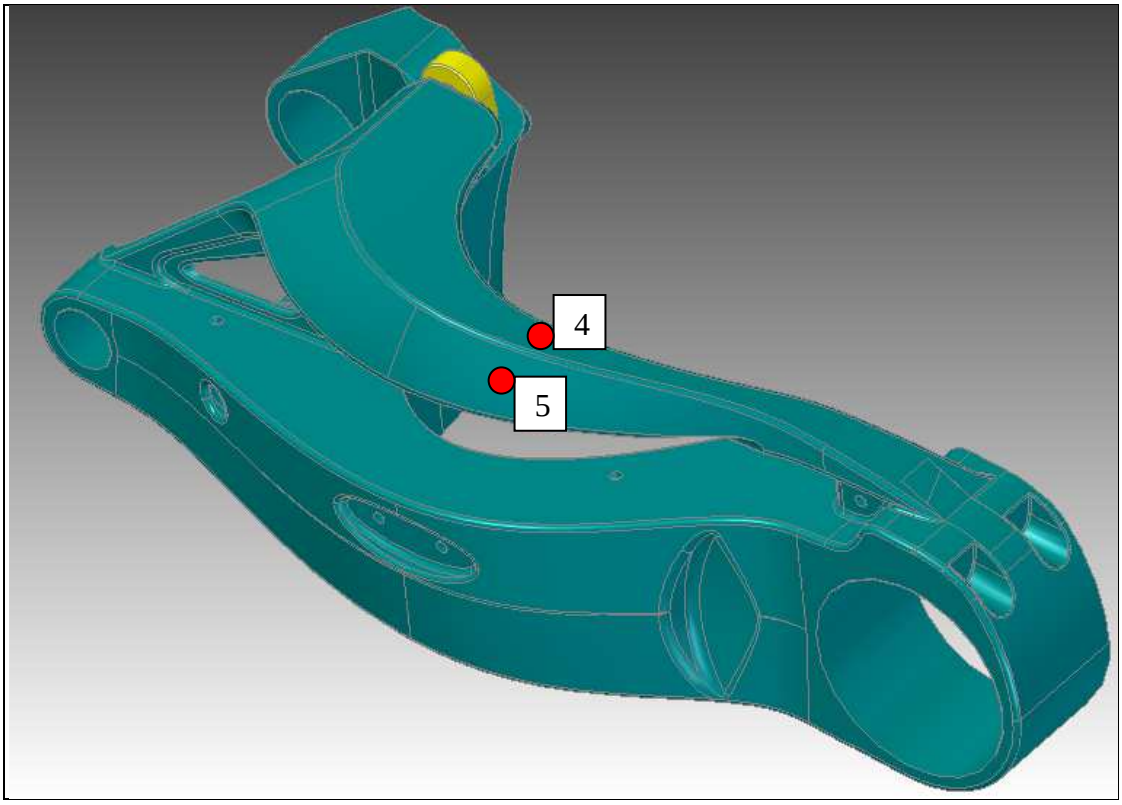


Figure 58. Strain gauge measurement positions.

Before proceeding, it should be noted that during the vertical loading tests, two channels measuring the longitudinal strain in Gauges 1 and 2 did not function. Therefore out of the possible eight longitudinal strain measurements, only six were measured.

Figure 59 presents the longitudinal strain measurements at Positions 3 through 8 during the vertical loading. The strain on the top arm at Positions 4, 5 and 6 measured the highest strains. At the maximum load of 8000 N, Gauges 4 and 5 measured approximately 1100 με (compressive) and 1100 με (tensile) respectively and Gauge 6 measured approximately 750 με (tensile). Therefore based on the positions measured, when designing the swingarm, it is important to know that the highest longitudinal strains in both tension and compression occur on the top arm during vertical loading.

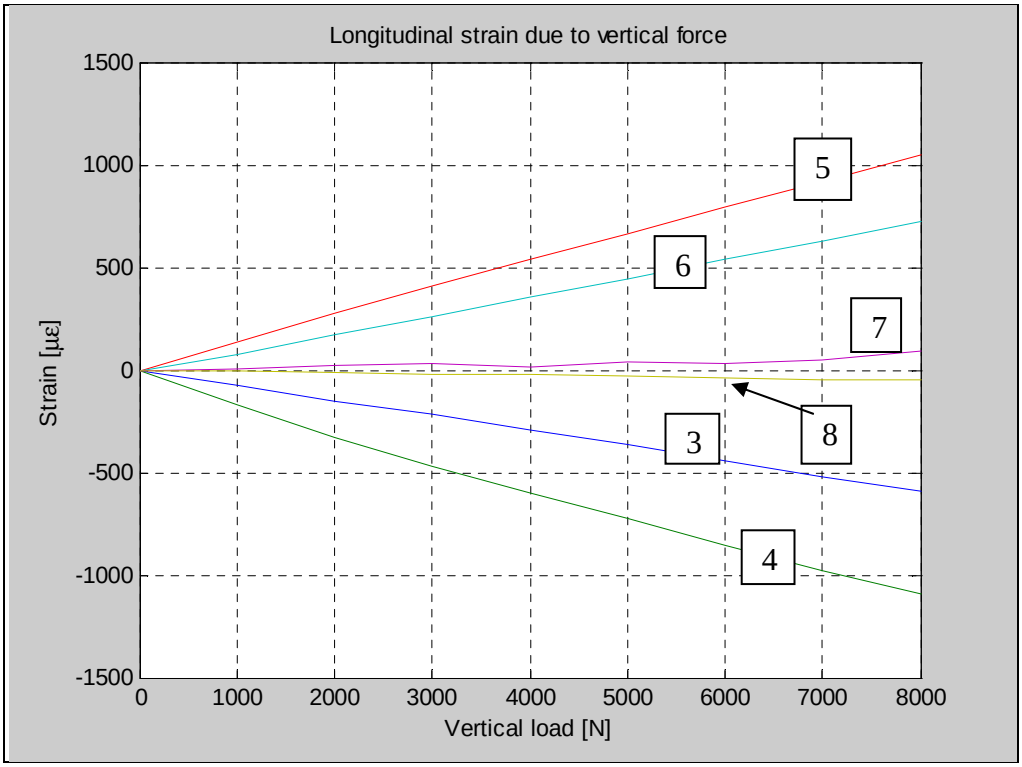


Figure 59. Longitudinal strain measured at positions 3 through 8.

Normal strain due to bending in a beam is given by the equation $\varepsilon = My/EI$ where M is the bending moment acting at the measurement point, y is the distance from the neutral axis, E is the modulus of elasticity and I is the second moment of area. It is difficult to discuss the strain results with respect to the distance from the neutral axis because it is uncertain where the neutral axis of the swingarm lies. However, the higher strain on the top arm may be due to a lower second moment of area in the top arm compared with that in the bottom arm. Also, the lowest strains occur at the pivot point at Positions 7 and 8. This is due to the aluminium inserts being mounted at those positions which increase the rigidity of those positions substantially.

The transverse strain due to vertical loading is shown in Figure 60. Positions 3 and 4 experience the highest tensile strains of approximately 800 με and 650 με respectively and Position 5 experiences the highest compressive strain of approximately 900 με. Typical ultimate strain values for a woven carbon fibre ply are approximately 8000 με for both the axial and transverse directions. For a unidirectional ply the ultimate strain is approximately 10000 με and 5000 με for the axial and transverse directions respectively. The measured strains were considerably lower than the maximum allowable strains which indicates the laminate design is strong enough to handle the

vertical loading. Furthermore, the ultimate strains are typical values for single plies. In the case of the swingarm, the laminates consist of a number of plies bonded together which increases the strength. It is also important to know that during vertical loading that causes bending in the swingarm, longitudinal as well as transverse strains occur on the swingarm. This is due to the nature of the layup design.

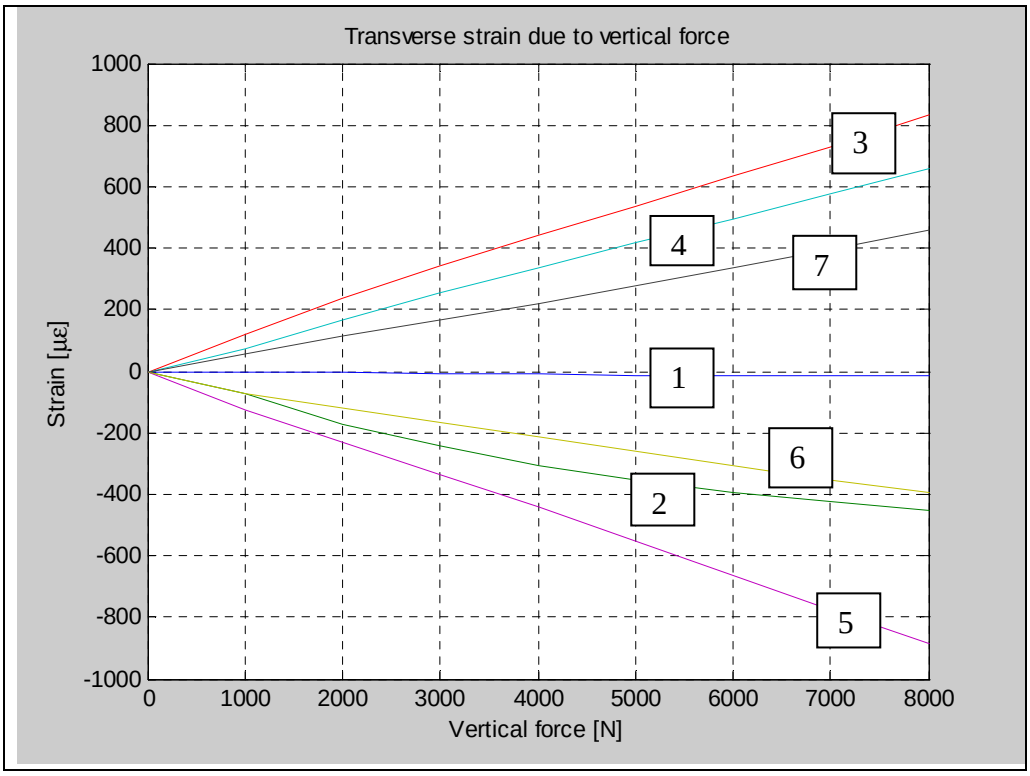


Figure 60. Transverse strain measured at positions 1 through 7.

Figures 61 to 63 show the magnitude and direction of strain (due to vertical loading) occurring at the positions on the bottom and top arms. The reason only the bottom and top arms were looked at was to determine how the loading affects the middle part of the swingarm. In the figures, the arrows pointing away from each other specify tensile strain and the arrows pointing toward each other specify compressive strain along that direction.

Position 3 experiences compression in the gauge longitudinal direction and tension in the transverse direction.

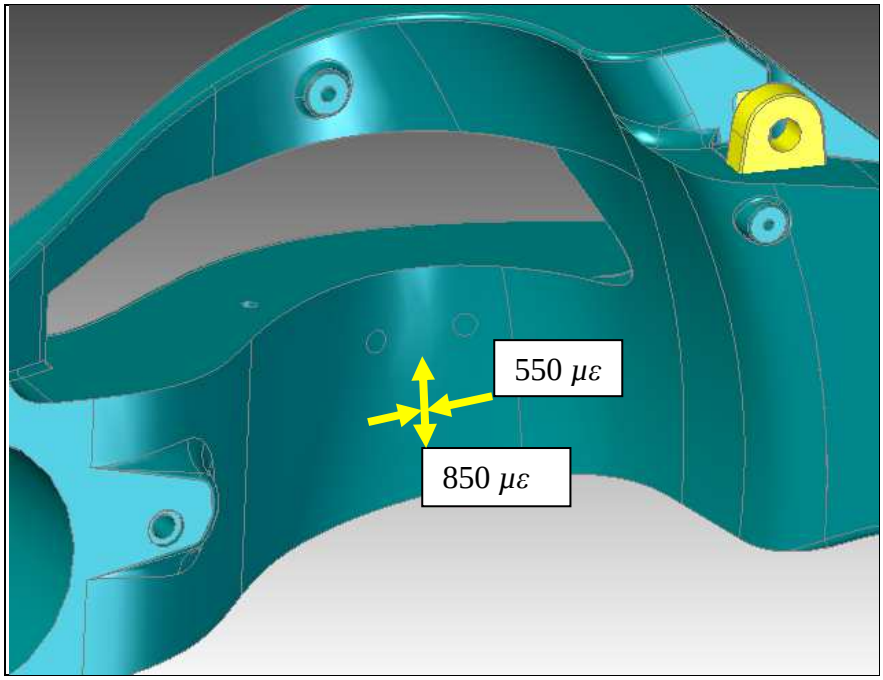


Figure 61. Maximum longitudinal and transverse strain at Position 3 during vertical loading.

During vertical loading the bottom (Position 6) and the side (Position 5) of the top arm experienced tension in the longitudinal direction and the top of the arm (Position 4) experienced compression in the longitudinal direction.

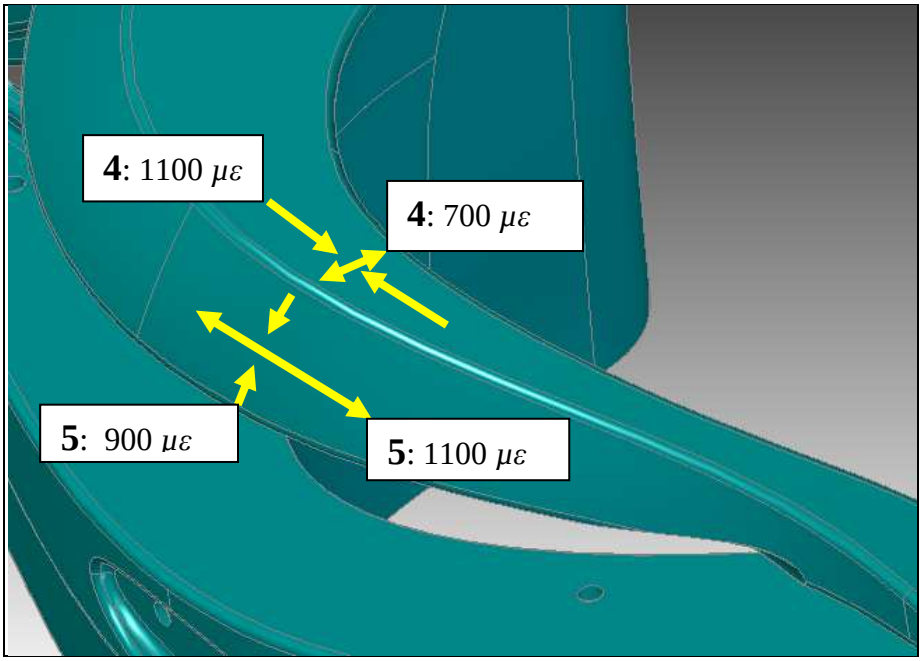


Figure 62. Maximum longitudinal and transverse strain at Positions 4 and 5 during vertical loading.

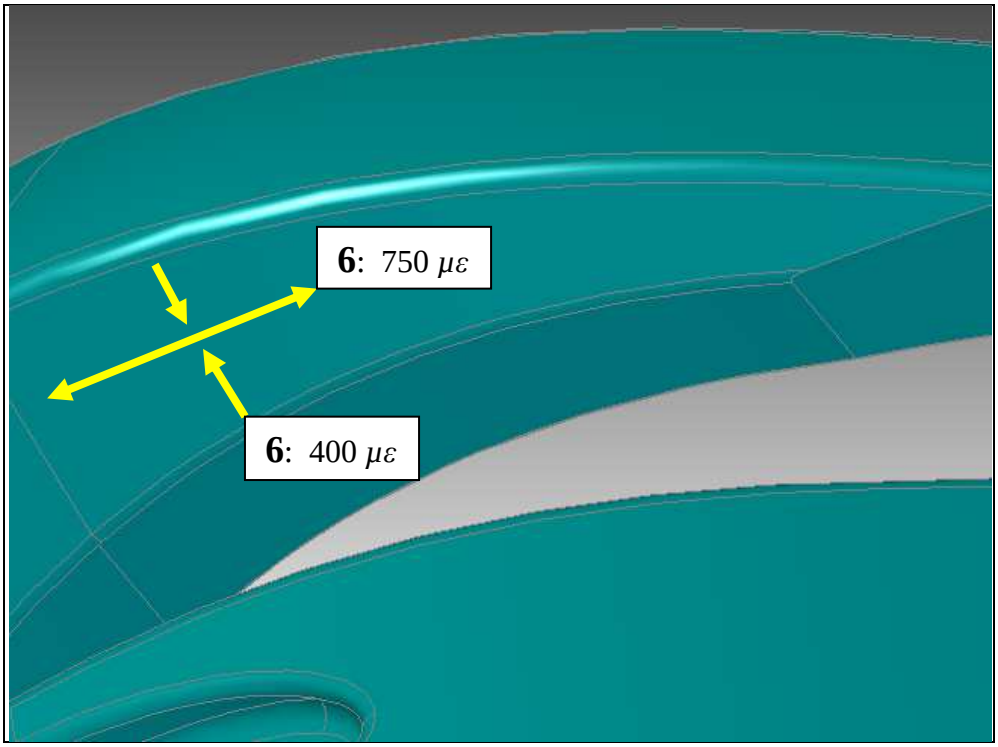


Figure 63. Maximum longitudinal and transverse strain occurring at Positions 6 during vertical loading.

The fact that the top part of the arm is in compression and the bottom part is in tension in the longitudinal direction is expected. The top arm can be considered to be a beam with a bending moment applied to it which causes the compression at the top and the tension at the bottom. The side of the top arm, Position 5, also experiences tension in the longitudinal direction. This may indicate, due to the asymmetric design of the swingarm and the shape of the top arm that as the swingarm is loaded vertically upward, a slight rotation about the longitudinal axis also develops as shown in Figure 64. This may also be the reason why in the transverse direction, there is a stretch on top and compression on the side and bottom of the top arm. This suggests that coupling exists between vertical and torsional direction. That is, as a load is applied in the vertical direction, not only are vertical deflections seen but also torsional deflections.

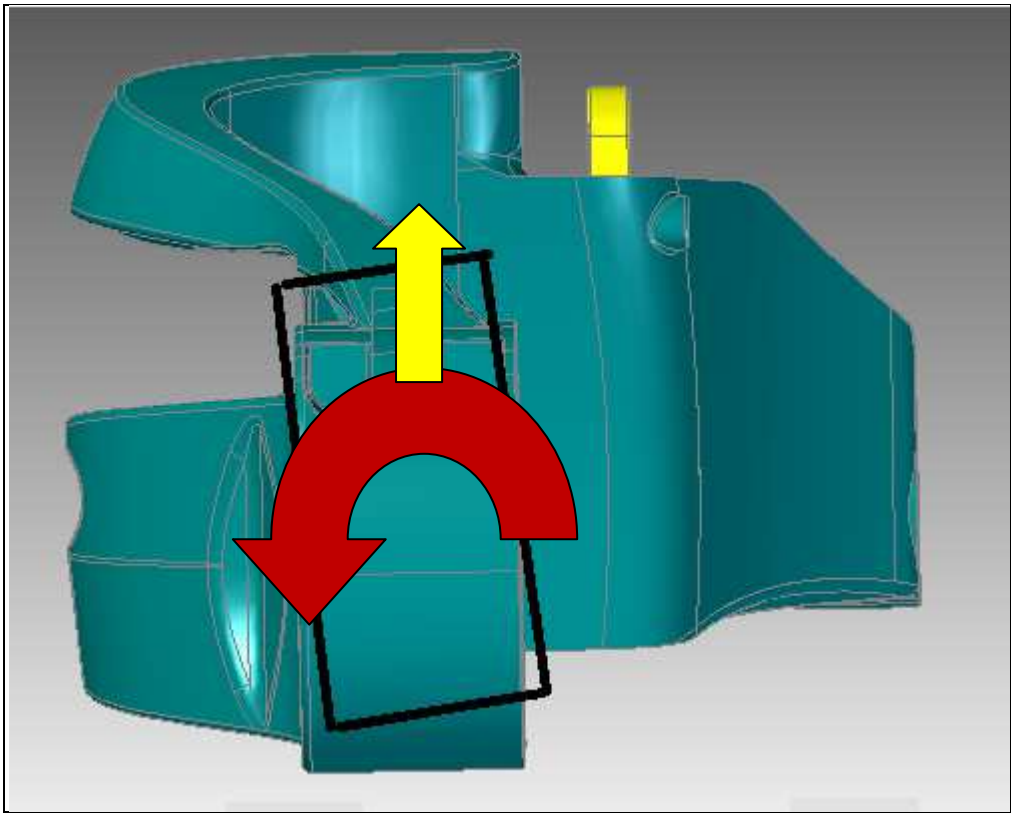


Figure 64. Schematic of the vertical and rotational translation of the swingarm during vertical loading.

To establish the relationship between the strains on the top arm as the vertical load is increased, the strains were normalized (Figure 65) based on the maximum strain of 1100 με. The numbers on each column refer to the gauge position, and the letters L and T refer to longitudinal and transverse directions respectively.

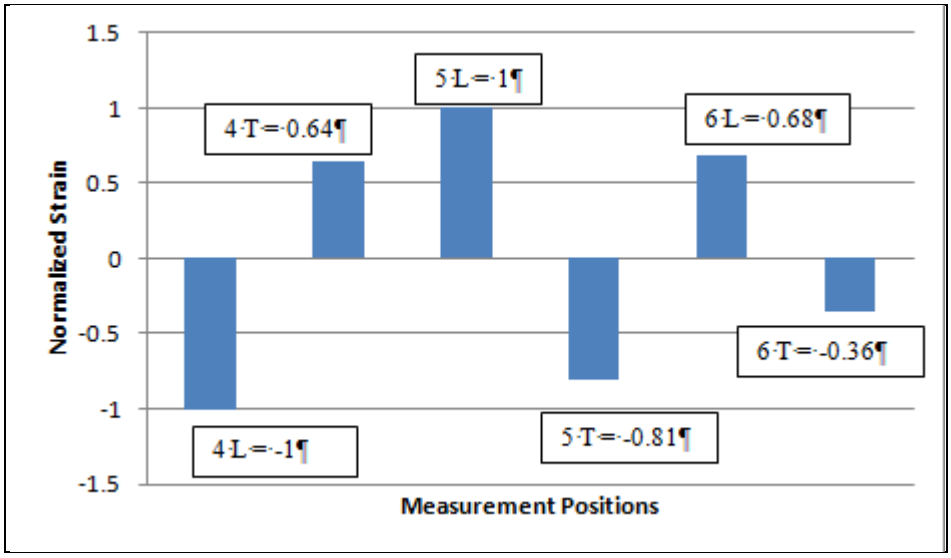


Figure 65. Normalized strain on the top arm of the swingarm due to vertical loading.

As the vertical load is applied, Positions 4 and 5 experience the same magnitude of longitudinal strain but with Position 4 in compression and 5 in tension. The longitudinal strain at Position 6 is approximately 0.7 time as large as the maximum strain. Therefore the areas which will govern the design are Positions 4 and 5 in the longitudinal direction and Position 5 in the transverse direction. If a linear strain is assumed, then these positions will experience failure first under vertical loading conditions.

Figures 66 and 67 present the longitudinal and transverse strain occurring during torsional loading. During the testing, the data acquisition system did not capture Strain Gauge 2 in its longitudinal direction and Strain Gauge 8 in its transverse direction. Also, it appeared that the data from Strain Gauge 7 in its transverse direction did not present proper results and was therefore not included.

At the maximum torsional loading of 680 Nm, Position 6 experienced the highest longitudinal strain of approximately 380 με. The longitudinal strain was highest on the top and underside of the top arm (Positions 4 and 6). In terms of the positions away from the aluminium inserts, Positions 4, 5 and 6 experience tension and Position 3 experiences compression in the longitudinal direction.

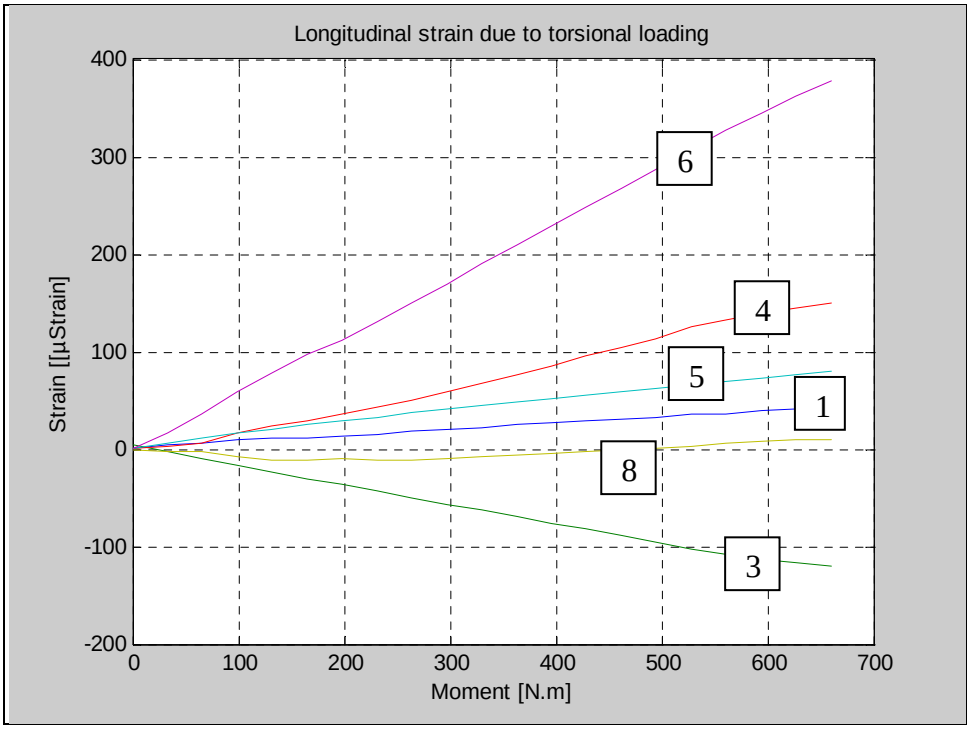


Figure 66. Longitudinal strain due to the torsional loading. Strain gauge positions are shown on the figure.

The highest transverse strain due to torsional loading, was measured at Positions 5 and 6 of approximately 250 με (compression). Positions 3, 4, 5 and 6 all experience compression in their respective transverse directions during torsional loading.

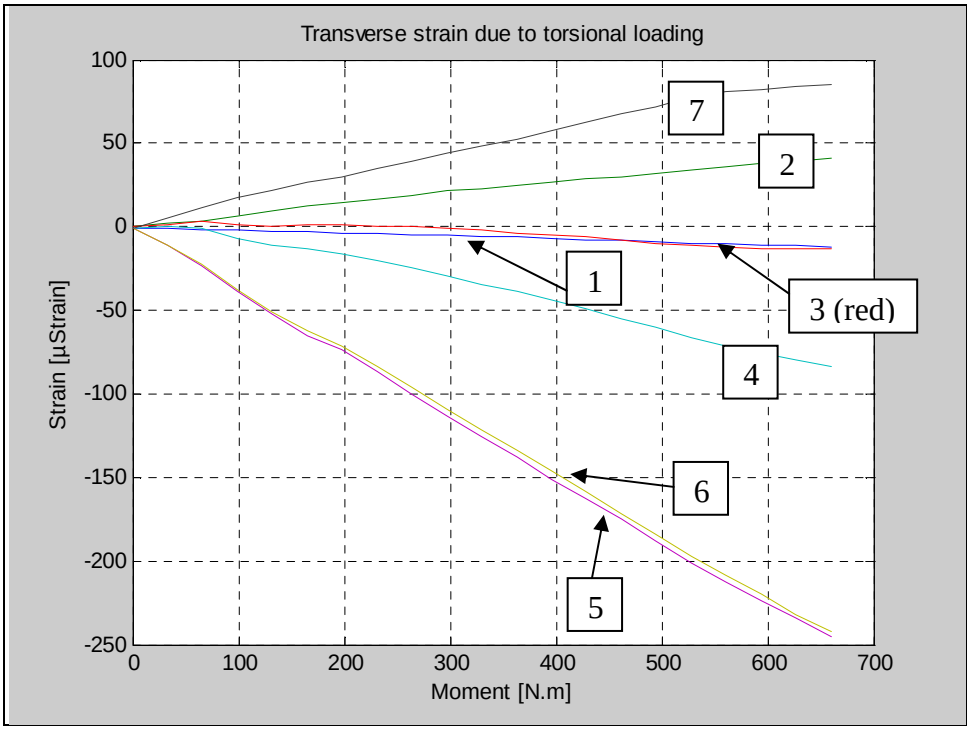


Figure 67. Strain in the transverse direction due to torsional loading.

Figures 68 to 70 present graphically the strains occurring at the positions in the central part of the swingarm.

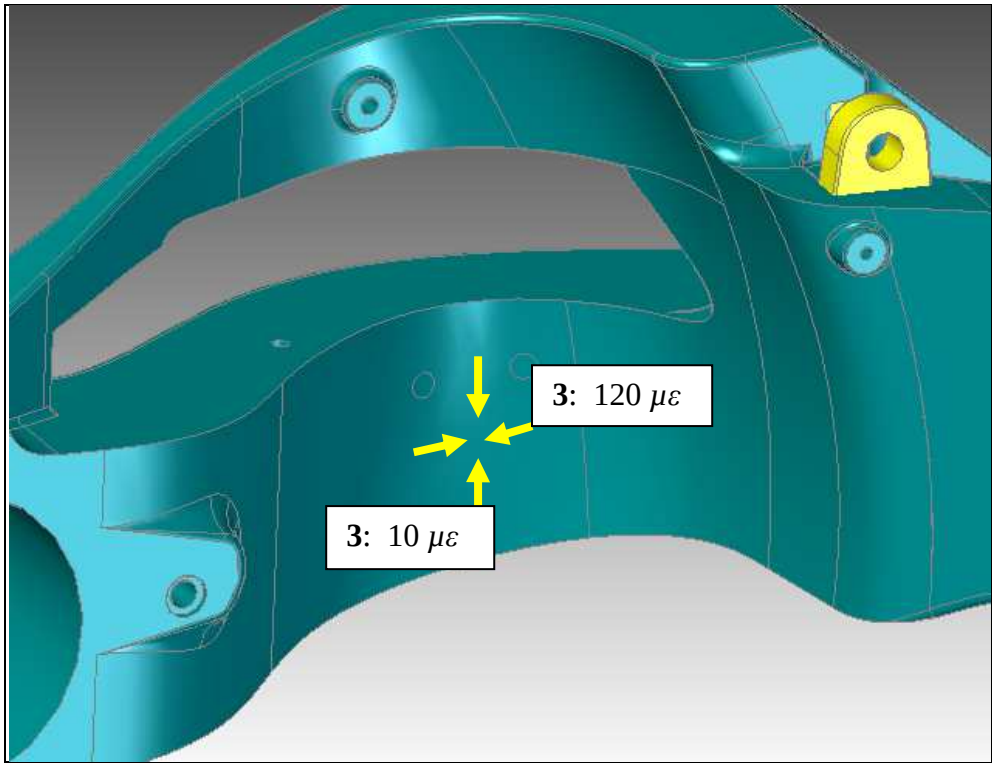


Figure 68. Maximum longitudinal and transverse strain at Position 3 during torsional loading.

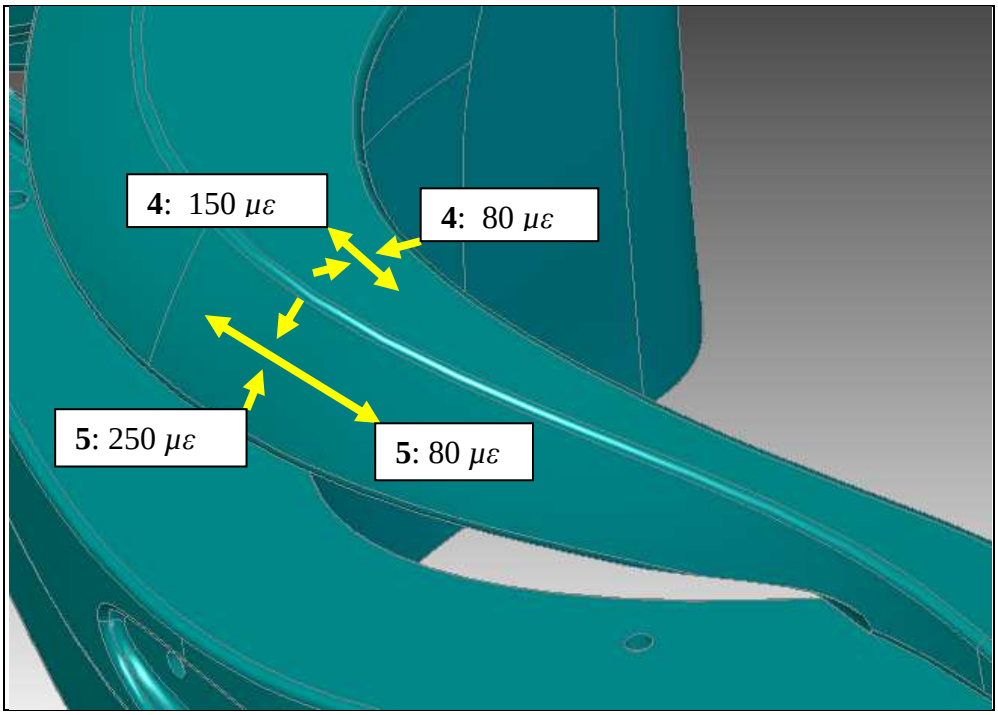


Figure 69. Maximum longitudinal and transverse strain at Positions 4 and 5 during torsional loading.

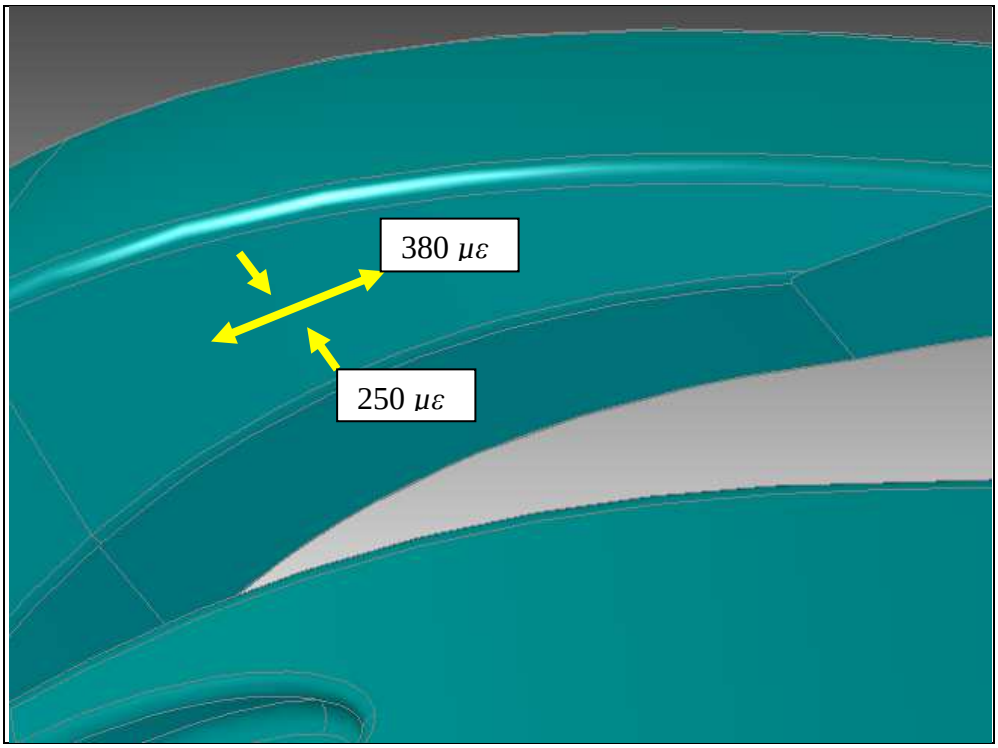


Figure 70. Maximum longitudinal and transverse strain at Position 6 during torsional loading.

As the moment is applied, the three sides of the top arm all experience tension in the longitudinal direction with the largest tension occurring on the underside (Position 6). It was expected that the top of the arm (Position 4) would experience compression due to bending[6] but it appears that the combination of torsion and bending results in longitudinal tension and transversal compression on all three sides.

If the results on the top arm are normalized (Figure 71), a relationship can be developed between the results. The results suggest that during torsional loading, the underside of the top arm (Position 6) is the limiting position in that the underside will most likely fail first in both directions.

[6] The reader should remember that during torsional loading a resultant force also occurs at the wheel mount due to the applied force not being a couple. A resultant force therefore also acts in the swingarm vertical direction.

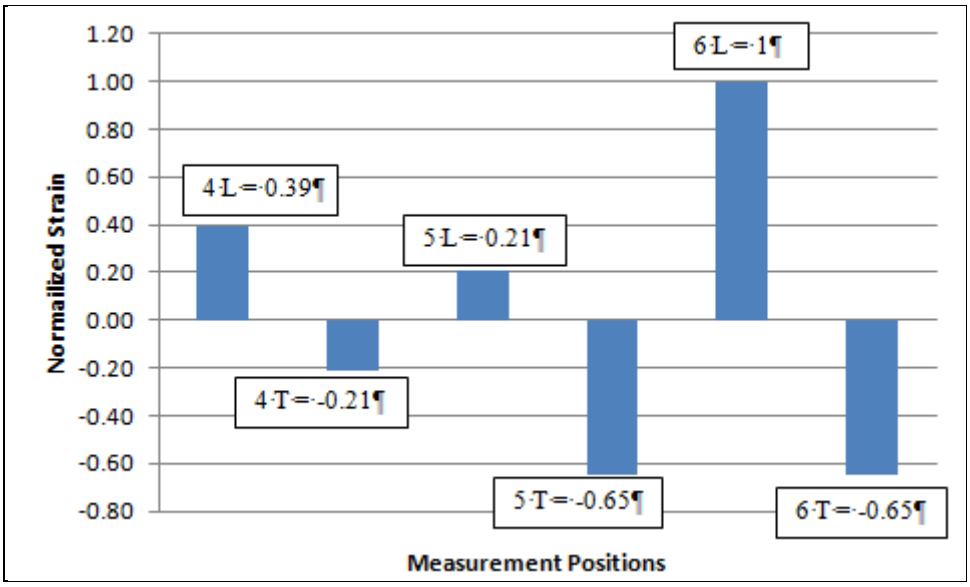


Figure 71. Normalized strain occurring on the top arm of the swingarm due to torsional loading.

5.3 Finite Element Analysis

This section presents the results obtained from the FEA. The assumptions for modelling the FE model are briefly presented again:

- Only the layup at the major zones were modelled with the smaller zones included in the larger more significant zones.
- Ply overlap was not modelled due to the complexity of the swingarm design.
- The aluminium inserts were not modelled.

Therefore when viewing the results, the reader should keep in mind the assumptions that were made to model the highly complex swingarm.

5.3.1 Finite Element Analysis: Deflections

The deflections of the swingarm were compared with the experimental results. Figure 72 shows the vertical deflection of the swingarm due to the maximum 8000 N vertical load.

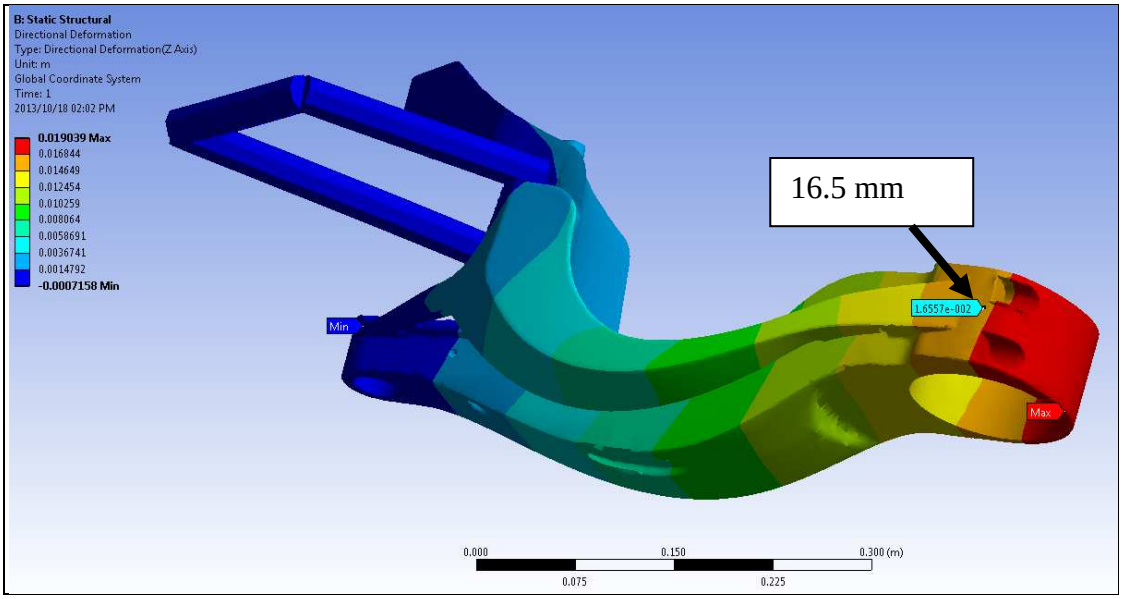


Figure 72. Vertical deflection at 8000N.

Table 10 compares the vertical deflection calculated by the FE model and the deflection measured during experimental testing. A 4.4% difference[7] between results was calculated which is acceptable.

Table 10. Comparison between experimental and FEA vertical deflection at the wheel mount.

Experimental deflection [mm]	FEA deflection [mm]	% Difference
15.8	16.5	4.4

Figure 73 shows the deflection calculated by the FE model during torsional loading at maximum load and moment of 2000 N and 680 Nm respectively. In a similar way to that shown in Section 4.3, the rotational angle was calculated by obtaining the net displacement and dividing it by the radius. Therefore as shown in Figure 73, the deflections at either side of the wheel mount were obtained and the difference between them was calculated (4 mm – 2.8 mm = 1.2 mm). This refers to the net displacement at the top of the wheel mount which was divided by the distance between the two measurements points (80 mm) to obtain the rotational angle: 1.2 mm / 80 mm = 0.015 rad or 0.86 deg.

[7] The percentage difference values calculated in this document made use of the experimental results as the reference values. For example, ((16.5 – 15.8)/15.8)x100 = 4.4 %.

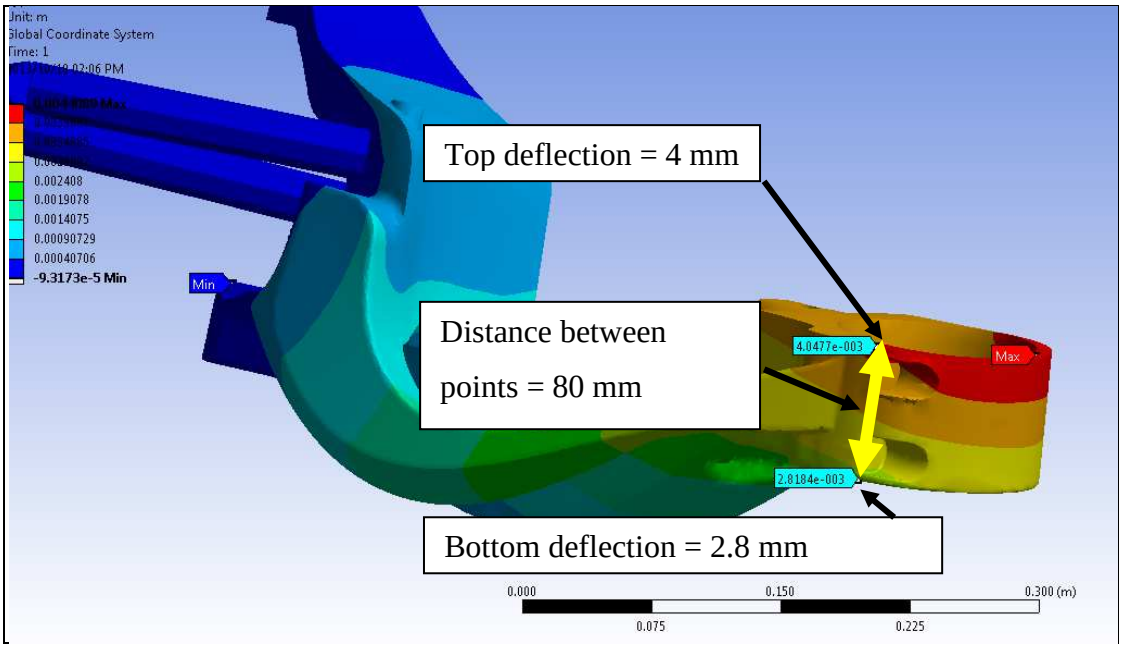


Figure 73. Deflection measured during maximum torsional loading of 2000 N and 680 Nm.

The maximum angle measured during experimental testing was approximately 1.2 deg. A comparison between the experimental and FEA angles of rotation is presented in Table 11 which gave a difference of 28%.

Table 11. Comparison between experimental and FEA rotation at the wheel mount.

Experimental rotation [deg]	FEA rotation [deg]	% Difference
1.2	0.86	28

The FEA lateral deflection was calculated as approximately 0.15 mm at the maximum lateral load of 135 N as shown in Figure 74. The deflection measured during experimental loading was 0.3 mm, twice as large as that calculated by the FEA. A difference of 50% was calculated between FEA and experimental lateral deflection (Table 12).

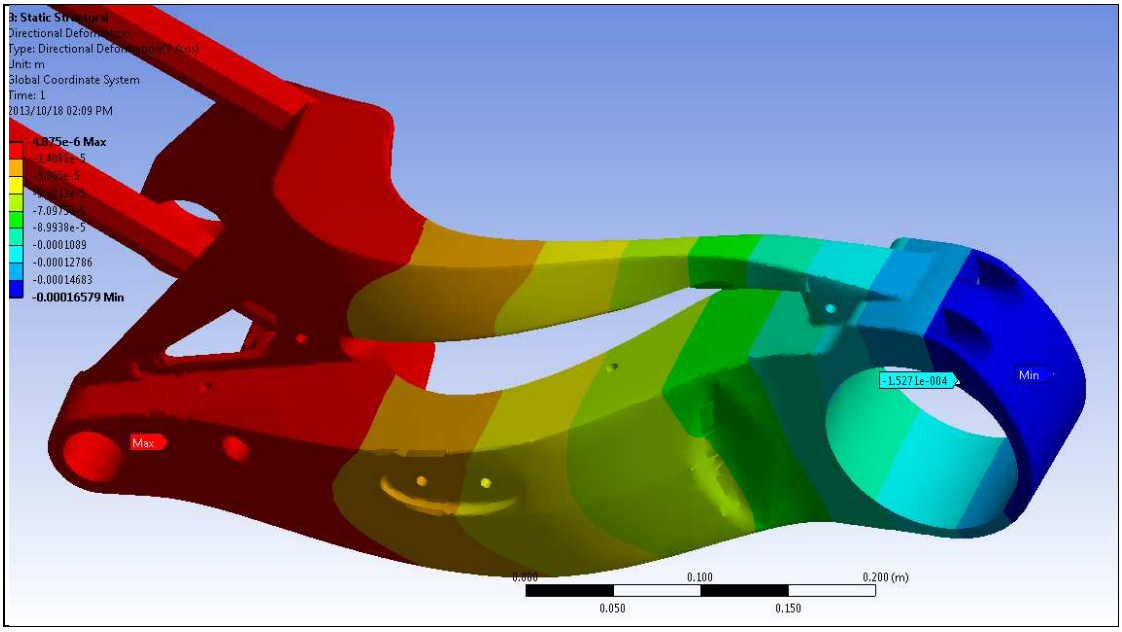


Figure 74. Lateral deflection under the 135 N load.

Table 12. Comparison between experimental and FEA lateral deflections at the wheel mount.

Experimental rotation [mm]	FEA rotation [mm]	% Difference
0.3	0.15	50

An initial reason for the large difference could be due to very low deflections (0.3 mm) in the lateral direction. At low deflections large differences occur in relative terms because the errors due to lash and bedding have a more significant effect. At larger loads and deflections a higher degree of correlation will result. For future testing, more accurate results may be obtained if much larger loads are applied in the lateral direction.

5.3.2 Finite Element Analysis: Strains

The strains calculated by the FE model were also compared with the measured strains. It should be noted that only the strains situated away from the aluminium inserts were analyzed. Due to not accurately modelling the region at the aluminium inserts, the results obtained by the FEA at those positions were not trusted and were therefore ignored. Only Positions 2 to 6 were analyzed and compared with experimental values. Furthermore, as was seen in Section 5.2, the data acquisition system did not

record proper results for Gauge 2 in the longitudinal direction and therefore only the results from Gauge 2 in its transverse direction were compared with the FE results.

All the following results shown in the FEA figures are based on the maximum vertical load of 8000 N. Due to the linearity of the FE model, at zero load there is zero strain and at the maximum load of 8000 N the swingarm experiences the maximum magnitude of strain.

The underside of the swingarm, which includes Position 2, is shown in Figure 75. The transverse strain calculated by the FEA at this point was approximately -230 με. The measured strain at the same load was -450 με and a comparison between experimental and simulated strain over the entire 0 N - 8000 N range is presented in Figure 76.

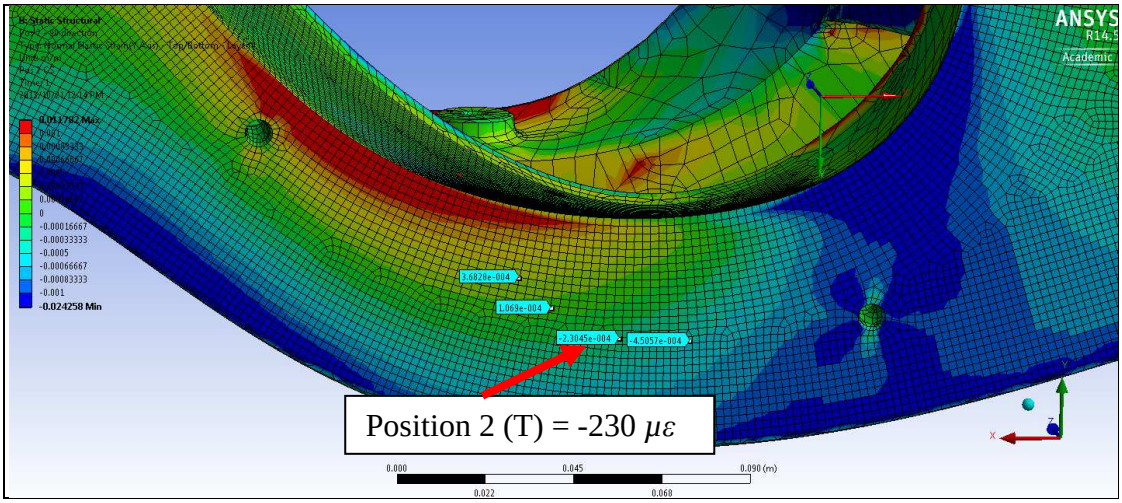


Figure 75. Strain distribution for Position 2 in the gauge transverse direction at vertical load of 8000 N.

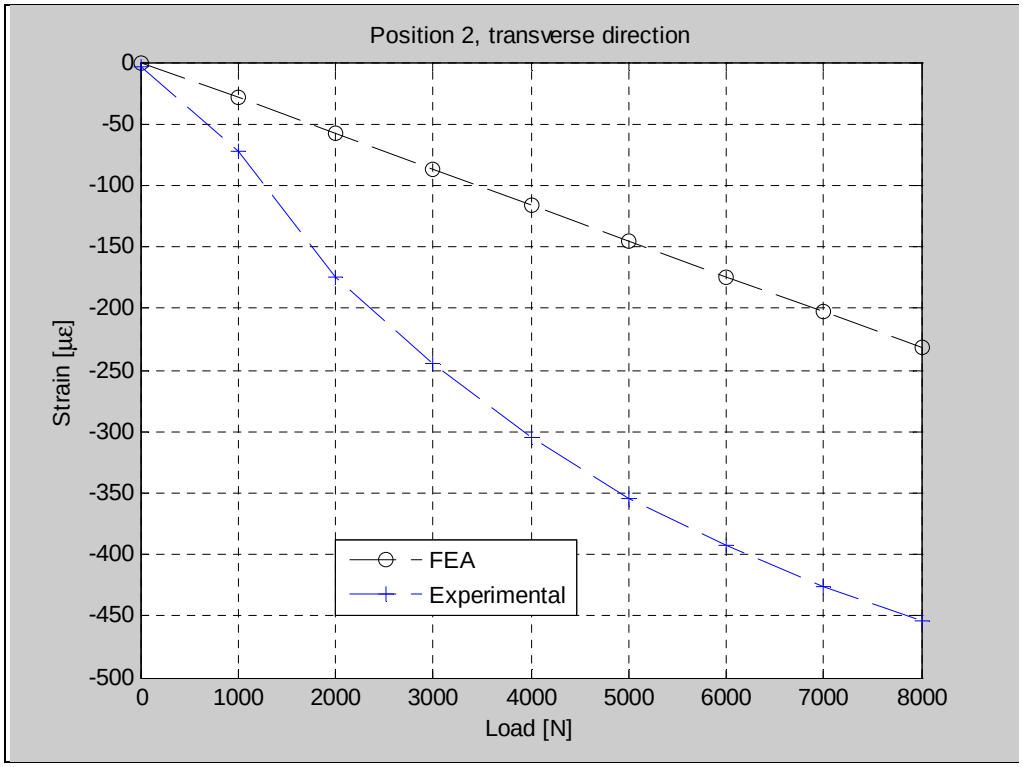


Figure 76. Comparison between FEA and experimental results at Position 2 in the gauge transverse direction.

Firstly, when comparing the FEA strain and experimental strain at 8000 N, a difference of 100 × (-450 - (-230)) / (-450) = 49% was calculated. This difference is large and to find possible reasons for the difference, **transverse sensitivity** and **gauge misalignment** were looked at first. The transverse sensitivity was based on strain measurements in the zero and ninety degree directions and due to the data acquisition system not measuring the longitudinal strain at Position 2 it was not possible to calculate the transverse sensitivity at this point. But assuming a transverse sensitivity error for Gauge 2 of -7.6 % (based on the largest negative error of -7.6% found at Gauge 6 in Table 8), then the measured transverse strain at Gauge 2 reduces to approximately -416 με. This reduces the difference between FE and experimental results to approximately 45%. In terms of gauge misalignment, Tuttle and Brinson [32] state that gauge alignment cannot be guaranteed to tolerances better than ±1 to 2 degrees. To determine the effect of gauge misalignment, the local coordinate axes in the FE model were rotated +2 degrees and -2 degrees to determine what effect it has on the FE results. Figures 77 and 78 show the results at Position 2 when rotating the axes -2 degrees and +2 degrees respectively. The strain at -2 degrees rotation is -205 με and at +2 degrees it is -280 με. Using the "best" results from the transverse

sensitivity (-416 με) and the gauge misalignment (-280 με), a difference of approximately 33% was calculated which shows a reduced difference.

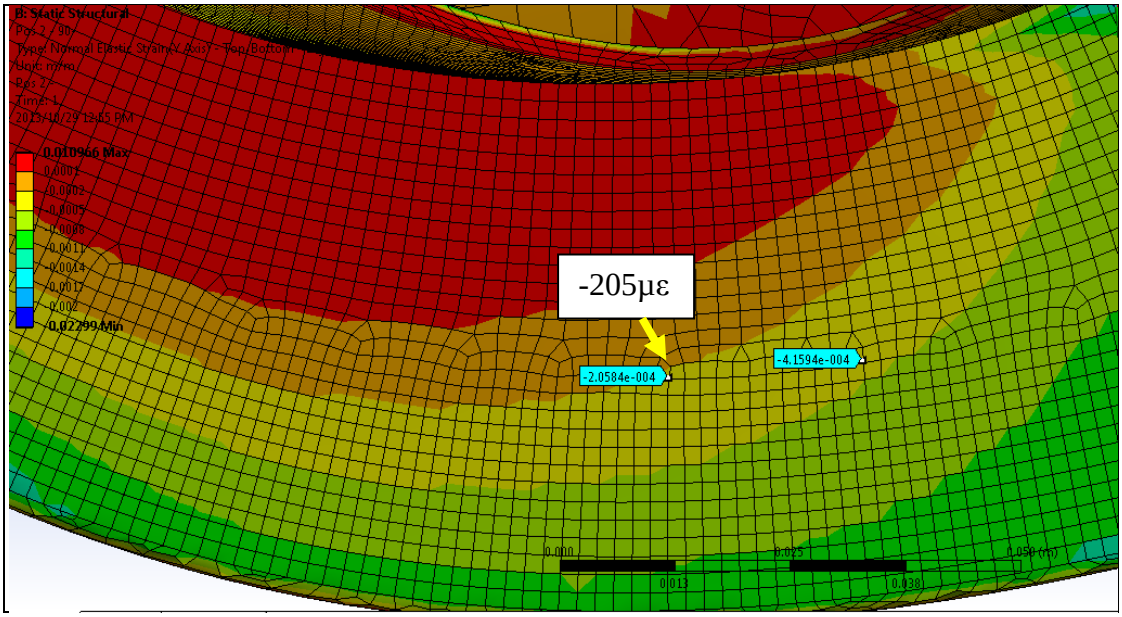


Figure 77. Position 2 in the transverse direction with the axes rotated -2 degrees.

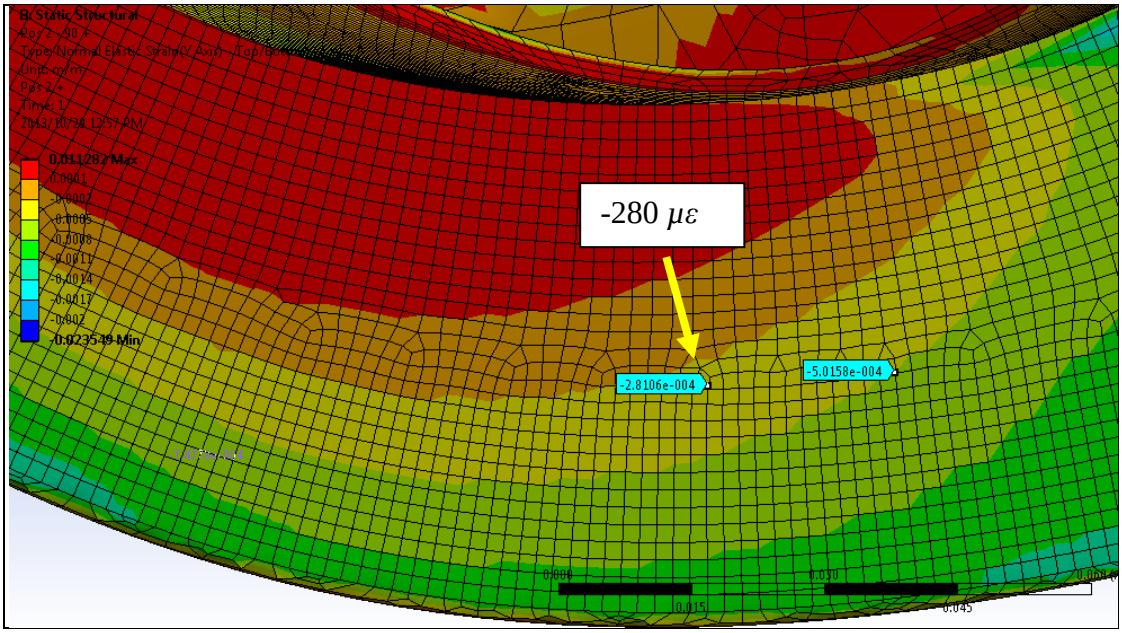


Figure 78. Position 2 in the transverse direction with the axes rotated +2 degrees.

Looking at further potential reasons for the large difference, Figure 79 shows that Position 2 in the transverse direction, is in the middle of a high strain gradient, i.e. the strain is changing rapidly in this area.

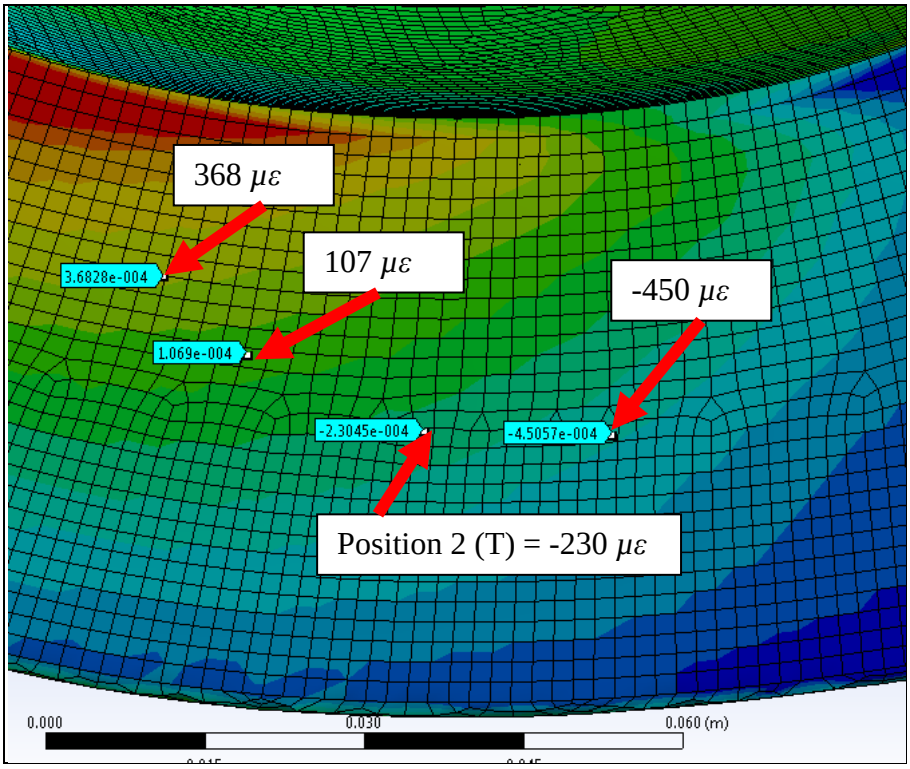


Figure 79. Close up of the strain distribution for Position 2 in the gauge transverse direction at vertical load of 8000 N

If the results on the FE model are viewed approximately 20 mm to the right, a value of -450 με is obtained. Also, moving approximately 10 mm and 20 mm to the top left, it can be seen that the strain on the FE model becomes 107 με and 368 με respectively. Therefore the position chosen to mount the 90° (transverse) strain gauge is near a region that changes from tensile to compressive strain and it is possible that the strain gauge readings in the transverse direction would not yield accurate results due to small changes resulting in high strain differences. Even though this is the case, simply by moving approximately 20 mm to the right on the FE model, strains very near to the measured values were found. Therefore based on the above discussions, transverse sensitivity, gauge misalignment and a high strain field gradient may all plausibly explain in part the difference in the FEA and measured strains.

The strain field for Position 3 in the longitudinal direction (horizontal direction in the figure) at 8000 N is shown in Figures 80 and 81. At Position 3, a longitudinal strain of -43 με was found on the FE model. Once again it can be seen that Strain Gauge 3 in the longitudinal direction was placed in the region of a high strain gradient.

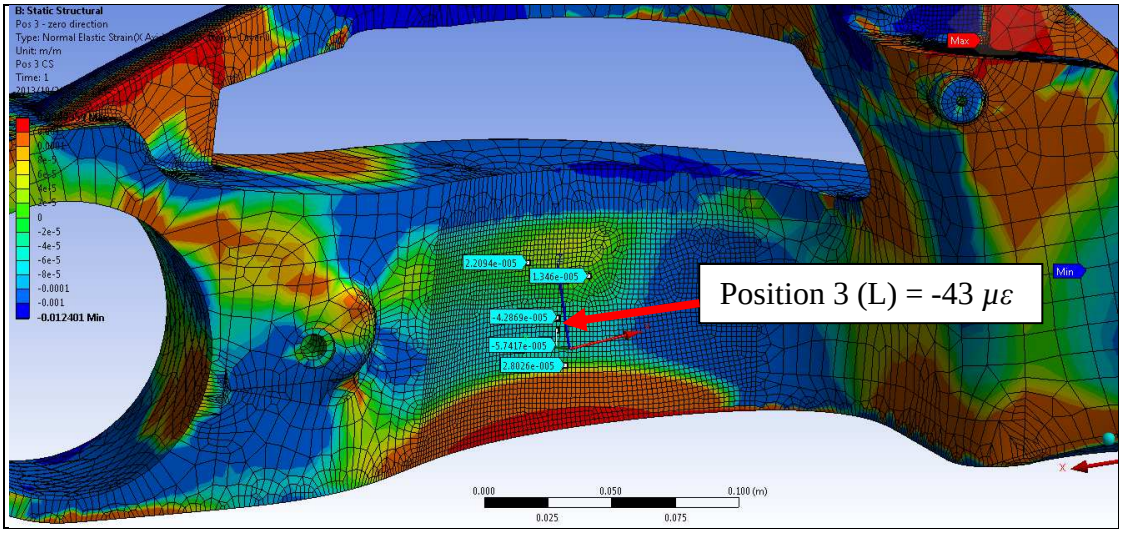


Figure 80. Strain distribution for Position 3 in the gauge longitudinal direction.

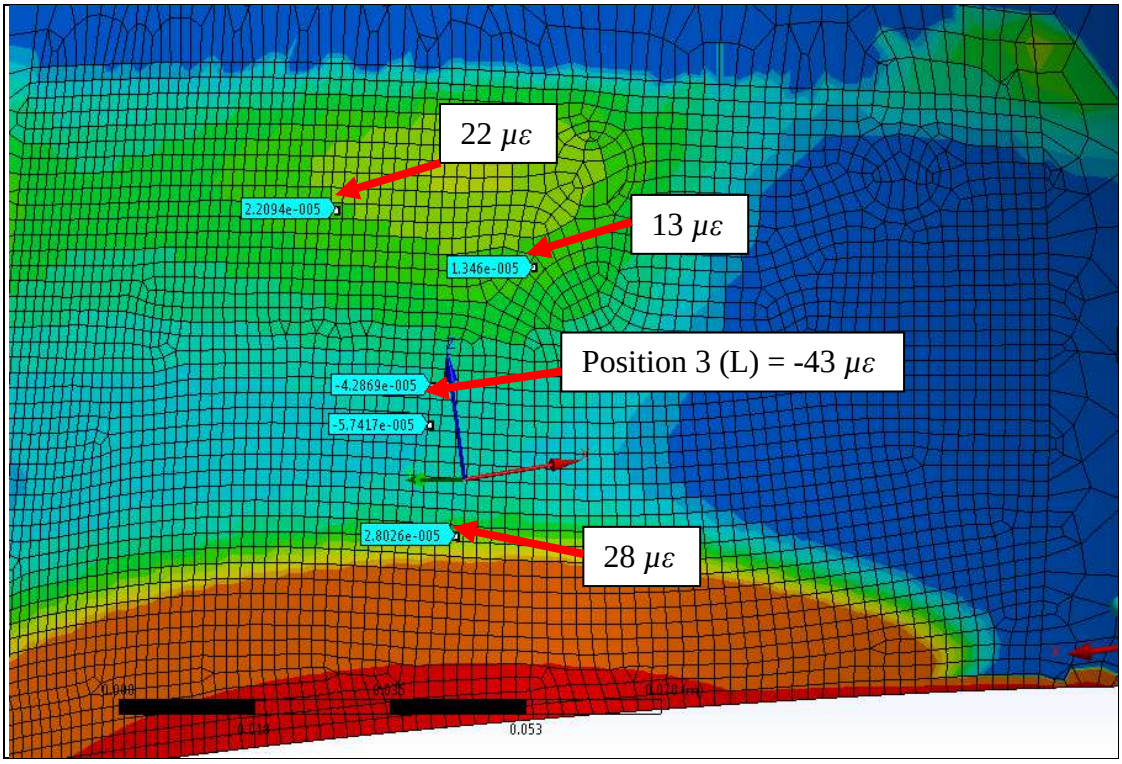


Figure 81. Close up of the strain distribution for Position 3 in the gauge longitudinal direction.

The comparison with the experimental results is shown in Figure 82. The experimental longitudinal strain measured at this position was -592 με and the difference was calculated as 100 × (-592 - (-43)) / (-592) = 93%. Once again, this difference is large and is likely due to the high strain gradient surrounding the measurement point. For example, studying Figure 81, it can be seen that moving

approximately 20 mm below Position 3, a positive strain of 28 με was found and moving similar distances above the measurement point, values in the region of 13 με to 22 με are found on the FE model. This means that both above and below the measurement point the strain changes rapidly from negative to positive. As discussed with Position 2, it is possible that a strain gauge placed in a region such as this will not yield accurate results.

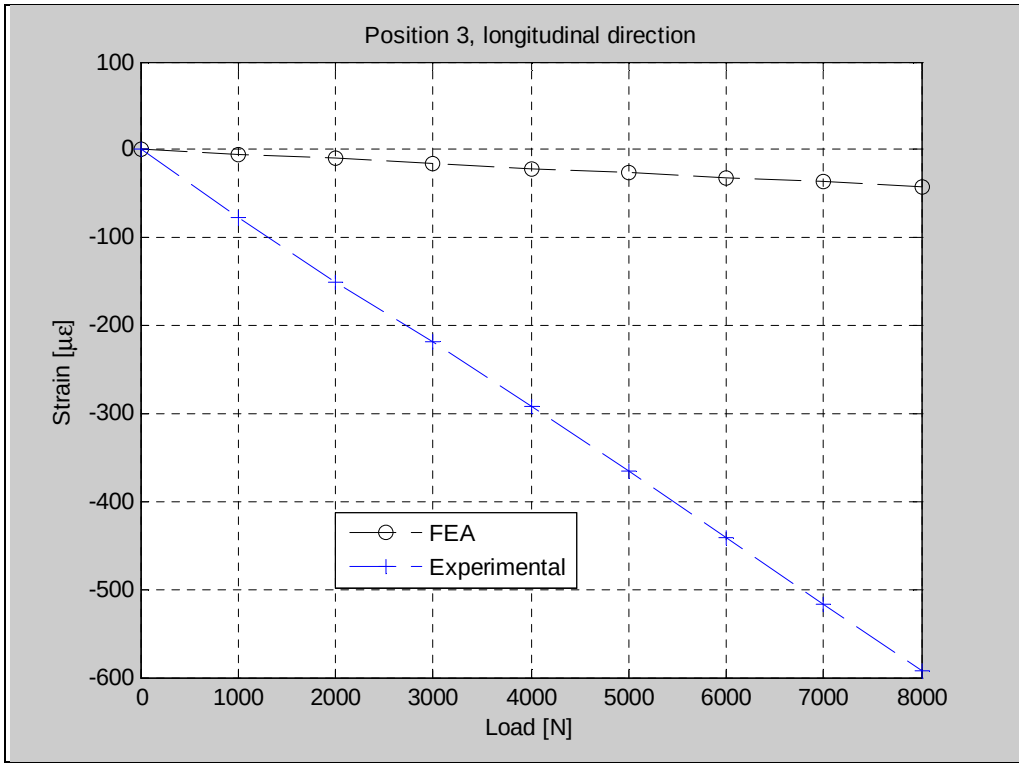


Figure 82. Comparison between FEA and experimental results at Position 3 in the gauge longitudinal direction.

The strain gauge transverse sensitivity error calculation reduces the measured strain to approximately -557 με. Rotating the axes through +2 degrees, a strain of -78 με is obtained shown in Figure 83. Therefore it can be concluded that the transverse sensitivity and the gauge misalignment do not play a significant role in the large difference obtained and that the difference is most likely due to the high strain gradient. Further strain gauge testing needs to be carried out in this area.

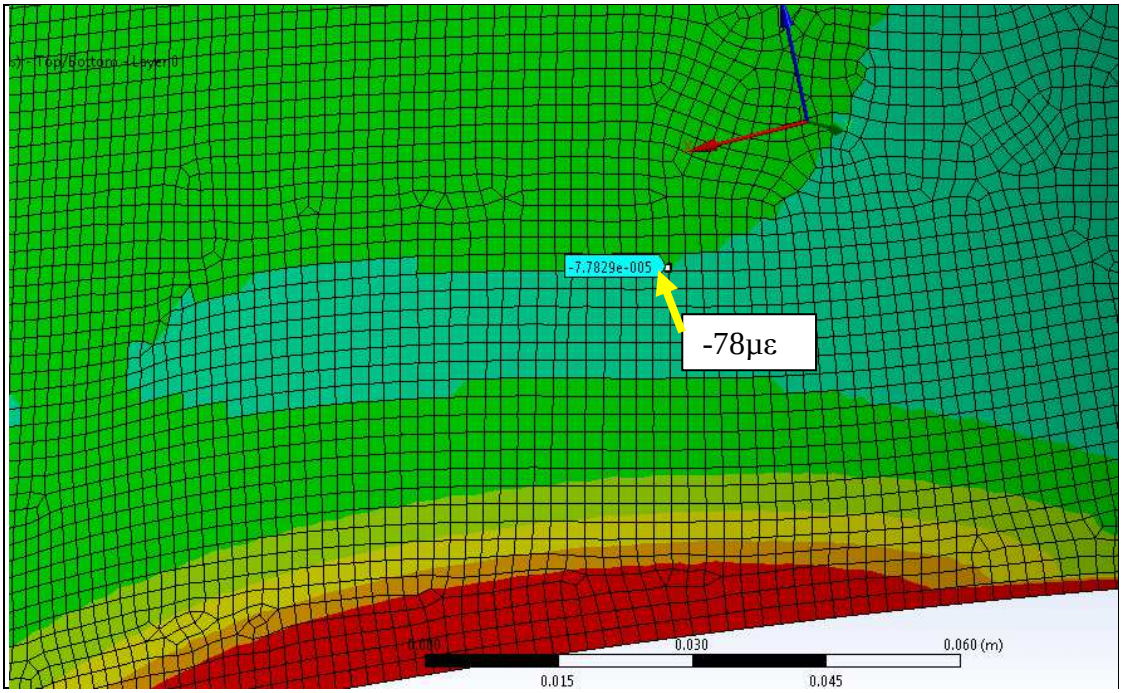


Figure 83. Strain at Position 3 in the longitudinal direction with the axes rotated +2 degrees.

The strain field around Position 3 in the gauge transverse direction (vertical direction in the figures) is shown in Figures 84 and 85 as approximately 430 $\mu\varepsilon$.

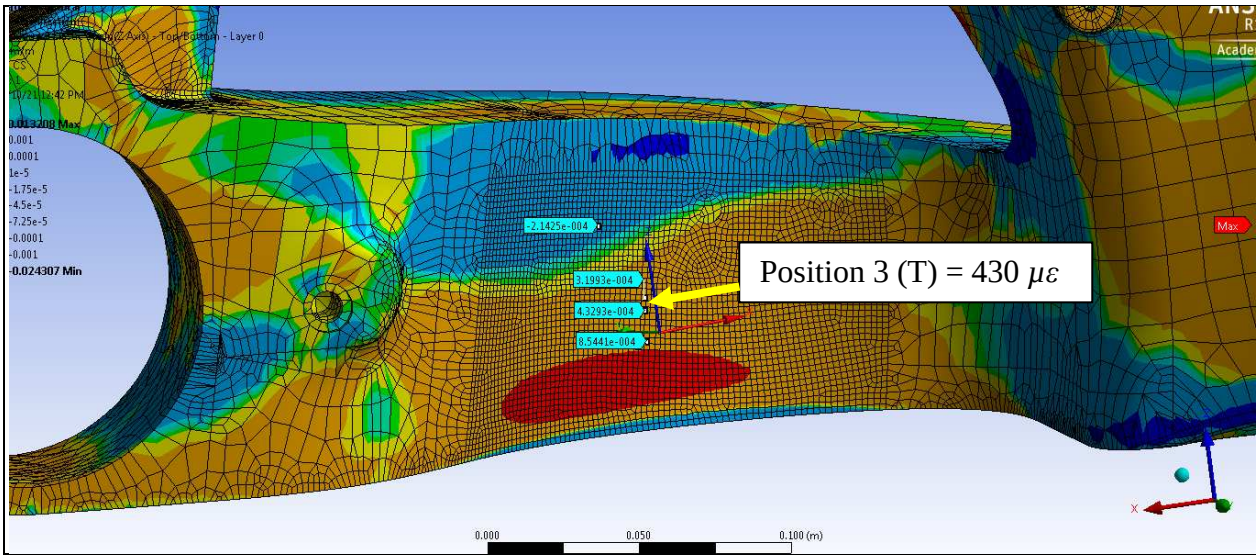


Figure 84. Strain distribution for Position 3 in the gauge transverse direction.

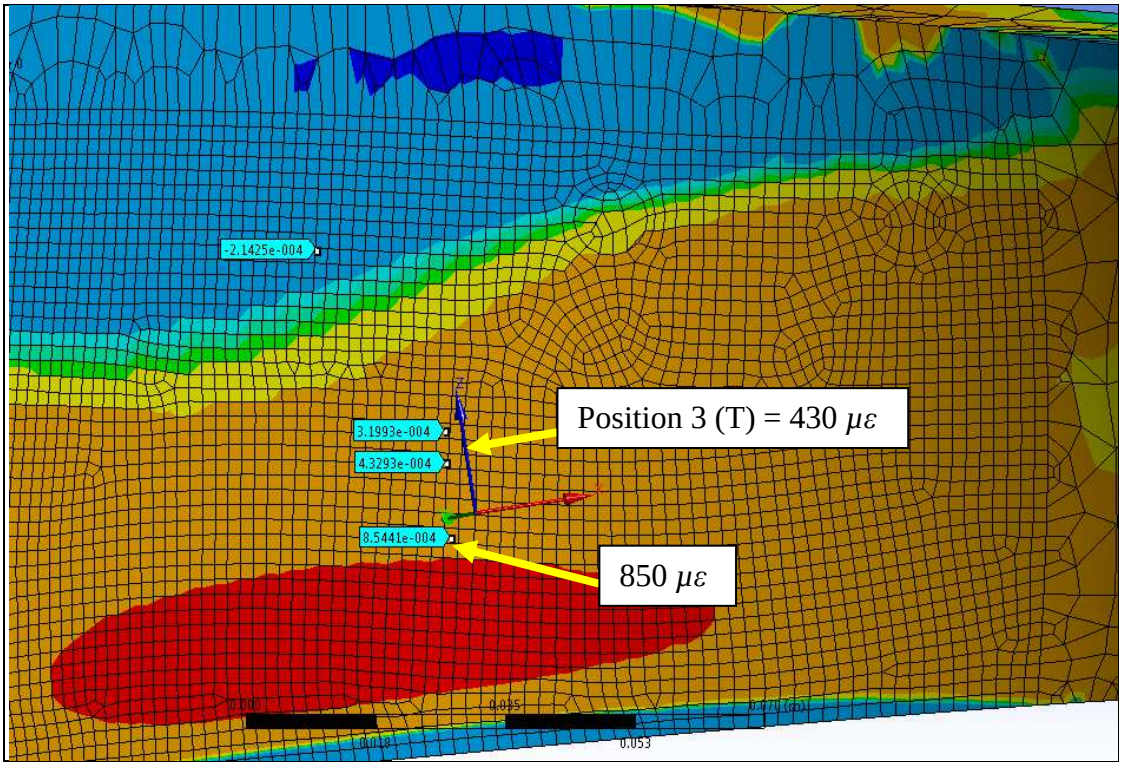


Figure 85. Close up of the strain distribution for Position 3 in the gauge transverse direction (vertical direction in the figure).

The experimental strain measured at 8000 N was approximately 850 με and a comparison between experimental and FE results over the range of loads is presented in Figure 86. The calculated difference in the FE and measured strains is 100 × (850 - 430)/830 = 49%. As can be seen in Figure 85 a strain of 850 με is found approximately 15 mm below the measurement point. This shows that although the exact point does not give the correct results, good correlation occurs nearby. Due to ply overlap, slightly different load paths exist in the real swingarm as compared to the model which plausibly explains the difference in the FE and measured strains.

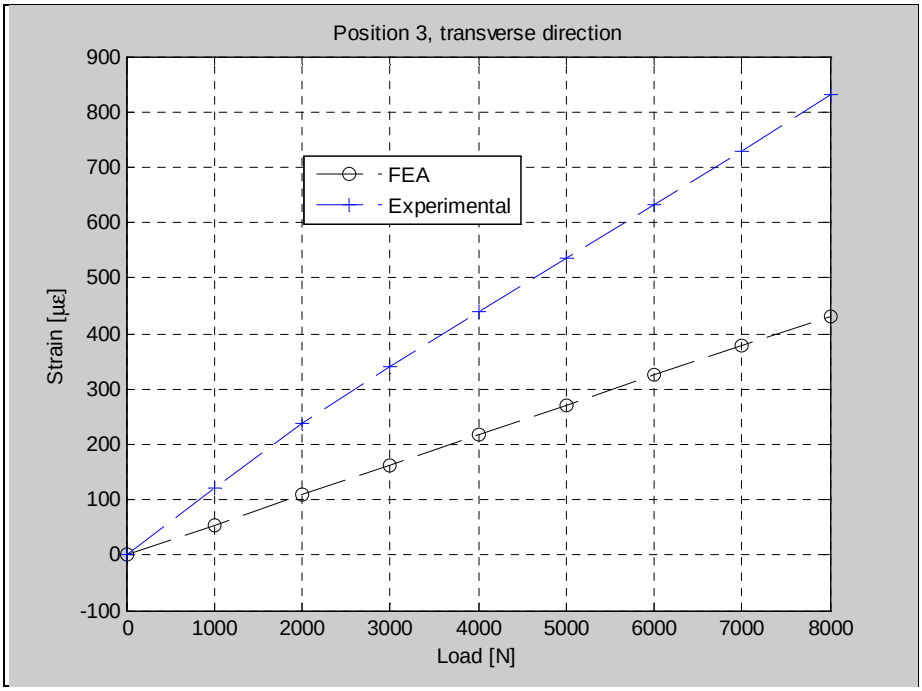


Figure 86. Comparison between FEA and experimental results at Position 3 in the gauge transverse direction.

Rotating the axes through -2 and +2 degrees does not significantly change the result in as shown in Figures 87 and 88. Also, the error due to transverse sensitivity was approximately 2% which would not significantly change the results. The large difference is then most likely due to ply overlap altering the load paths in that region.

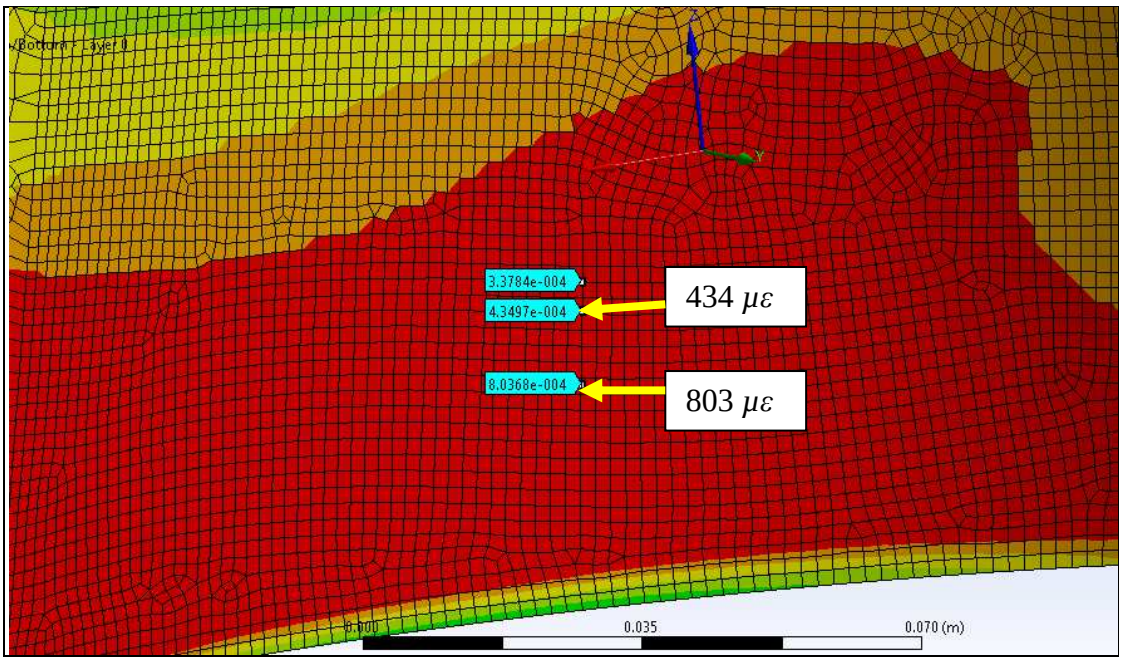


Figure 87. Position 3 in the transverse direction with axes rotated -2 degrees.

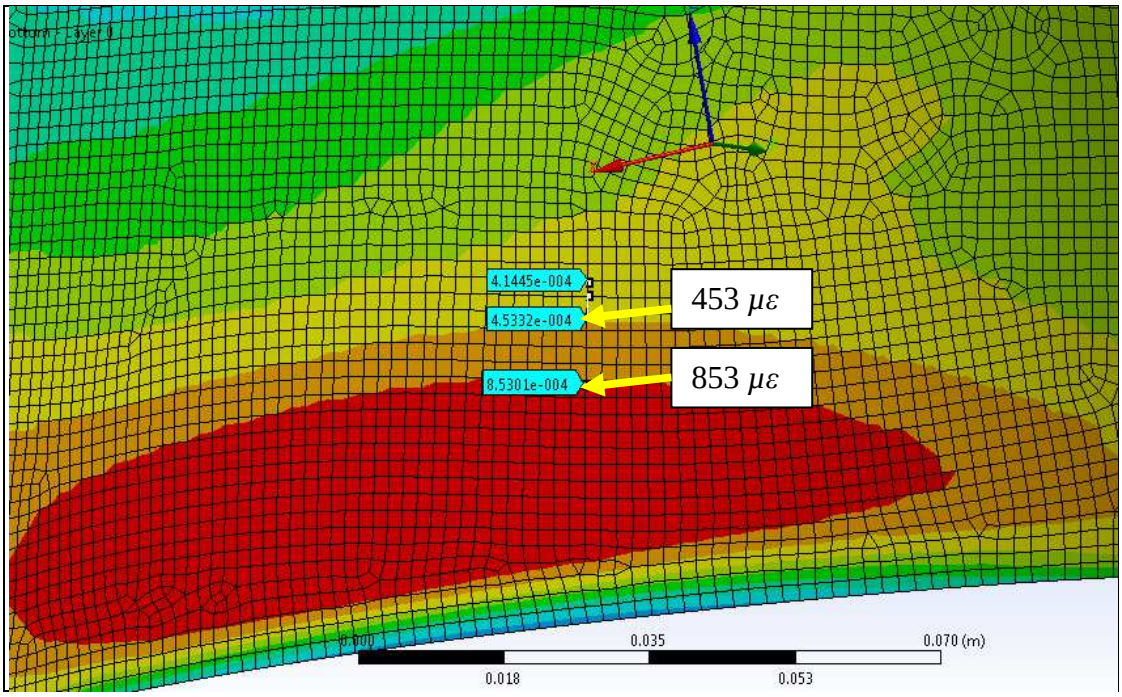


Figure 88. Position 3 in the transverse direction with axes rotated +2 degrees.

The strain in the longitudinal direction on the top side of the top arm (Position 4) was found to give very good results. Figure 89 shows the FE longitudinal strain distribution on the top arm with a value of -1100 με at Position 4. The measured strain was -1090 με and Figure 90 shows the comparison between experimental and FEA results for Position 4. An error of approximately 100 × (-1100 - (-1090)) / (-1100) = 0.9% was calculated. Therefore this result shows that the FE model corresponds well with the experimental results at certain positions.

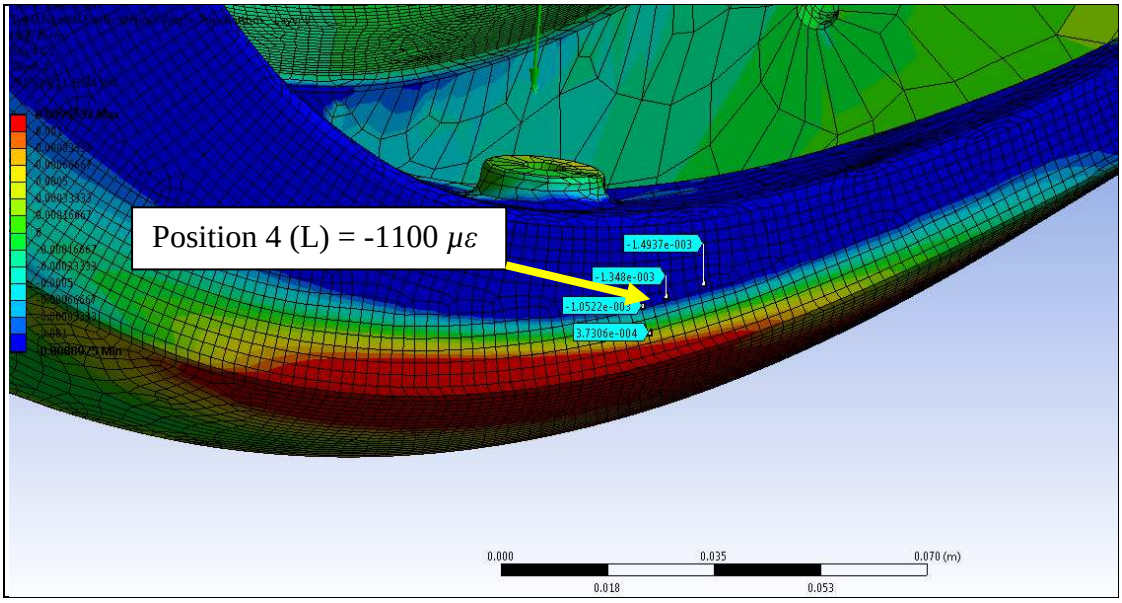


Figure 89. Strain distribution for Position 4 in the gauge longitudinal direction at 8000N.

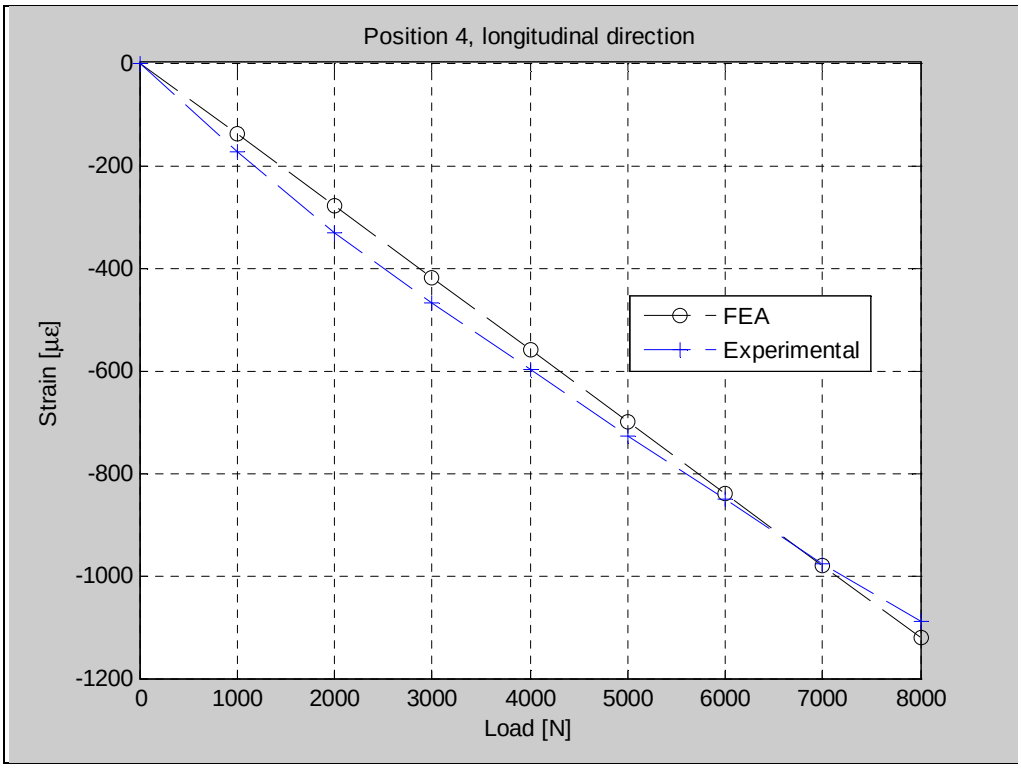


Figure 90. Comparison between FEA and experimental results at Position 4 in the gauge longitudinal direction.

When the axes were rotated through +2 and -2 degrees, longitudinal strains at Position 4 of -1122 $\mu\varepsilon$ and -1055 $\mu\varepsilon$ were obtained which do not significantly change the results. Error due to transverse sensitivity was calculated to be less than 1.7% (see Section 5.2) and therefore would not significantly affect the results either.

The strain on the top side of the top arm in transverse direction is shown in Figure 91 with the strain at Position 4 in the transverse direction being approximately +1700 με.

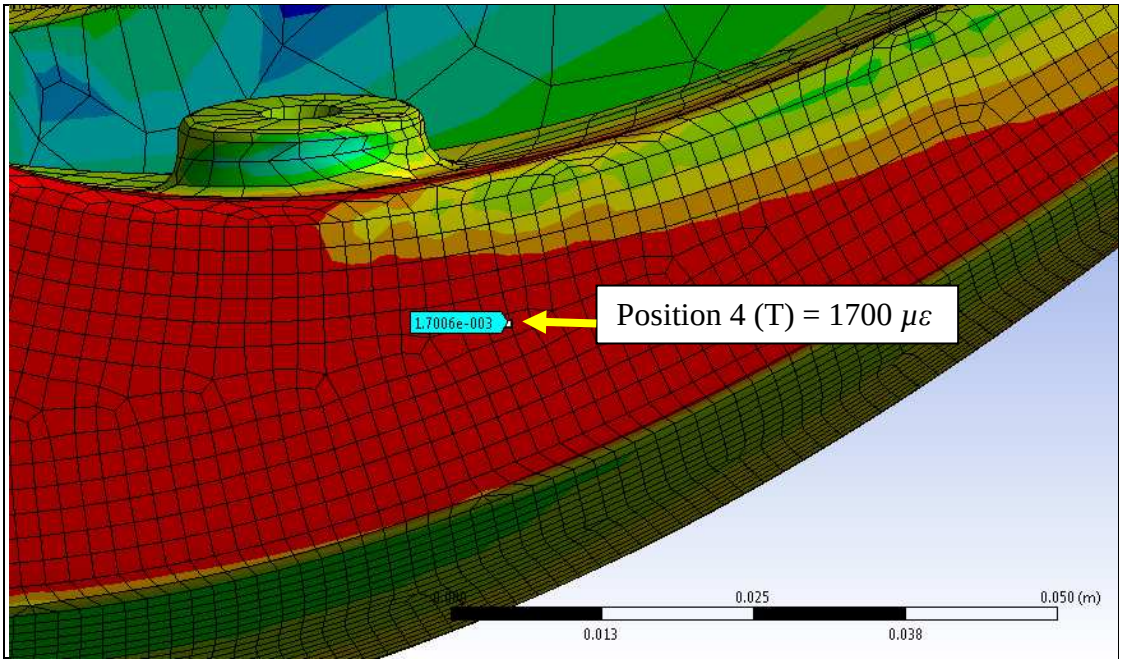


Figure 91. Strain distribution for Position 4 in the gauge transverse direction at 8000N.

The experimental result at 8000 N was approximately 660 με (see Figure 92), and a difference between the experimental and FE results of 157% was calculated which is exceedingly high.

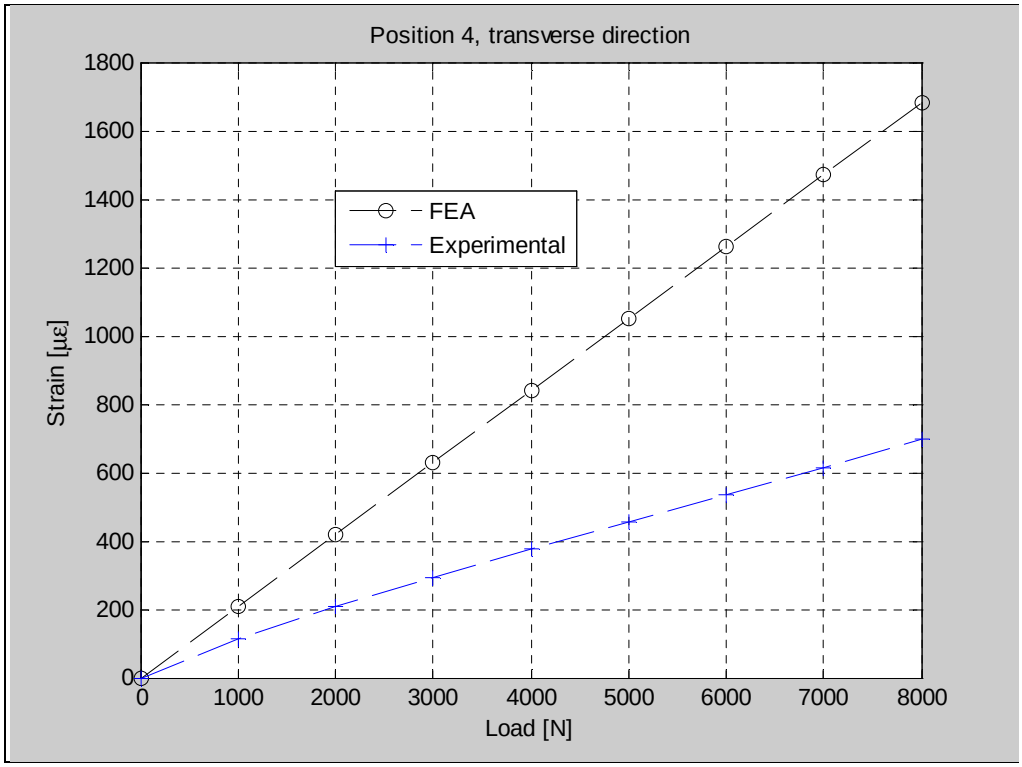


Figure 92. Comparison between FEA and experimental results at Position 4 in the gauge transverse direction.

Rotating the axes through +2 and – 2 degrees give values FE strain of 1820 με and 1690 με respectively and does not decrease the error significantly. Applying gauge transverse sensitivity effects, a measured strain of 702 με was calculated as shown in Table 8. Therefore it can be concluded that the differences are not due to sensitivity factors or gauge misalignment. Once again, the reader needs to be reminded that the swingarm and the layup of the swingarm is very complex. Not modelling the ply overlap due to the complexity of the swingarm was one of the major assumptions and to accurately model the overlap would present great difficulty. The layup on the top part of the top arm consisted mainly of ±45° woven plies with the fibre reference direction being along the longitudinal direction of the swingarm. In an attempt to simulate the overlap on the top arm, extra ±45° woven plies were added in this region because during layup the overlap consisted mainly of these types of plies. After adding three plies on the top, new longitudinal and transverse strains were calculated by the FEA and shown in Figures 93 and 94 respectively.

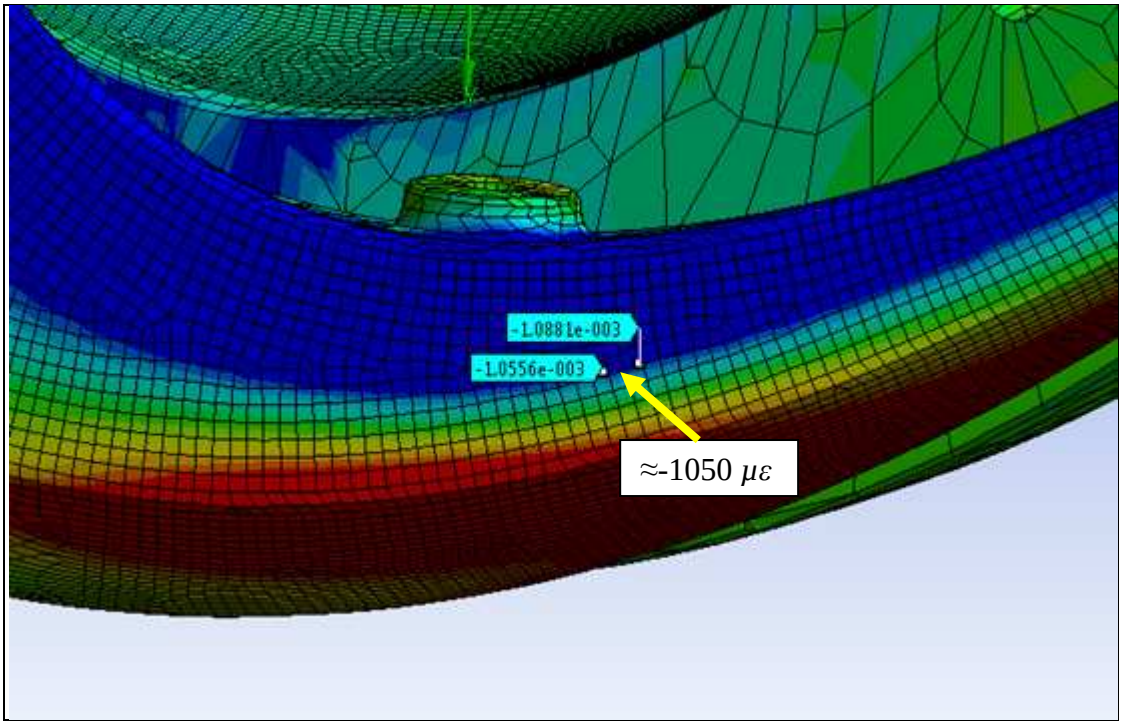


Figure 93. Updated longitudinal strain at Position 4 by adding 3 plies.

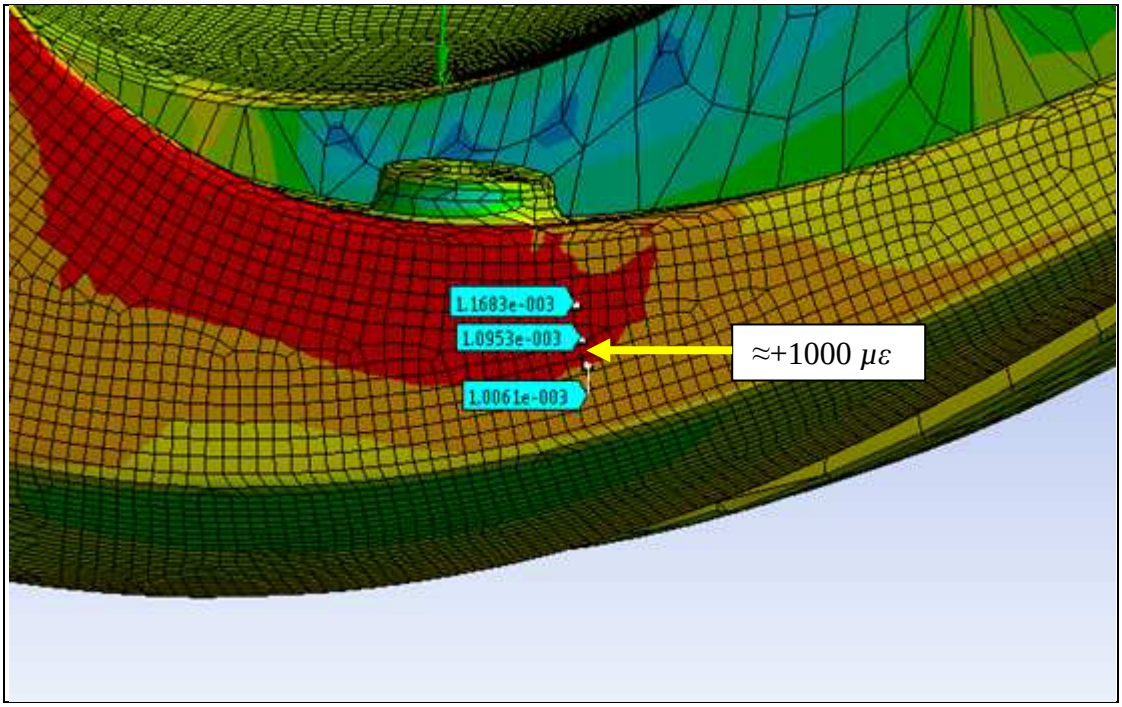


Figure 94. Updated transverse strain at Position 4 by adding 3 plies.

For the longitudinal strain, there was no noticeable difference with a strain of approximately -1050 με being calculated by the FE model. Therefore the FE strains remain the same in the longitudinal direction. However, simply by adding the three plies, the transverse strain was reduced from 1700 με to approximately 1000 με This

presents a reduction of about 40% and a new difference of just below 40% when compared with the experimental value of 725 $\mu\varepsilon$ at 8000 N. This exercise shows that by simply adding three plies to simulate some degree of overlap in that area, the transverse strain becomes more accurate and the longitudinal strain remains almost the same. The overlap plays a huge role in obtaining accurate transverse FE strain results but does not appear to affect the longitudinal strain results in this region. This may be due to high Poisson's ratio effects based on the ±45° plies. It is concluded therefore that if highly accurate results are to be obtained at Position 4 in the transverse direction, a method would need to be developed to accurately model the overlap.

The longitudinal strain calculated by the FE model at Position 5 (on the side of the top arm) is shown in Figure 95. Strain of approximately 1100 με was calculated by the FE model and the experimental value was 1050 με. The comparison between the experimental and FE results (Figure 96) show good correlation at this position (difference of 5%). Once again, good results have been found along the longitudinal direction and no significant difference was found when looking at transverse sensitivity and gauge misalignment.

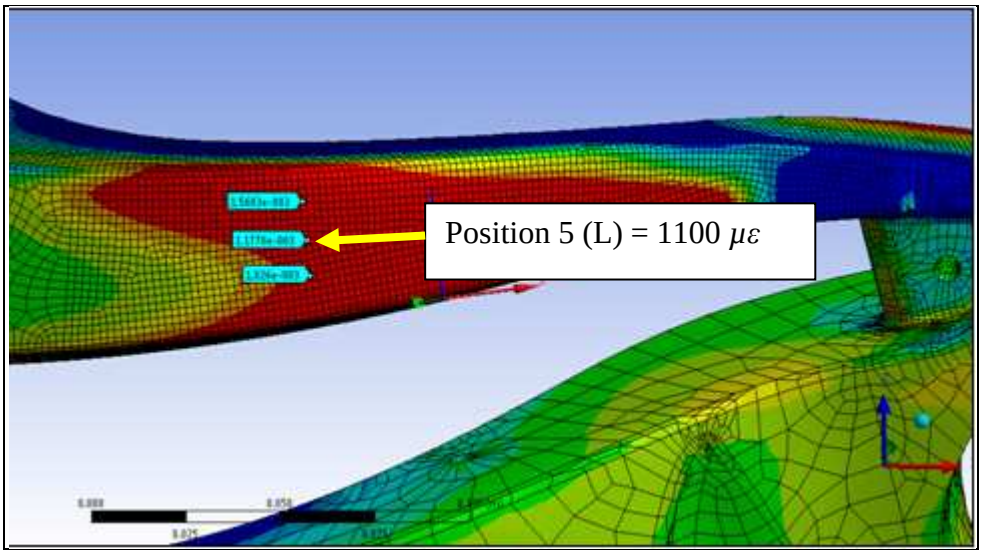


Figure 95. Strain distribution for Position 5 in the gauge longitudinal direction.

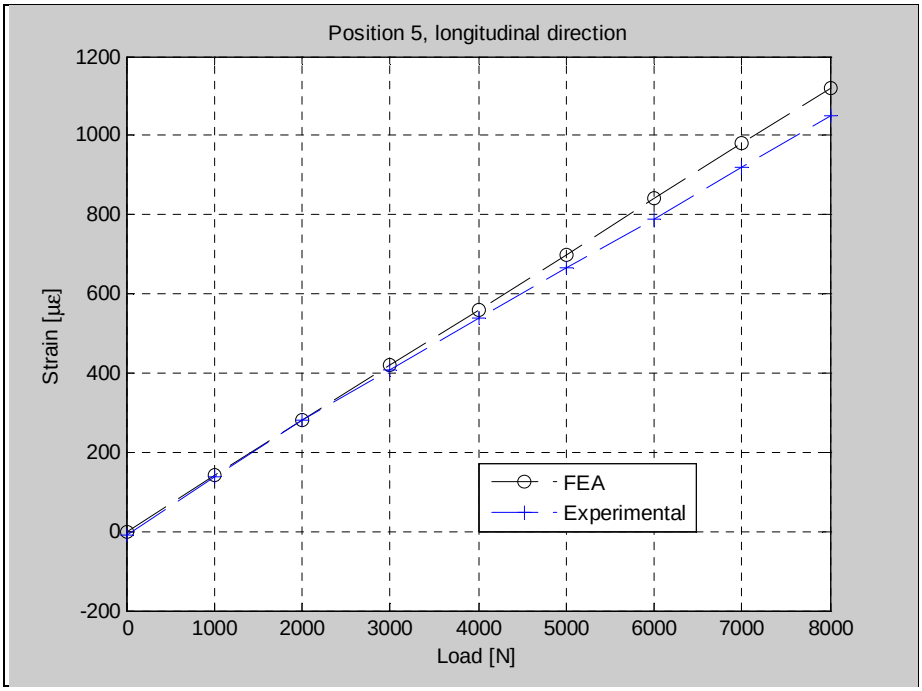


Figure 96. Comparison between FEA and experimental results at Position 5 in the gauge longitudinal direction.

Figure 97 shows the transverse strain distribution on the side of the top arm near Position 5. A strain of approximately -1200 με at Position 5 was found from the FEA. The experimental result was approximately -870 με which gives a difference of 38% (see comparison in Figure 98).

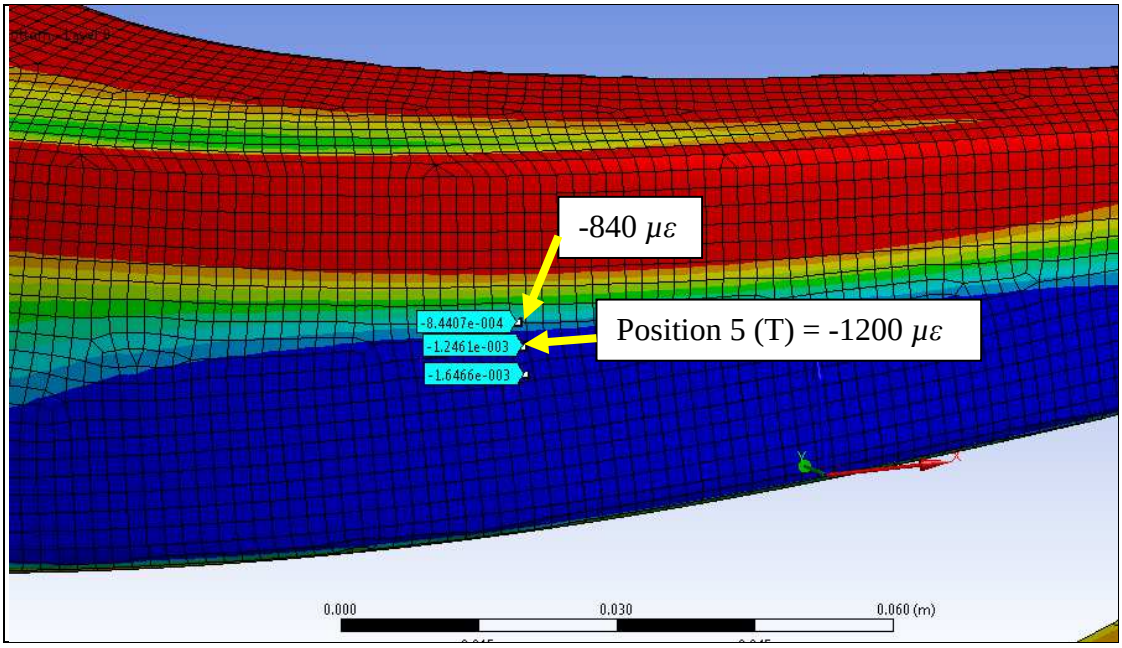


Figure 97. Strain distribution for Position 5 in the gauge transverse direction.

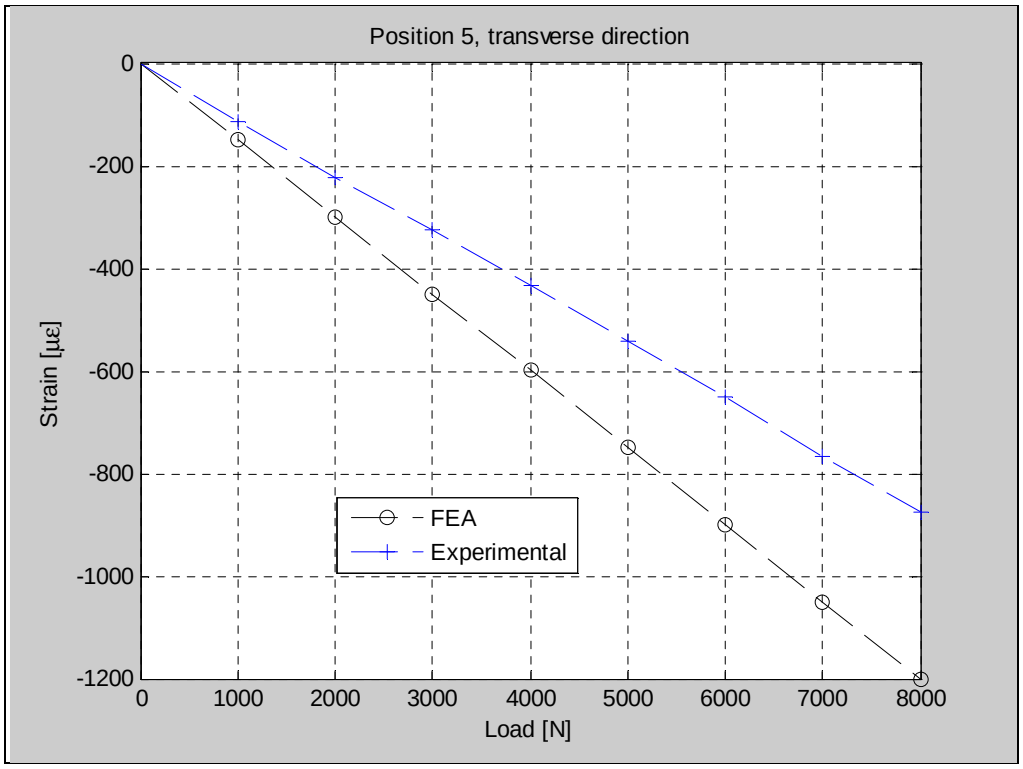


Figure 98. Comparison between FEA and experimental results at Position 5 in the gauge transverse direction.

Rotating the axes -2 degrees reduced the FE strain to -1188 $\mu\varepsilon$ which is not a significant change. The change in measured strain due to transverse sensitivity (-923 με from Table 8) reduced the difference to approximately 30% which is a significant difference. Once again, the difference is most likely due to the overlap not being modelled which causes different load paths. If the results are viewed approximately 10 mm above Position 5, then strains of approximately -840 με are found on the FE model which are very close to the measured value of -870 με. This shows that the FE load paths are slightly different to the actual load path due to different rigidity in the transverse direction. This position is therefore relatively accurate.

Figure 99 presents the strain distribution under the top arm (Position 6) in the longitudinal direction. It can be seen that the strain distribution is highly uniform and the longitudinal strain calculated by the FEA at Position 6 was approximately 1000 με. A strain of 725 με was measured during testing which results in a difference of approximately 38%. Figure 100 shows the comparison between experimental and FE results over the range of loads. A possible reason for this error could be due to the

narrowing of the arm and curve of the arm at this position. It was concluded earlier with respect to Position 4, that the increase in the ±45° plies does not play a role in changing the longitudinal strain. But in this case, because of the narrowing and curvature it is possible that the lack of overlap affects the longitudinal strain more. However, by moving up 10 mm (see Figure 99) a strain of approximately 730 με was found which is very close to the measured strain. This could again indicate that the inaccuracy is due to not modelling ply overlap which cause the load paths to be slightly different.

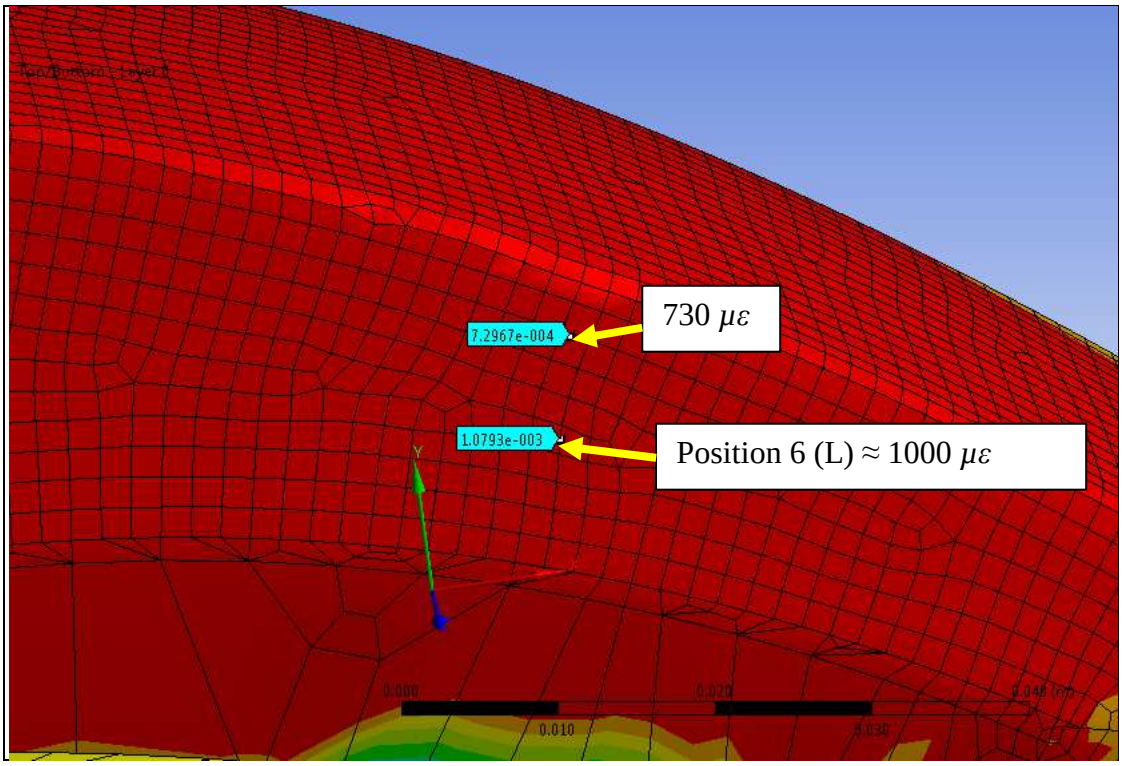


Figure 99. Strain distribution for Position 6 in the gauge longitudinal direction.

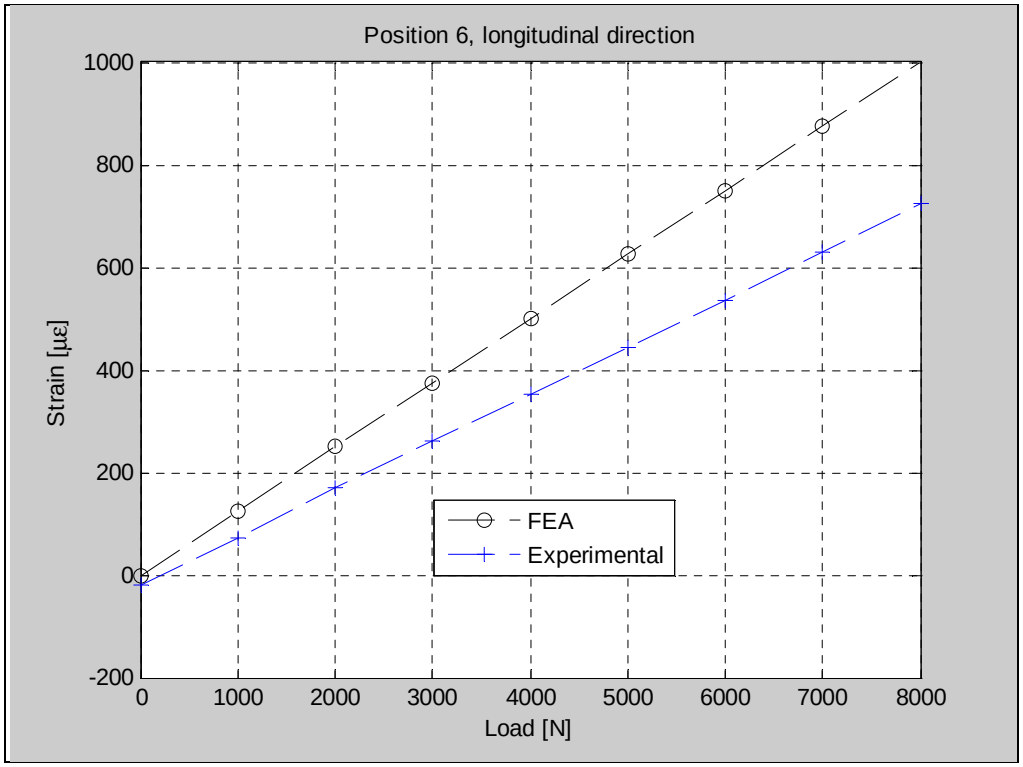


Figure 100. Comparison between FEA and experimental results at Position 6 in the gauge longitudinal direction.

To determine the effect of overlap in the region of Position 6, three ±45° plies were added to this section. Figure 101 shows that the new strain was found to be approximately 1100 με which suggests that the addition of the plies does not significantly change the longitudinal strain. This is similar to what was found earlier at Position 4 and 5, namely that the longitudinal strain is not significantly affected by the addition of ±45°plies. Furthermore, the effect due transverse sensitivity error (1.4%) and the rotation of the axes (with values of 1188 με and 1050 με) do not explain the difference. It is not certain what the 38% difference is due to, but as was shown in Figure 99, more accurate correlation is found within 10 mm above Position 6.

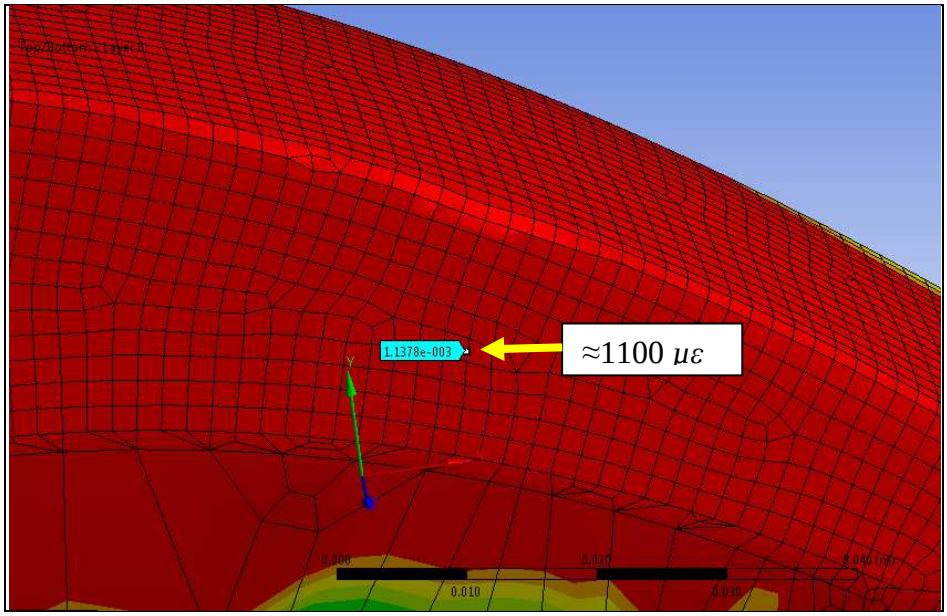


Figure 101. Longitudinal strain at Position 6 after adding three ±45° plies.

In terms of the transverse strain at Position 6, a value of approximately -830 $\mu\varepsilon$ was found as shown in Figure 102. The comparison between experimental and FE results is shown in Figure 103. Comparing the FE result (-830 $\mu\varepsilon$) with the measured strain (-394 $\mu\varepsilon$) gives a difference of approximately 110% which is very large. Before looking at possible reasons for the difference, Figure 102 shows that simply by moving 10 mm below Position 6, strain of approximately -400 $\mu\varepsilon$ is found which is very close to the measured result (less than 2% difference).

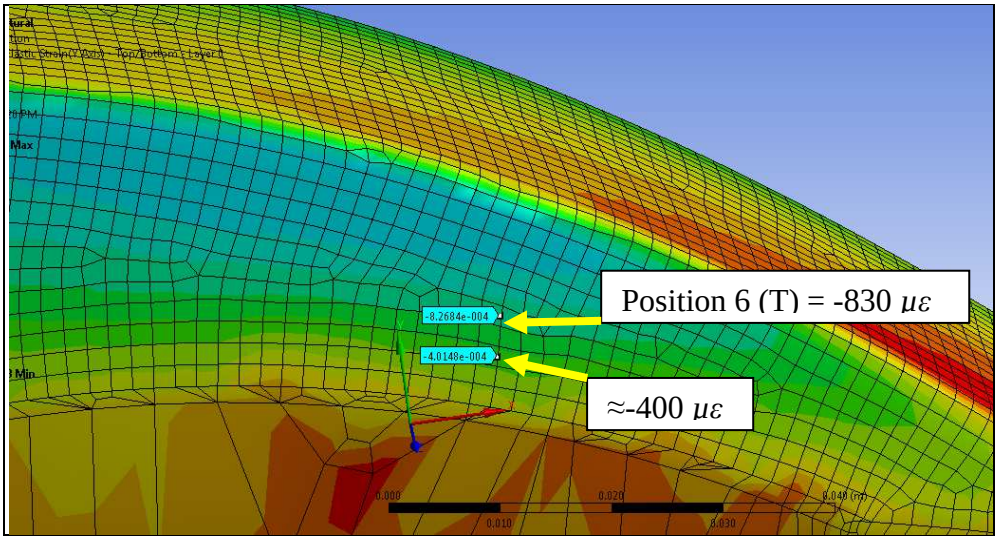


Figure 102. Strain distribution near Position 6 in the gauge transverse direction.

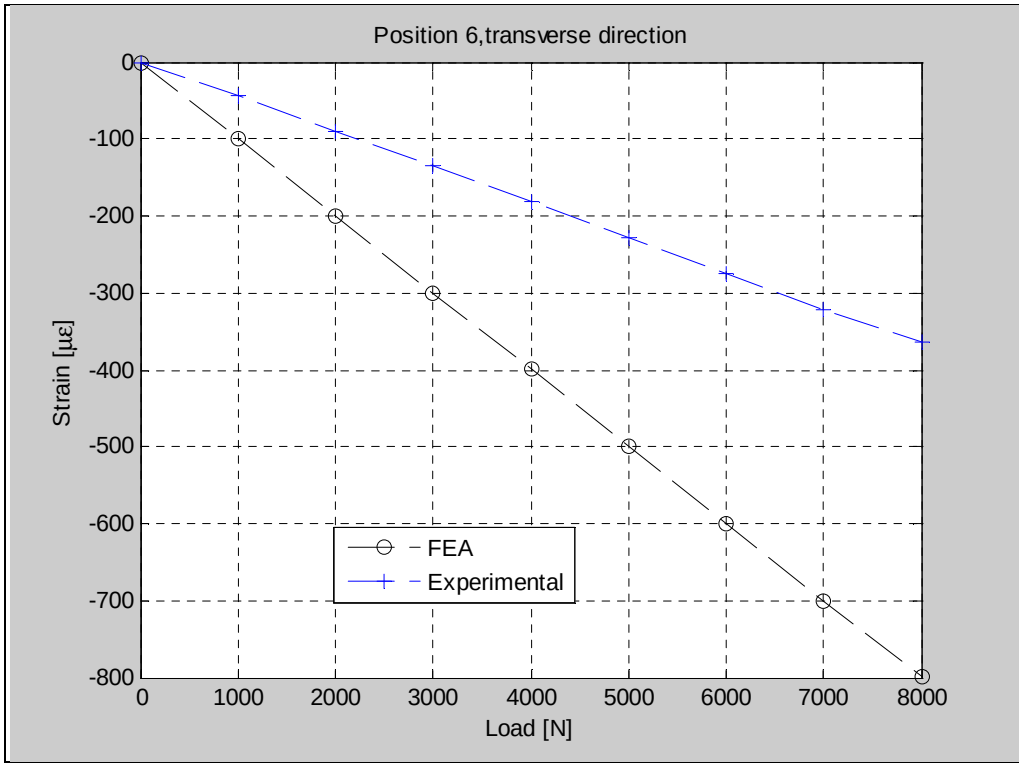


Figure 103. Comparison between FEA and experimental results at Position 6 in the gauge transverse direction.

By applying the three plies of ±45° (as discussed earlier) the strain at Position 6 become significantly more accurate. Figure 104 shows strain at Position 6 of approximately -400 $\mu\varepsilon$ which yields a difference of approximately 2%. Once again, the importance of modeling ply overlap is evident.

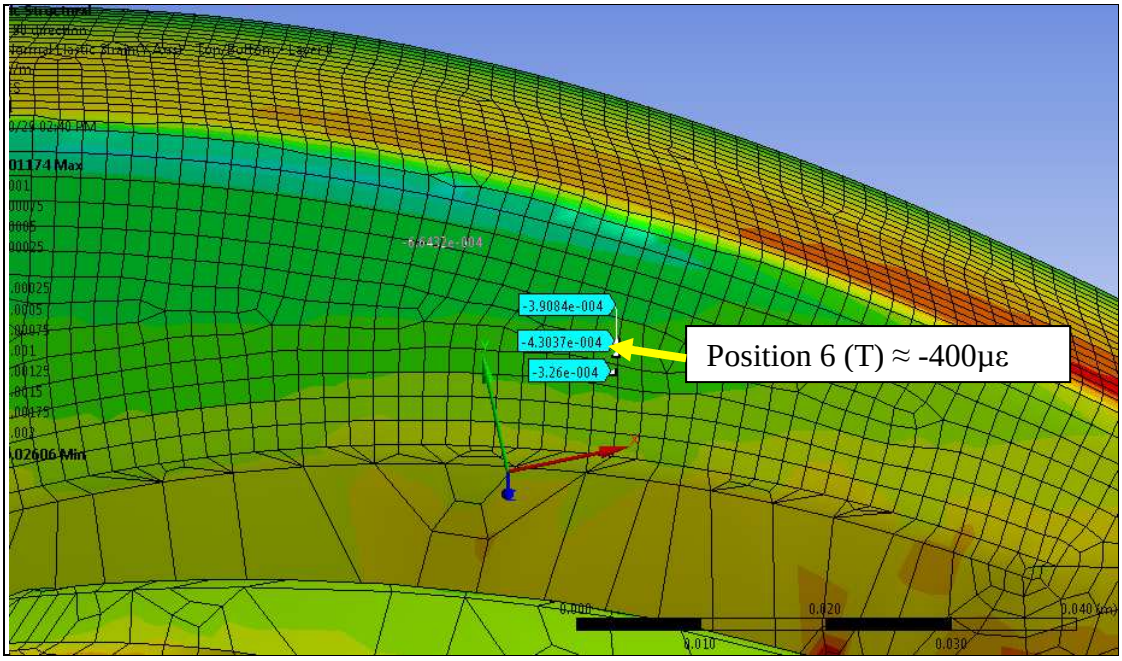


Figure 104. Strain distribution for Position 6 in the gauge transverse direction with the addition of 3 ±45° plies.

5.3.3 Effect of Ply Thickness on FE Model Accuracy

To add completeness and due to relatively large errors being found at certain points on the FE model, the effect of ply thickness on the results was also investigated.

Table 4 showed that the original thicknesses of the unidirectional and woven plies were 0.3 mm and 0.38 mm respectively. To study the effect of ply thickness, each thickness was changed by +5% and -5% and the results from Position 4 were evaluated and presented in Table 13. This exercise was to develop an indication of the effect of ply thickness so not all the positions were looked at.

Table 13. Effect of change in thickness of plies at Position 4.

Thickness change [%]	UD [mm]	Woven [mm]	Longitudinal strain [$\mu\varepsilon$]	Transverse strain [$\mu\varepsilon$]
+5	0.315	0.4	-1050	1560
-5	0.285	0.36	-1050	1850

The results show that by increasing both plies by 5%, the longitudinal strains remain the same but the transverse strain decreases by approximately 8% from the original

1700 $\mu\varepsilon$. The transverse strain is increased by about 9% when the thicknesses are decreased by 5%. Although not very large, the change in thickness of the plies definitely plays a role in the results obtained in the transverse direction. Therefore any slight error in the thickness could add to the reasons why differences were obtained.

5.3.4 Finite Element Model – Conclusion

The finite element model shows areas of satisfactory (less than 10%) and poor (>100%) correlation with the experimental results. The reader may consider some of these values to be highly unacceptable and generally this opinion would be valid. There is the need therefore for further discussion to justify the work.

It was briefly mentioned earlier that a strain gauge validation test was carried out before testing the swingarm (see Appendix A). The aim of the validation test was to determine if the readings obtained from the strain gauge measurement were closely matched by the calculations carried out using classical lamination theory. As discussed in Appendix A, the strain gauge results were compared with classical laminate theory results using FEA in ANSYS. It was shown there that differences of less than 2% were found for three separate tests. This is mentioned because for a very simple carbon fibre structure it is possible to get highly accurate results. The structure was a simple rectangular beam consisting of a number of plies at various orientations. But when a very complex structure such as the swingarm is modelled, it seems very challenging to obtain a finite element model of the swingarm to correlate with strain gauge measurements. The reasons for the differences in the results have been discussed above. These differences seem to be primarily due to ply overlap but can also be attributed to gauge misalignment, gauge transverse sensitivity and ply thickness. If the swingarm was made of an isotropic material, then most likely a much higher degree of correlation would be found.

A question then could be asked: is building a finite element model the best method for determining stress and strain distribution for such a complex composite structure? Most analysts would say it is and for simple structures it is easy to be convinced that it is the best method. But for a complex structure such as the carbon fibre swingarm, unless a method is found to model the numerous overlaps occurring over the

swingarm, it may not be possible to obtain accurate correlation. To obtain accurate results in certain areas of the swingarm may require the analyst to focus on a certain section and only model that section. The strains there would need to be determined by experimental measurement and then the forces and moments acting at that point could be reconstructed on the FE model. Therefore instead of modelling the entire swingarm in a more general way, a specific section could be modelled in a more accurate way.

6. CONCLUSION AND RECOMMENDATIONS

6.1 Conclusions

Carbon fibre has not been extensively used in the development of motorcycle components due to high costs and manufacturing constraints. Carbon fibre has a higher strength/stiffness to weight ratio than materials such as steel, aluminium and magnesium and therefore can provide better structural characteristics at lower weight. This research report presented the first step in the design process of a carbon fibre swingarm for a Ducati 1098 motorcycle. Using preliminary carbon fibre laminate designs, the aim was to develop a swingarm that exhibited satisfactory strength under typical loading conditions with reduced weight.

The literature showed that it is important to characterize the stiffness of the swingarm for two reasons. The first is that the degree of rigidity of the swingarm affects the response time of the motorcycle when cornering. The second is the effect that the stiffness (specifically lateral and torsional) has on the weave mode stability of the motorcycle. Therefore the stiffness coefficients were calculated by measuring deflections in the vertical, lateral and torsional directions while the swingarm was subjected to typical loads experienced in the field. Lateral and torsional stiffness values of 445 kN/m and 550 Nm/deg respectively, were determined from the deflection measurements. Both values are on the lower end of the spectrum when compared with other stiffness values found in the literature. The lower lateral and torsional stiffness values may negatively affect the weave mode stability of the motorcycle at medium to high speeds and also cause the motorcycle to have a sluggish response when turning. The vertical stiffness coefficient was calculated to be 500 kN/m and was deemed sufficiently rigid to not negatively affect the effective stiffness between the chassis and wheel.

Results from the strain measurements were found to be considerably lower than the ultimate strains for the type of laminates employed in the design. Longitudinal and transverse strain was measured at eight positions on the swingarm. Even at high vertical loads of 8000 N and moments about the longitudinal axis of 680 Nm (applied separately), the measured strain did not exceed values of 1100 $\mu\varepsilon$ in tension or compression. These values were well under the ultimate strain for typical

unidirectional and woven plies of between 5000 $\mu\varepsilon$ and 8000 $\mu\varepsilon$. It is concluded that the swingarm is sufficiently strong at the positions that were measured. Furthermore, the strain measurements show that during vertical loading, there is a coupling between vertical and torsional loading. This means that due to the asymmetric design of the swingarm, as a vertical load is applied, there is also a twisting of the swingarm. Results also suggest that during vertical loading, the limiting position is the side of the top arm, Position 5. This means that during increased vertical loading, Position 5 measures the highest strain in both the longitudinal and transverse direction and will therefore most likely fail first. Similarly, Position 6 (underside of the top arm) is the limiting factor during torsional loading.

In terms of weight, the carbon fibre swingarm was measured to be 1.5 kg less than the original aluminium swingarm which satisfies the requirement for a reduction in weight.

A finite element model of the composite swingarm was developed based on the following assumptions: not modelling ply overlap and the aluminium inserts and simplifying the modelling to model only the major zones. In terms of deflection, good correlation was found for the vertical deflection (less than 5%). Less accurate results were obtained for the torsional (28%) and lateral (50%) deflection. Reasons for the large difference in lateral deflection are most likely due to the very low deflection measurements of less than 1 mm and not modelling ply overlap. To obtain a higher degree of accuracy, it may be necessary to apply loads of an order of magnitude higher for the lateral deflection.

When comparing the FE strain results with the experimental strain gauge values in order to further validate the model, a range of differences between 0.9% and 157% were initially found. Two areas were focused on in terms of FEA strains, namely the bottom and top arms of the swingarm. On the lower arm two positions were measured in the longitudinal and transverse directions. Results showed differences of between 49% and 93% which are significantly large. This can be attributed to the strain gauge measurements being placed in a rapidly changing strain field. For two out of the three positions on the lower arm, accurate results (less than 10% difference) were found within 10 mm to 20 mm from the measurement position on the FE model.

This may indicate that due to not modelling ply overlap, the load path is slightly different.

Three positions were measured on the top arm in longitudinal and transverse directions. The longitudinal results showed differences of 0.9%, 5% and 38% for Positions 4, 5 and 6 respectively. Although Position 6 produces differences that are large, very accurate results are found 10 mm above the measurement position. The longitudinal strain on the top arm therefore produced acceptable results.

Positions 4, 5 and 6 in the transverse direction produced differences of 157%, 38% and 110% respectively. Gauge transverse sensitivity and gauge misalignment were looked at for possible reasons for the differences but did not show significant improvements in the results. Position 5 was shown to have very accurate results 10 mm above its measurement point. An attempt to simulate ply overlap was carried out in these areas by simply adding three ±45°plies. The results were drastically improved. Position 4 improved from 157% to just below 40% difference and Position 6 improved from 110% to less than 2%. This exercise showed the major effect that ply overlap has on the results. A summary of the comparison between FE and experimental strain is presented in Table 14.

Table 14. Comparison of experimental and FE strain results.

Position	Exp. strain [με]	FE strain [με]	Difference [%]	Notes	New FE strain [με]	Difference after addition of 3 ±45°plies [%]
2 L	-	-	-	• No reading on DAQ	-	-
2 T	-450	-230	49	• Error due to high strain gradient, • Accurate strain 10mm to the right	-	-
3 L	-592	-43	93	• Error due to high strain gradient	-	-
3 T	850	430	49	• Error due to no ply overlap	-	-

				• Accurate strain 15mm below		
4 L	-1090	-1100	0.9	-	-	-
4 T	660	1700	157	• Error due to no ply overlap • Add 3 plies to simulate overlap	1000	40
5 L	1050	1100	5	-	-	-
5 T	-870	-1200	38	• Error due to no ply overlap • Accurate strain 10mm above	-	-
6 L	725	1000	38	• Error due to no ply overlap • Accurate strain 10mm above • Add 3 plies to simulate overlap	-	-
6 T	-394	-830	110	• Error due to no ply overlap • Accurate strain 10mm above • Add 3 plies to simulate overlap	400	2

6.2 Recommendations

The stiffness values of the original aluminium swingarm were not known and although the stiffness results suggest the motorcycle will exhibit slow response and lower stability, a clearer picture will be obtained if a direct comparison is made with the original aluminium swingarm. Furthermore, to determine the actual response and stability of the swingarm, there would be the need to carry out experimental testing during motorcycle operating conditions.

With regard to the FE model, it is of vital importance that a method is devised to accurately model ply overlap for future research. Both the torsional and lateral deflections and the transverse strains depend highly on ply overlap. Furthermore, if

highly accurate results are required then it may necessitate only modelling a specific part of the swingarm and focussing the analysis on that part alone.

7. REFERENCES

[1] H. Sol and W. de Wilde, “Identification of elastic properties of composite materials using resonant frequencies,” *Computational Mechanics Publications*, pp. 273-280, 1988.

[2] A. Airoldi, S. Bertoli, L. Lanzi, M. Sirna and G. Sala, “Design of a motorcycle composite swing-arm by means of multi-objective optimisation,” *Appl Compos Mater*, vol. 19, pp. 599-618, 2012.

[3] T. Foale, Motorcycle handling and chassis design, Spain: Tony Foale Designs, 2006.

[4] B. Madson, “Motorcycle-USA.com,” 14 August 2009. [Online]. Available: http://www.motorcycle-usa.com/363/4336/Motorcycle-Article/2010-Sachs-MadAss-125-First-Look.aspx?WT.i_e_dcsvid=1464738270. [Accessed 25 March 2013].

[5] G. Risitano, L. Scappaticci, C. Grimaldi and F. Mariani, “Analysis of the structural behavior of racing motorcycle swingarms,” *SAE Technical Paper 2012-01-0207*, 2012.

[6] K. H. C. C. Ltd, “DIY Trade,” 23 November 2009. [Online]. Available: http://www.diytrade.com/china/pd/6169920/alloy_swing_arm.html#normal_img. [Accessed 25 March 2013].

[7] T. Carrithers, “Motor Cyclist,” June 2011. [Online]. Available: http://www.motorcyclistonline.com/howto/answers/122_1106_dangerous_helmets_swingarms_and_valve_stem_cap_questions/. [Accessed 20 February 2013].

[8] E. Armentani, S. Fusco and M. Pirozzi, “Numerical evaluation and experimental tests for a road bike swingarm,” in *Science and Motor Vehicles JUMV International Automotive Conference with Exhibition*, Beograd, Serbia, 2007.

[9] S. Cassani and A. Mancuso, “Shape Optimization of a High Performance Motorbike Single Sided Swingarm,” *SAE International*, 2005.

[10] V. Cossalter, Motorcycle Dynamics, 2006.

[11] Unknown, “www.mindsetsonline.co.uk,” Mind Sets, 2013. [Online]. Available: http://www.mindsetsonline.co.uk/Catalogue/ProductDetail/genuine-carbon-fibre-sheet?productID=a00ac9d6-b444-425a-b52e-b4b6167f8181&catalogueLevelItemID=4d561b21-7a62-4ba3-896c-cd0b2ff19840. [Accessed 19 May 2014].

[12] W. University, “Mechanics of Composite Materials, MECN 4003 Notes,” South Africa, University of the Witwatersrand.

[13] N. O'Dea, “Motorcycle swingarm redesigned in carbon composite,” *Reinforced Plastics*, vol. 55,

no. 6, pp. 38-41, 2011.

[14] H. Iwasaki, A. Mizuta, T. Hasegawa and H. Yoshitake, “Development of a magnesium swing arm for motorcycles,” *SAE Technical Paper2004-32-0048,* 2004.

[15] J. S. Hoksbergen, M. Ramalu, P. Reinhall and T. M. Briggs, “A Comparison of the vibration characteristics of carbon fiber reinforced plastic plates with those of magnesium plates,” *Appl Compos Mater,* vol. 16, pp. 263-283, 2009.

[16] R. Sullivan, “Automotive carbon fiber: opportunities and challenges,” JOM, 2006.

[17] Unknown, “www.firehole.com,” Firehole Composites Analysis Software & Services, July 2011. [Online]. Available: http://www.firehole.com/news/quarter_02_2011/fpf.aspx. [Accessed 19 May 2014].

[18] J. Wood, “Finite element analysis of composite structures,” *Composite Structures,* vol. 29, pp. 219-230, 1994.

[19] B. S. Arms, “OPP Racing,” 2013. [Online]. Available: http://www.oppracing.com/image_display.php?image=54619&id=32189. [Accessed 25 March 2013].

[20] R. Kharul, S. Balakrishnan and D. Karedla, “Virtual testing and correlation for a motorcycle design,” *SAE Technical Paper2010-01-0925,* 2010.

[21] P. Wilkinson, “The changing role of physical testing in vehicle development programmes,” *Journal of Terramechanics,* vol. 44, p. 15, 2007.

[22] K. Dressler, M. Speckert and G. Bitsch, “Virtual durability test rigs for automotive engineering,” *Vehicle System Dynamics: International Journal of Vehicle Mechanics and Mobility,* vol. 47, no. 4, pp. 387-401, 2009.

[23] K. Lin, J. Chang, J. Wu, C. Chang, S. Chang, J. Hwang and C. Fung, “Durability assessments of motorcycle handlebars,” *SAE International,* no. 2005-01-0801, 2005.

[24] R. Ide, T. Ogushi, Y. Sunayama, Y. Kishita and S. Watanabe, “Estimating of motorcycle frame strength by virtual durability test,” *SAE International,* no. 2009-32-0143, 2009.

[25] Mira, “www.mira.co.uk,” 2014. [Online]. Available: http://www.mira.co.uk/facilities. [Accessed 21 May 2014].

[26] E. Dragoni and F. Foresti, “Design of a single-sided composite swing arm for racing motorcycles,” *Int. J. of Materials and Product Technology,* vol. 13, no. 3-6, pp. 411-420, 1998.

[27] V. Cossalter, R. Lot and M. Massaro, “The influence of frame compliance and rider mobility on

the scooter stability," *Vehicle System Dynamics: International Journal of Vehicle Mechanics and Mobility,* vol. 45, no. 4, pp. 313-326, 2007.

[28] K. Lake, R. Thomas and O. Williams, "The influence of compliant chassis components on motorcycle dynamics: an historical overview and the potential future impact of carbon fibre," *Vehicle System Dynamics: International Journal of Vehicle Mechanics and Mobility,* vol. 50, no. 7, pp. 1043-1052, 2012.

[29] R. Sharp, "Research Note: The influence of frame flexibility on the lateral stability of motorcycles," *J. Mech. Eng. Sci,* vol. 16, no. 2, pp. 117-120, 1974.

[30] D. Systemes, "plmmarketplace.com," Dassault Systemes, 2002-2013. [Online]. Available: http://www.plmmarketplace.com/blog/CategoryView,category,Simulayt.aspx. [Accessed 21 May 2014].

[31] C. Stan, Development trends of motorcycles II, Germany: Expert Verlag, 2005.

[32] M. Tuttle and H. Brinson, "Resistance-foil strain-gage technology as applied to composite materials," *Experimental Mechanics,* vol. 24, no. 1, pp. 54-65, 1984.

[33] "Errors due to transverse sensitivity in strain gages," *M-M Tech. Note TN-509, Micro-Measurements Division, Measurement Group, Inc., Raleigh, NC,* 1982.

[34] R. Ali, "Use of finite element technique for the analysis of composite structures," *Computers & Structures,* vol. 58, no. 5, pp. 1015-1023, 1996.

[35] Z. Yinhuan, X. Ka and H. Zhigao, "Finite element analysis of composite leaf spring," in *The 6th Internatonal Conference on Computer Science & Education*, Singapore, 2011.

[36] H. Mian, G. Wang, U. Dar and W. Zhang, "Optimization of composite material system and lay-up to achieve minimum weight pressure vessel," *Appl Compos Mat,* 2012.

[37] R. Chacko, "Design and experimental validation of a carbon fibre swing arm test rig.," University of the Witwatersrand, Johannesburg, 2013.

[38] R. Hibbeler, "Simplification of a force and couple system," in *Engineering mechanics statics twelfth edition in SI units*, Singapore, Prentice Hall, 2010, p. 160.

[39] P. Benham, R. Crawford and C. Armstrong, Mechanics of Engineering Materials, Singapore: Pearson Education Limited, 1996.

[40] M. Pinfold and G. Calvert, "Experimental analysis of a composite automotive suspension arm," *Composites,* vol. 25, no. 1, pp. 59-63, 1994.

[41] P. Beardmore, "Composite structures for automobiles," *Compos. Struct.,* vol. 5, pp. 163-176, 1986.

[42] G. Smith, “Design and production of composites in the automotive industries,” *Compos. Manuf,* vol. 1, no. 2, pp. 112-116, 1990.

[43] K. Edwards, “Strategic substitution of new materials for old: applications in automotive product development,” *Materials and Design,* vol. 25, no. 6, pp. 529-533, 2004.

[44] T. Foale, Motorcycle handling and chassis design, Tony Foale Designs, 2006.

Appendix A Strain Gauge Validation

Prior to applying strain gauges to the swingarm, it was necessary to compare results from a basic strain gauge application with results using classical laminate theory. A carbon fibre plate consisting of a number of plies of various types and orientations was fixed at one end and a load was applied at the other end as shown in Figure 105.

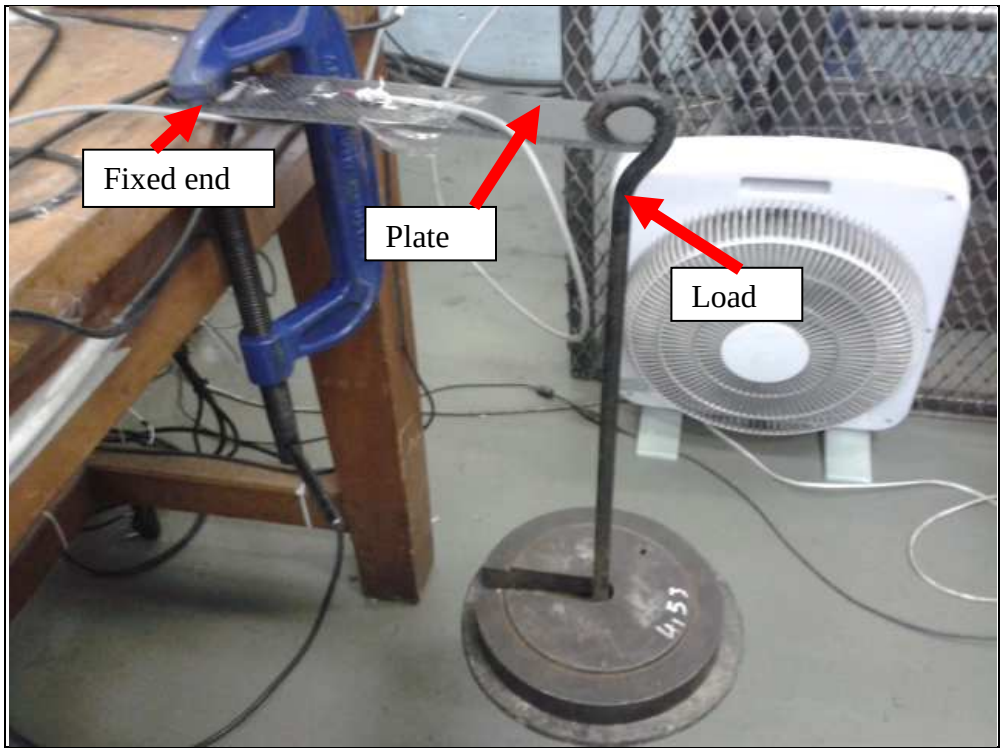


Figure 105. Rig setup for testing the carbon fibre plate.

The plate that was used, closely resembled one of the main layups used in the swingarm but the details are withheld here.

A load was applied toward the end of the beam which would cause a maximum bending moment near the fixed side (as well as a constant shear force along the plate). An axial strain gauge (see Figure 106) was mounted near the fixed end of the plate and the strain along the length of the plate was measured.

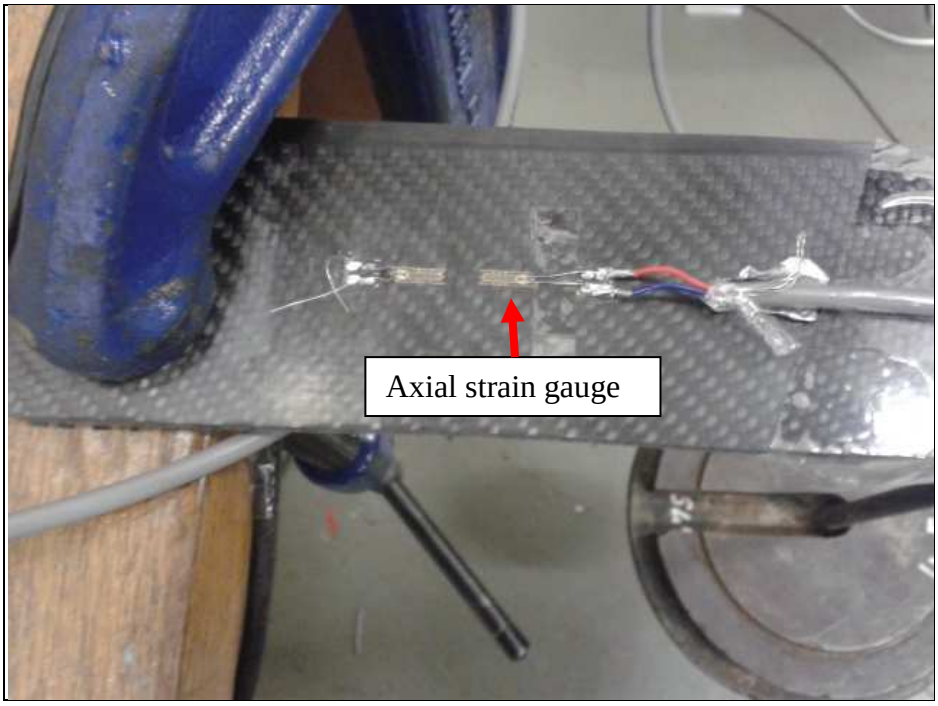


Figure 106. Axial strain gauge applied near the fixed end of the plate.

The length, width and height of the plate were 200 mm, 50 mm and 5 mm respectively. As a further validation test, it was decided to use ANSYS Composite PrepPost to calculate the strain based on classical laminate theory and at the same time determine the accuracy of ANSYS Composite.. Three tests were carried out with increasing load applied at the end of the beam. The load and the measured strain are presented in Table 15.

Table 15. Load applied to cantilever plate and the resultant axial strain from experimental setup.

Load [N]	Measured strain [$\mu\varepsilon$]
34.8	509
79	1117
123	1732

Thereafter, the carbon fibre plate was built in ANSYS Composite PrepPost and the same constraints and loads were applied to the model. Figure 107 shows the plate with the applied force at one end and a fixed support at the other end.

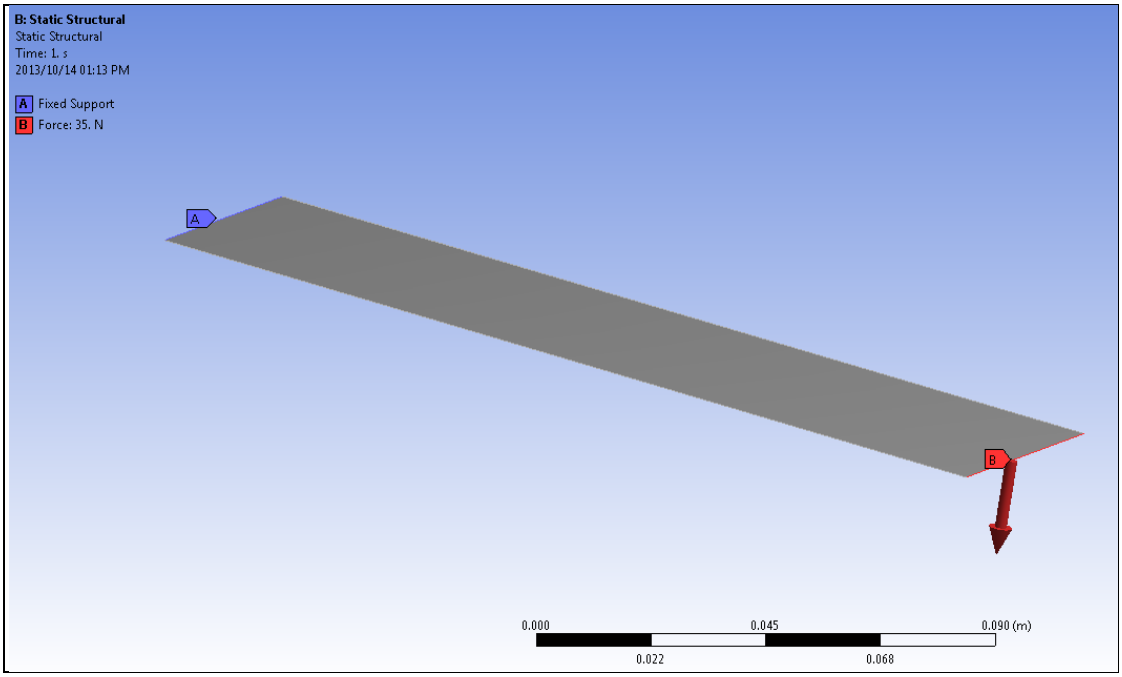


Figure 107. Constraints applied to the carbon fibre plate created in Ansys Composite.

Figure 108 presents the strain along the plate in graphical form after the first load of 35 N was applied.

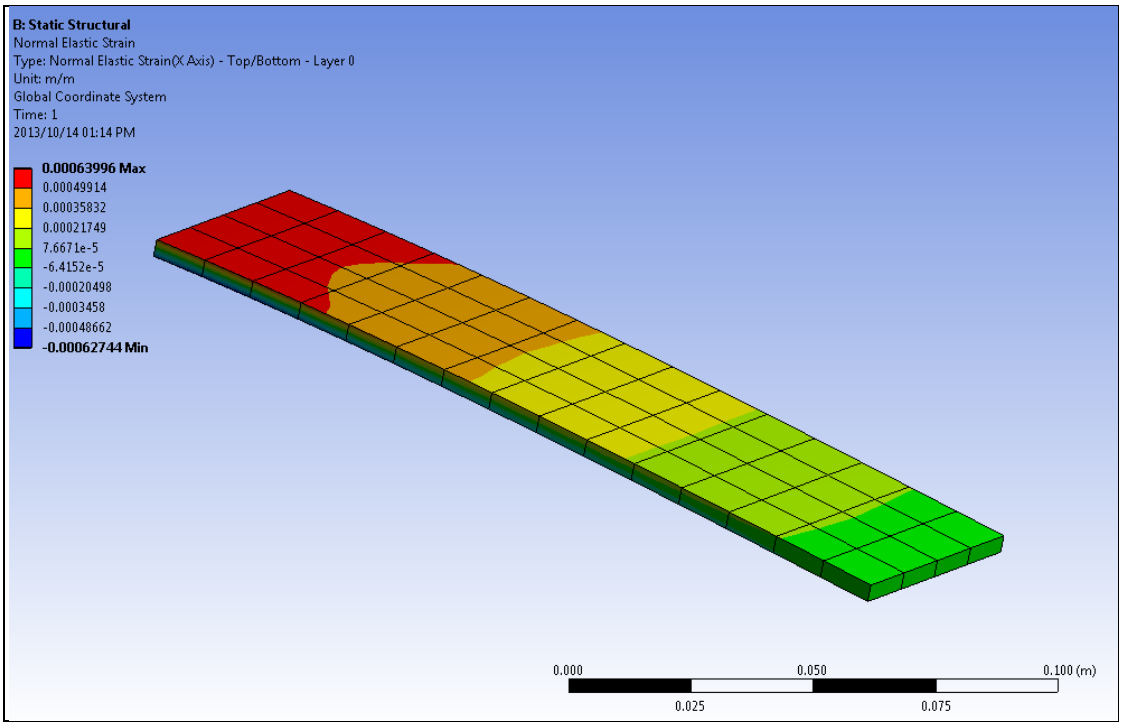


Figure 108. Graphical FEA results for the cantilever plate.

Figure 109 shows the strain of 499 $\mu\varepsilon$ calculated at the same position as the strain gauge.

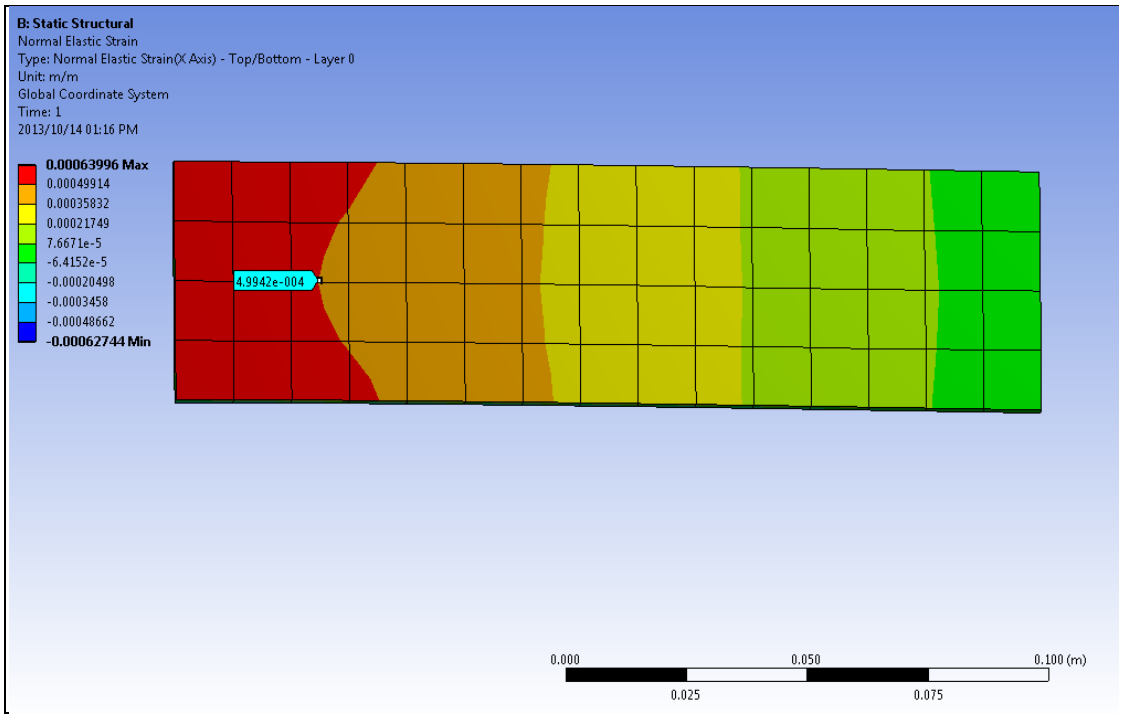


Figure 109. Longitudinal strain of 499 $\mu\varepsilon$ obtained from Ansys Composite.

Table 16 shows that the FEA which utilizes classical laminate theory, calculated results within 2% of the measured strain. The remaining two measurement values were also compared and both had differences of less than 2%

Table 16. Comparison between the measured strain and the strain calculated by ANSYS.

Measured strain [$\mu\varepsilon$]	FEA [$\mu\varepsilon$]	% difference
509	499	2
1117	1125	1
1732	1757	1.5

The experimental strain results very closely match the classical laminate theory results and this exercise also shows a degree of confidence in the results calculated by ANSYS Composite. It was therefore felt that the results were validated.

Appendix B Load Cell Calibration

A 50kN load cell was used during the testing to read the applied loads. The following presents the calibration of the load cell unit. The load cell was attached to a crane via a steel chain as shown in Figure 110.

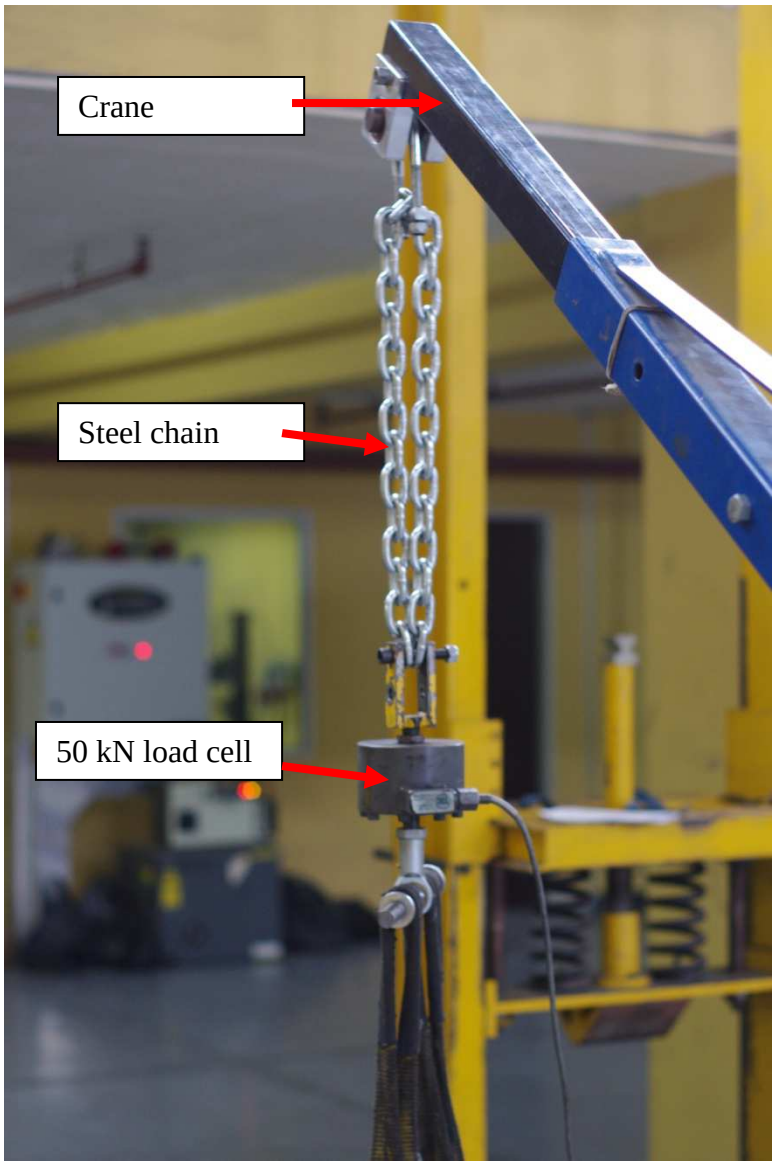


Figure 110. Top part of the load cell calibration rig showing the load cell attached to the portable crane via a steel chain.

A basket was hung from the load cell via a belt as shown in Figure 111. Known weights were placed inside the basket to apply the loads and the value shown on the load cell display was read. Table 17 presents the total mass applied to the load cell and also the load cell readings.

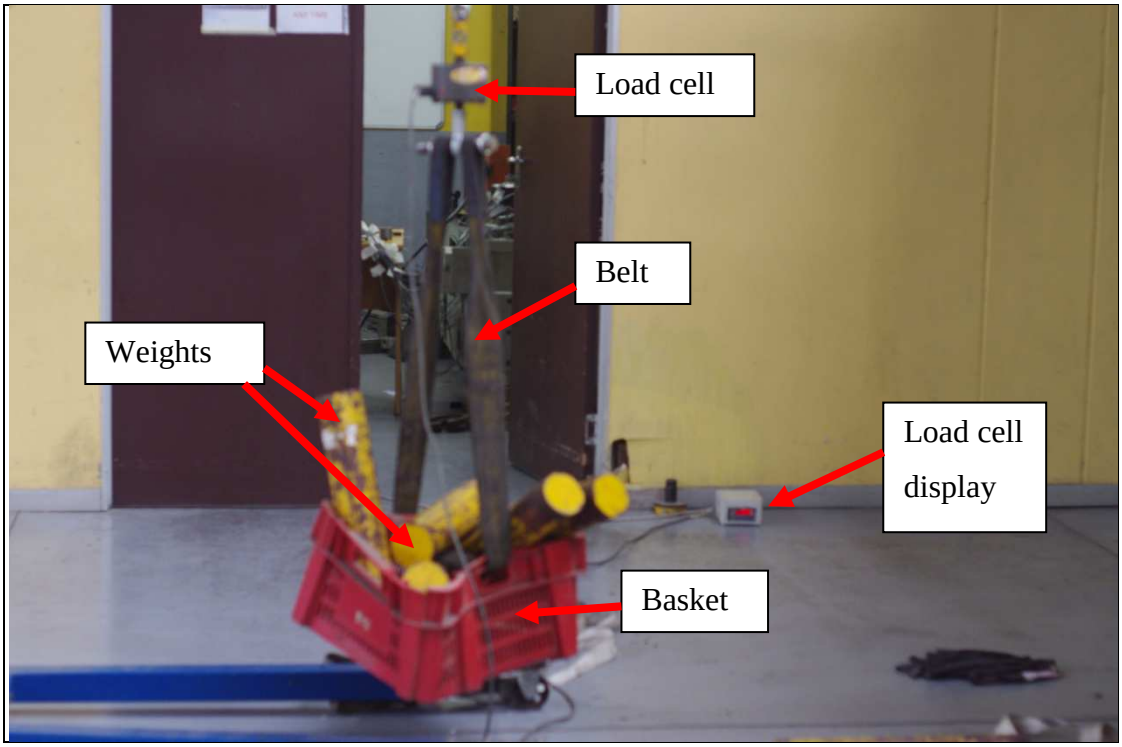


Figure 111. Basket carrying weights applying a load to the load cell.

Table 17. Calibration values for the 50kN load cell.

Description	Total mass [kg]	Load cell reading [kg]
Basket + belt	3.91	4
31.3	35.2	34
31.25	66.5	68
31.3	97.8	100
31.4	129.2	131
31.4	160.6	162
31.4	192	193
31.4	223.4	225
31.5	254.9	255
31.4	286.3	288

Figure 112 shows the calibration graph together with a linear trendline. The trendline indicates what the load cell will display if a given mass is applied.

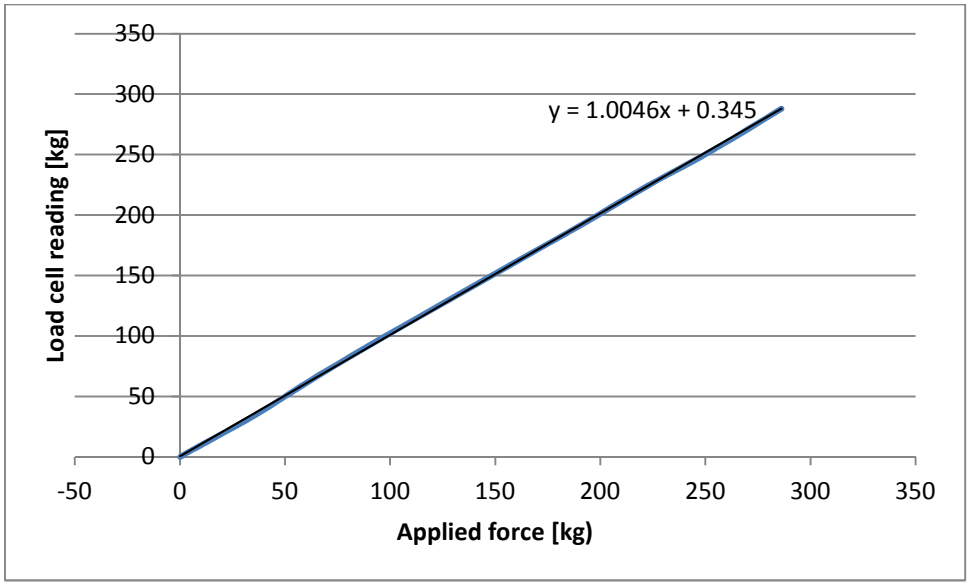


Figure 112. Calibration curve for the 50kN load cell.

More importantly, to know what the actual force is when a value is read off the load cell display, the axes were simply inverted and the equation y = 0.995x – 0.33 was obtained. This means that if the load cell reads 100kg for example, then the actual load will be y = 0.995(100) – 0.33 = 99.17kg. This allows for adjusting the load until the correct loading is applied.

Appendix C Ply Overlap

Ply overlap occurs when two adjacent plies are mounted on each other as shown in Figure 113.

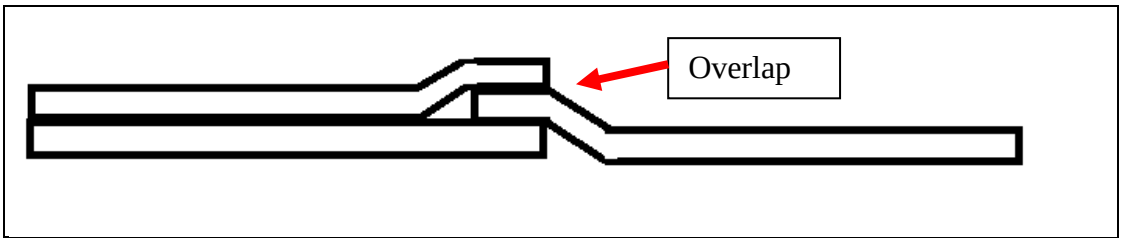


Figure 113. Schematic of plies overlapping each other.

This method was not used when creating the finite element model in ANSYS Composite due to the difficulty of modelling the overlap. Therefore in the areas where ply overlap exist, the method used was to model the adjacent plies as shown in Figure 114.

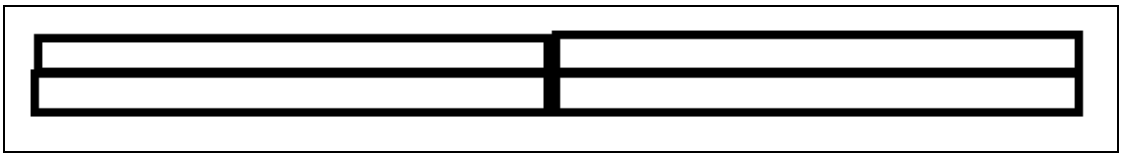


Figure 114. Adjacent plies without ply overlap.

Appendix D Strain Gauge Positions and NI Data Acquisition System

The following figures show the positioning of the strain gauges.



Figure 115. Strain Gauge 1

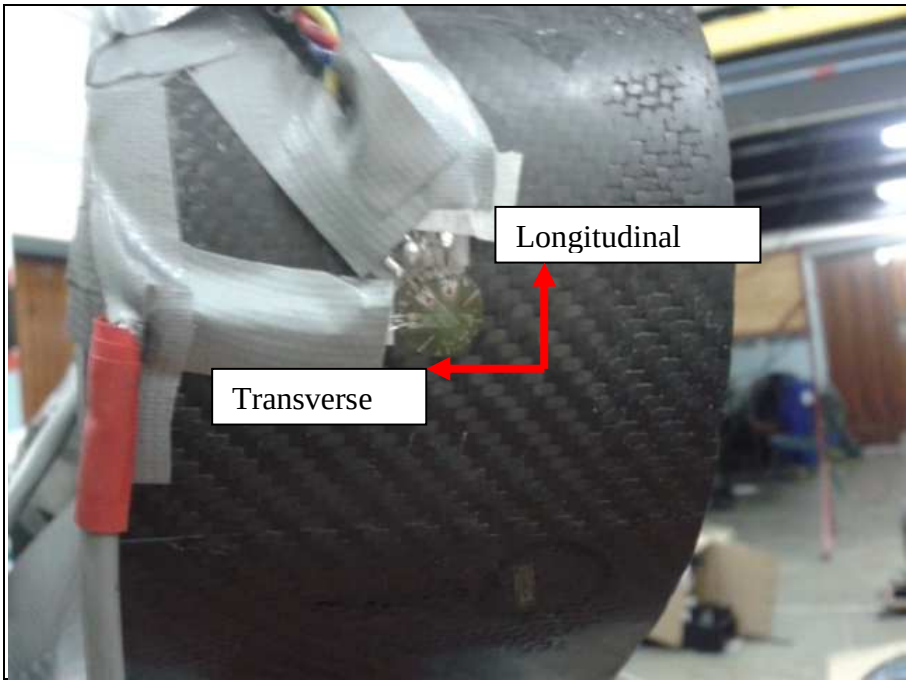


Figure 116. Strain Gauge 1.



Figure 117. Strain Gauge 2.

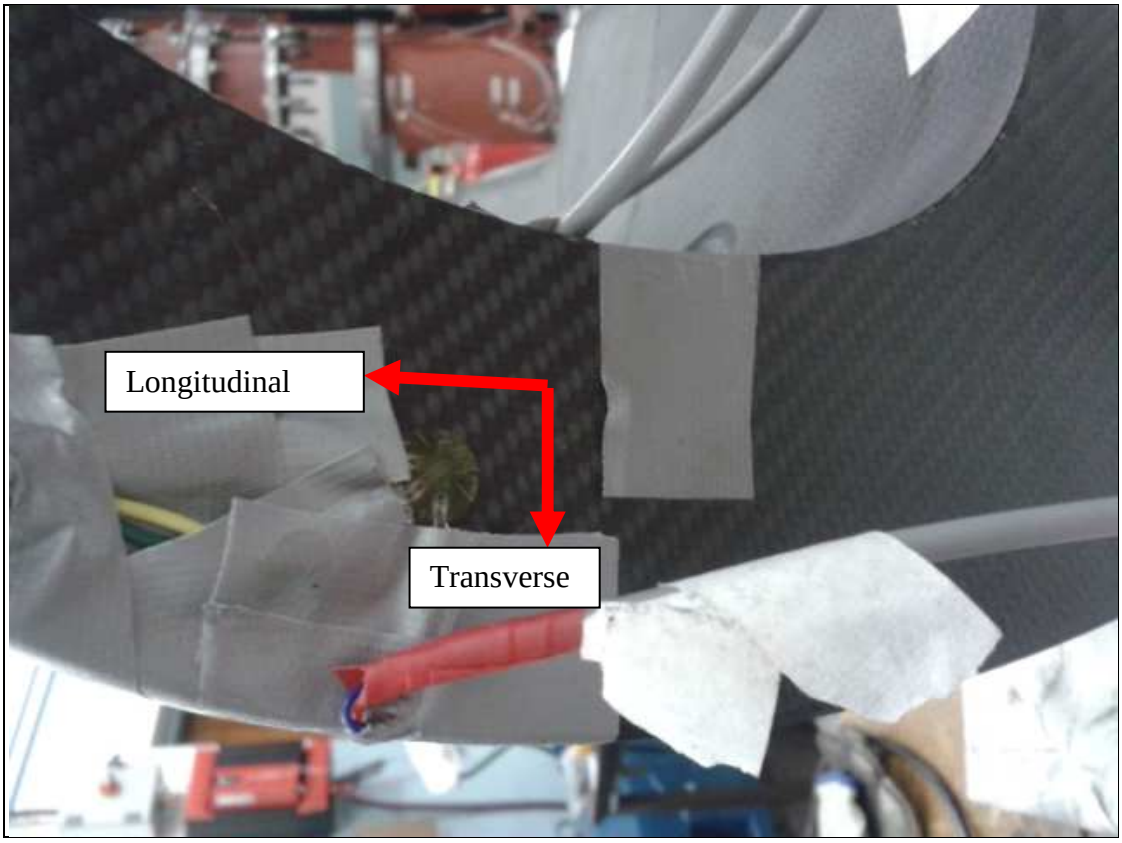


Figure 118. Strain Gauge 2.

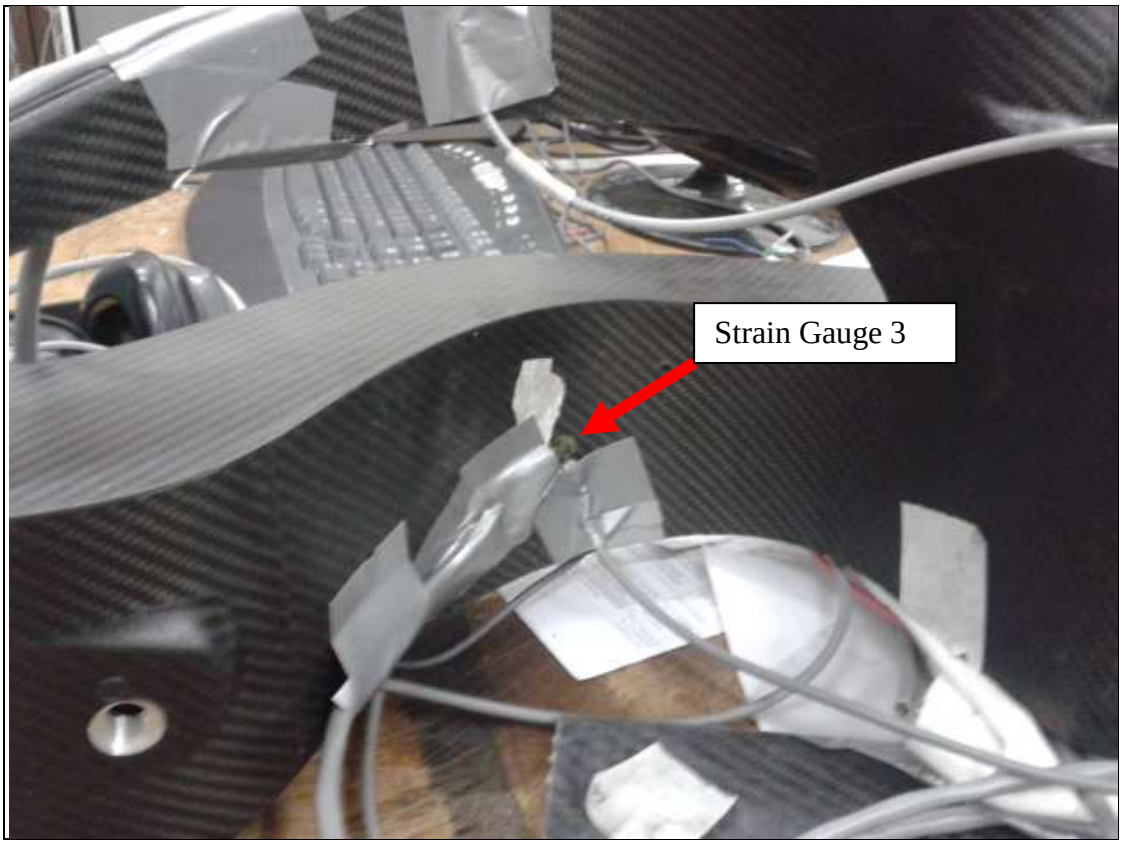


Figure 119. Strain Gauge 3.

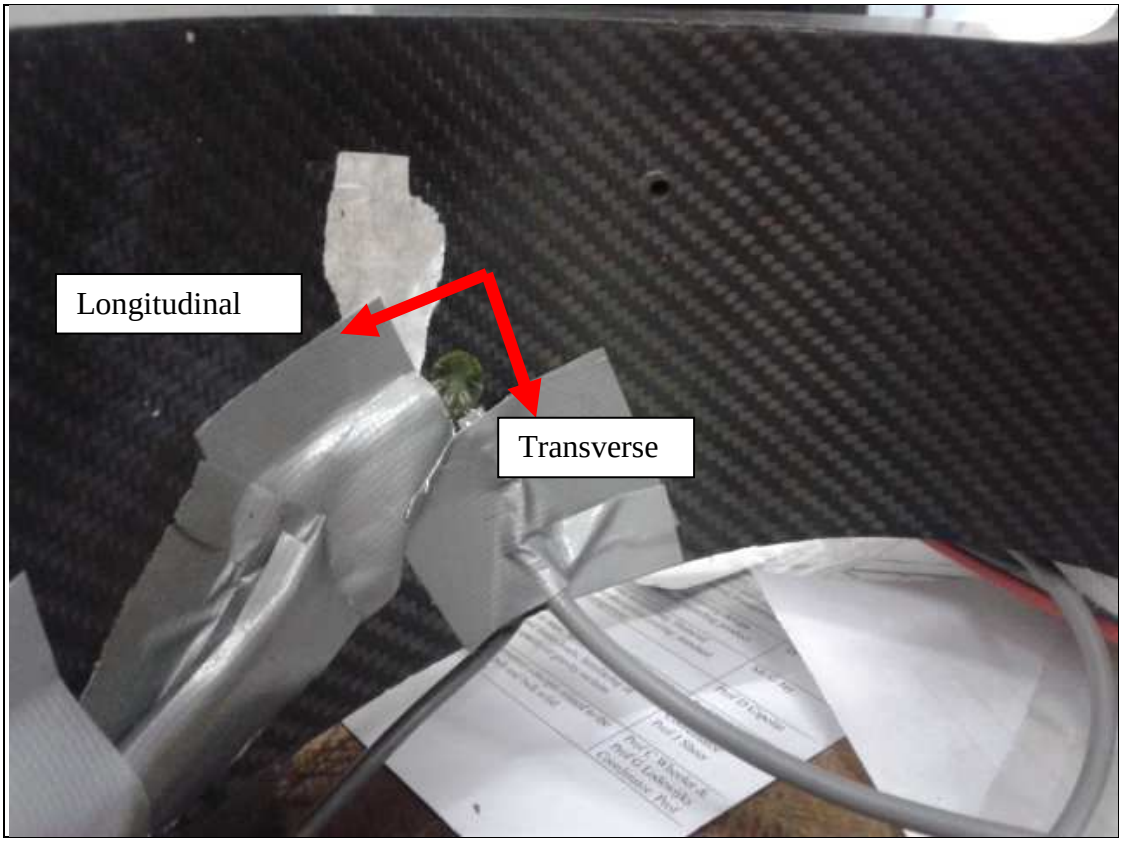


Figure 120. Strain Gauge 3.

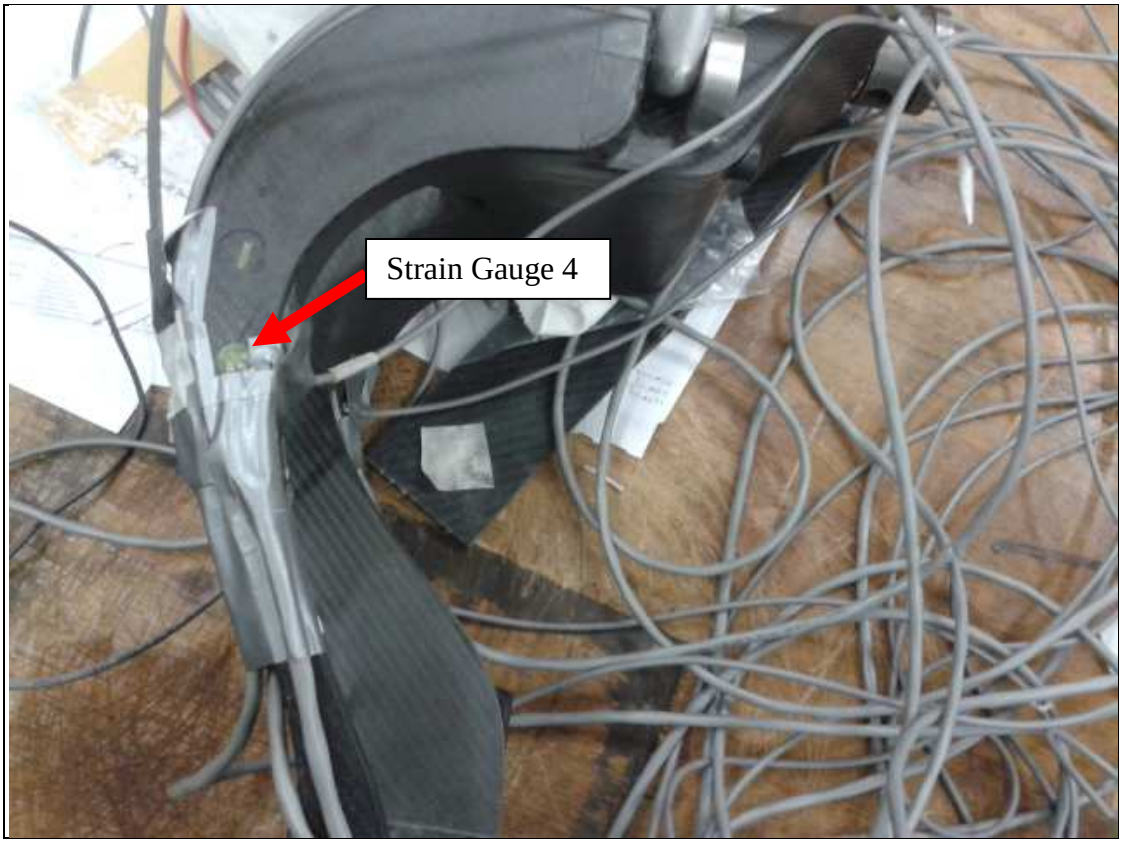


Figure 121. Strain Gauge 4.

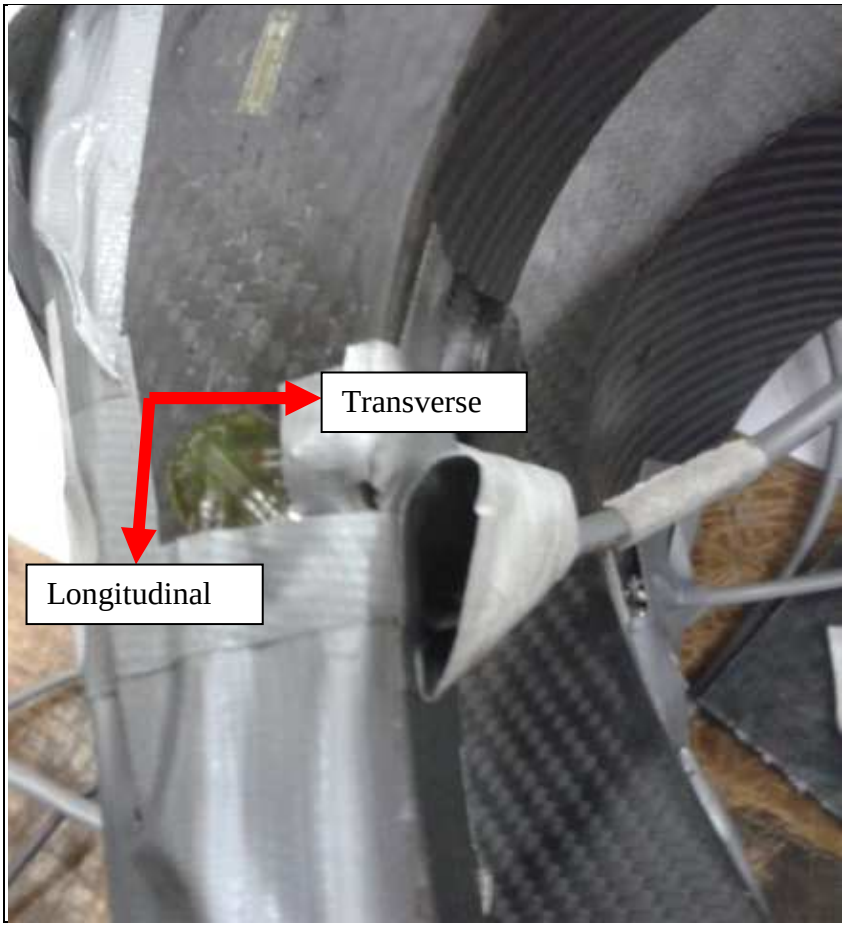


Figure 122. Strain Gauge 4.

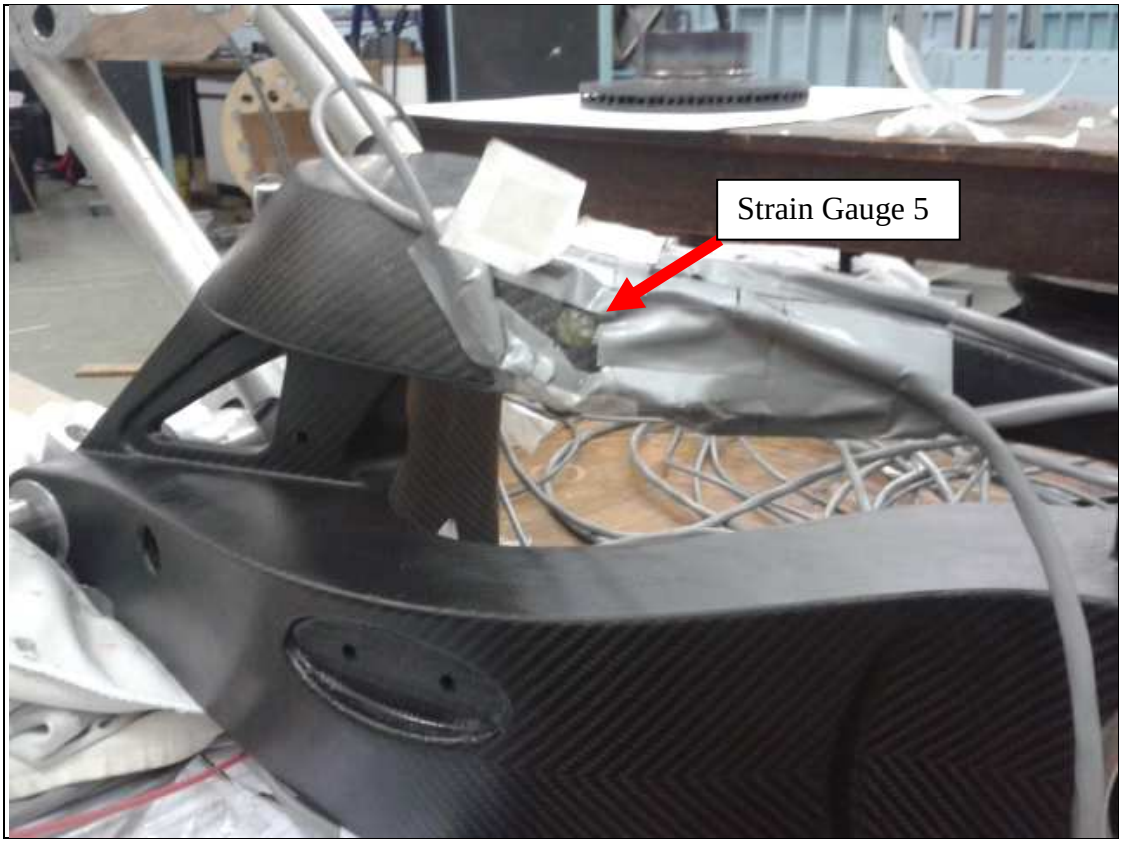


Figure 123. Strain Gauge 5.

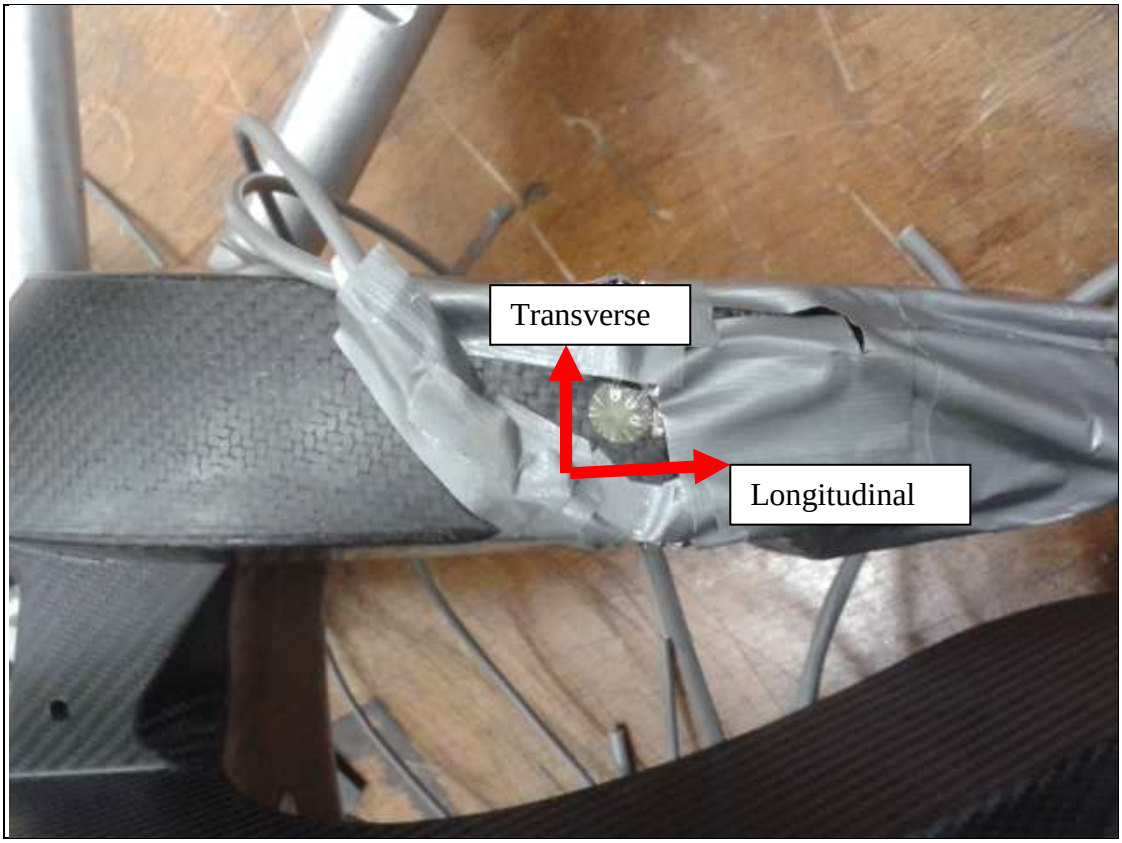


Figure 124. Strain Gauge 5.



Figure 125. Strain Gauge 6.

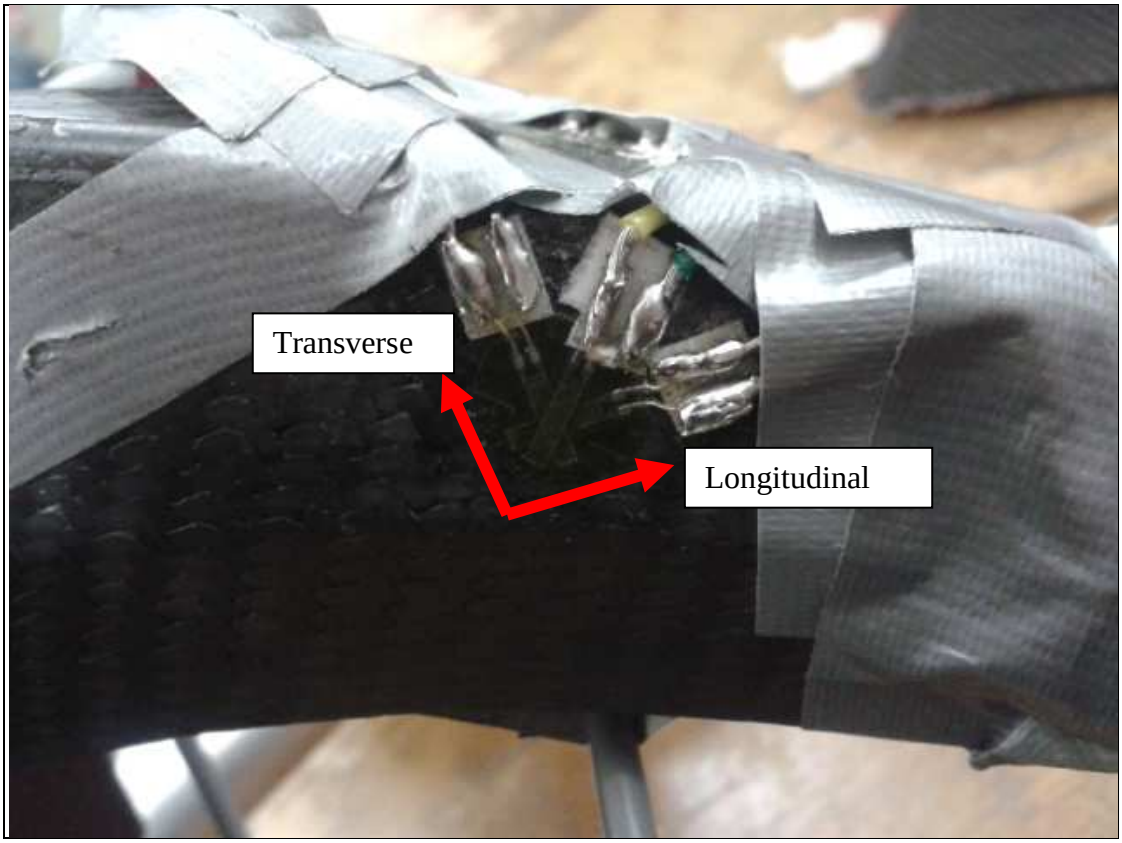


Figure 126. Strain Gauge 6.

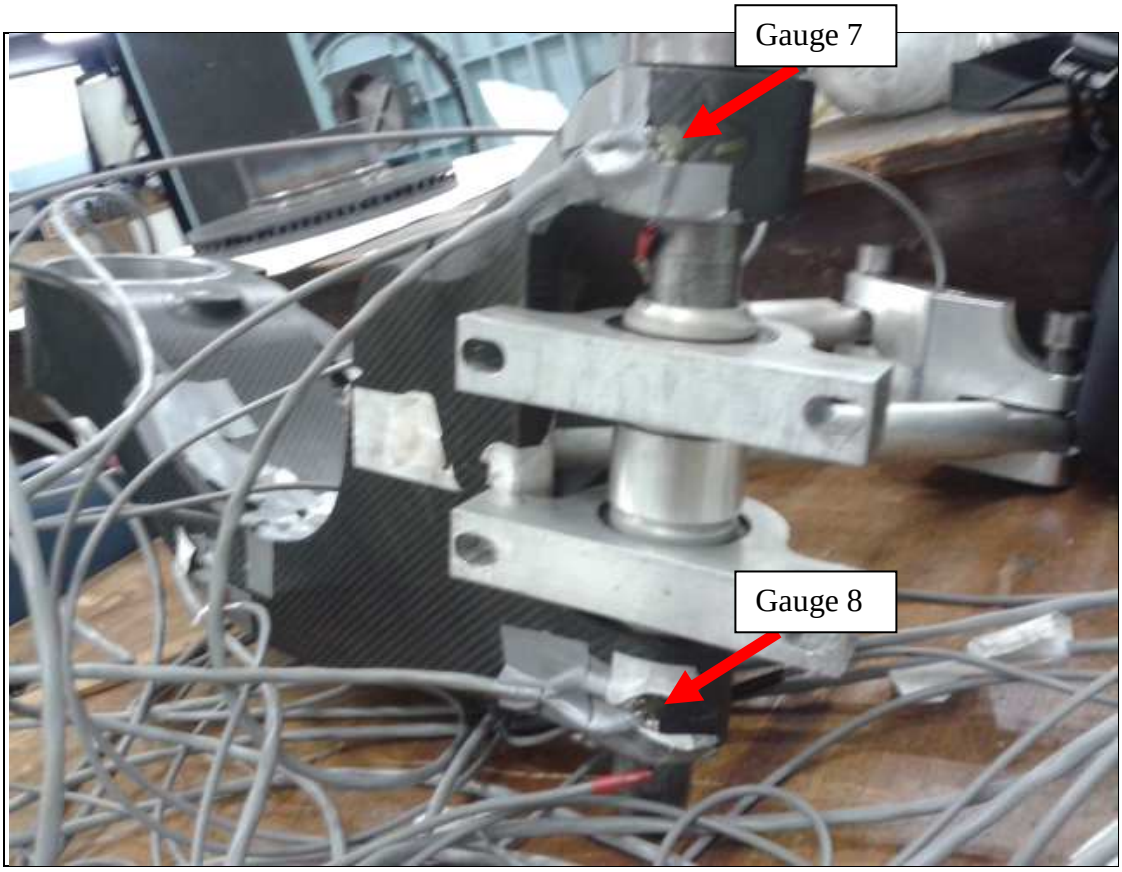


Figure 127. Strain Gauges 7 & 8.

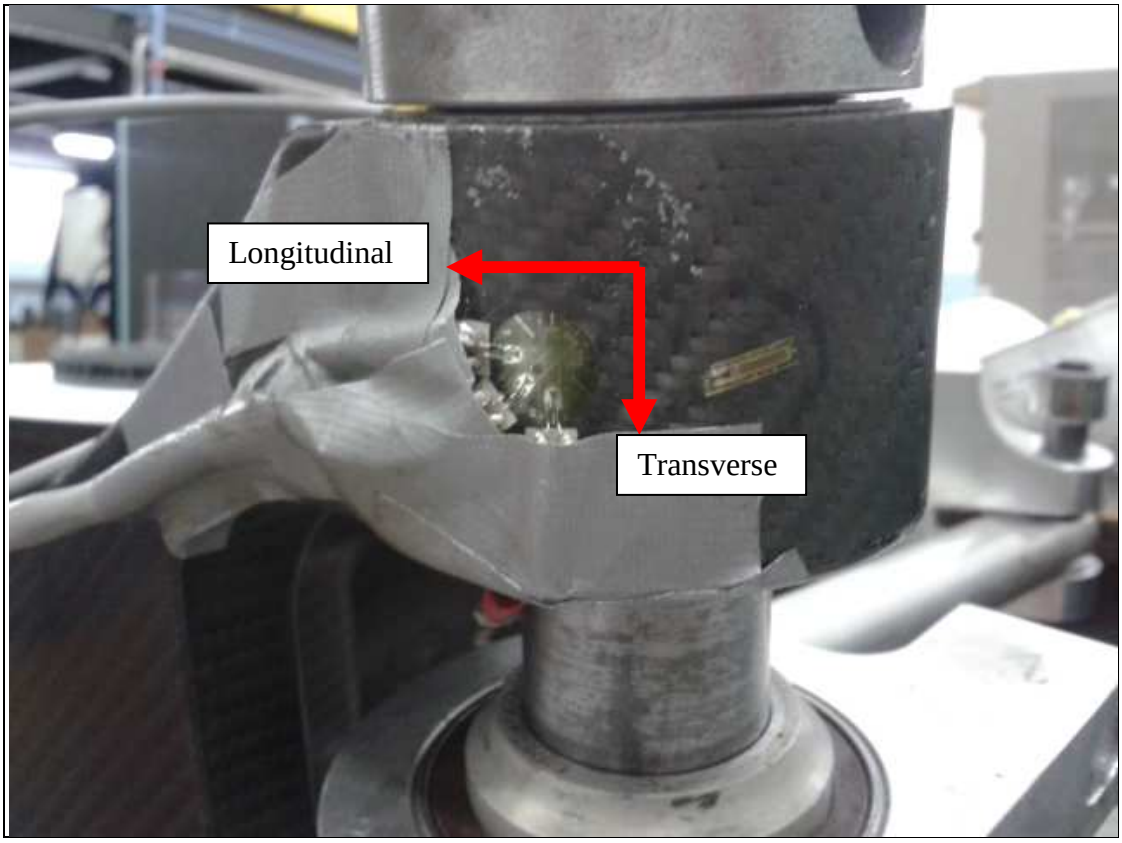


Figure 128. Strain Gauge 7.

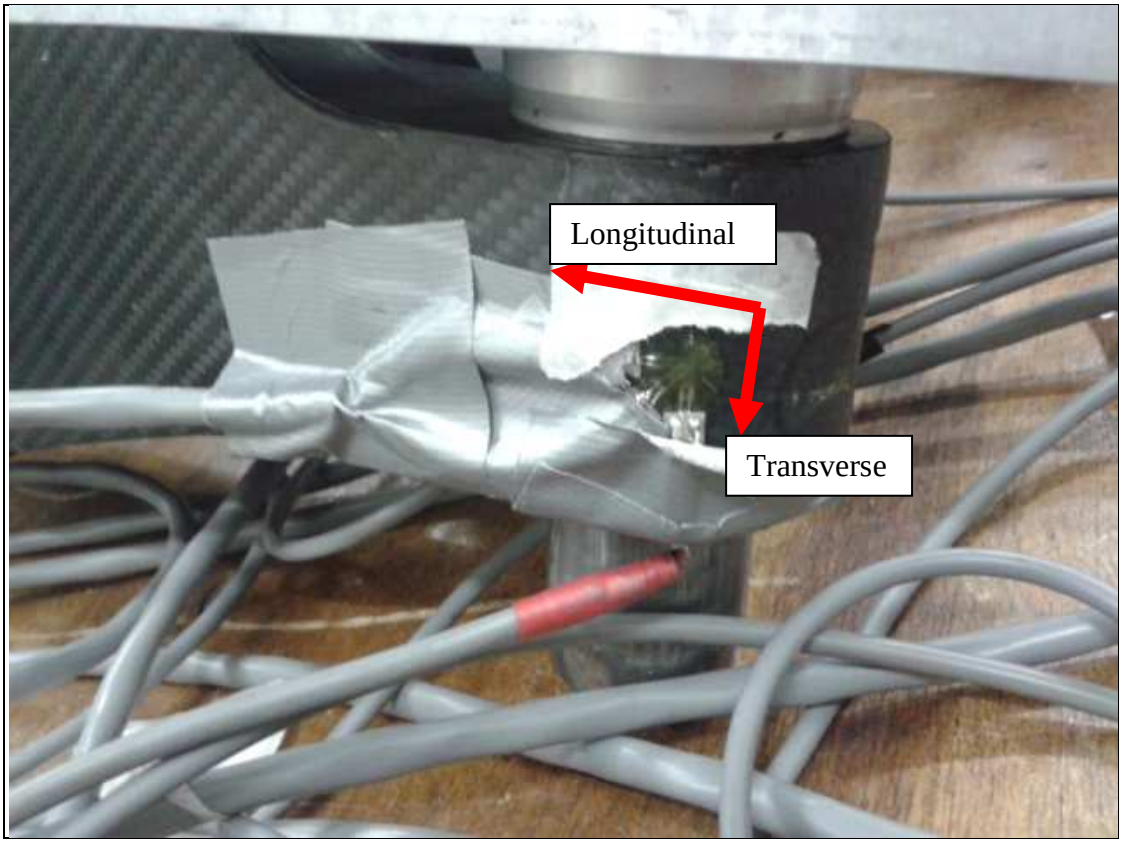


Figure 129. Strain Gauge 8.

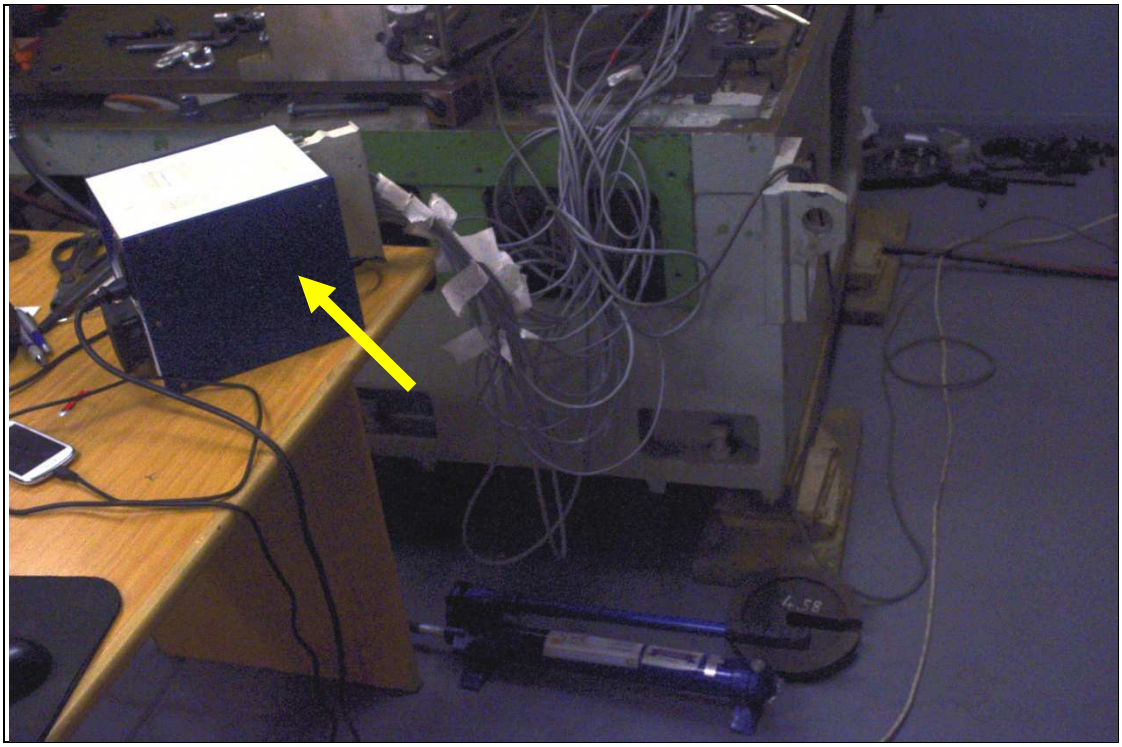


Figure 130. NI data acquisition system connected to the strain gauges on the swingarm.

Appendix E Test Rig Modification Calculations and Drawings

The design and manufacture of the test rig can be seen in Chacko [37]. However modifications were made to the rig in order to apply torsional loading. A steel shaft was designed that would act as a moment arm to apply a moment to the wheel mount of the swingarm. The arm would be subjected to a maximum load of 2000 N at the top end. The length of the arm from the load application point to the top of the wheel mount is approximately 250 mm. Therefore the maximum moment calculated at the wheel mount is given in Equation A.1

$$\begin{aligned} M &= Fd \\ &= 2000 \times 0.25 \\ &= 500\ Nm \end{aligned} \tag{A.1}$$

The maximum bending stress in the shaft is calculated in Equation A.2.

$$\sigma = \frac{My}{I} \tag{A.2}$$

$$\begin{aligned} &= \frac{My}{\frac{\pi d^4}{64}} \\ &= \frac{(500)(0.3)}{\frac{\pi(0.6)^4}{64}} \\ &= 235.7\ MPa \end{aligned}$$

Where: σ = Stress due to bending [MPa]

y = Maximum distance from neutral axis [m]

I = Second moment of area of shaft [m^4]

d = Diameter of shaft [m]

The maximum stress of 235.7 MPa is below the yield strength of 250 MPa for steel therefore the shaft is thick enough. The design drawings of the shaft is shown in Figures 131 to 133.

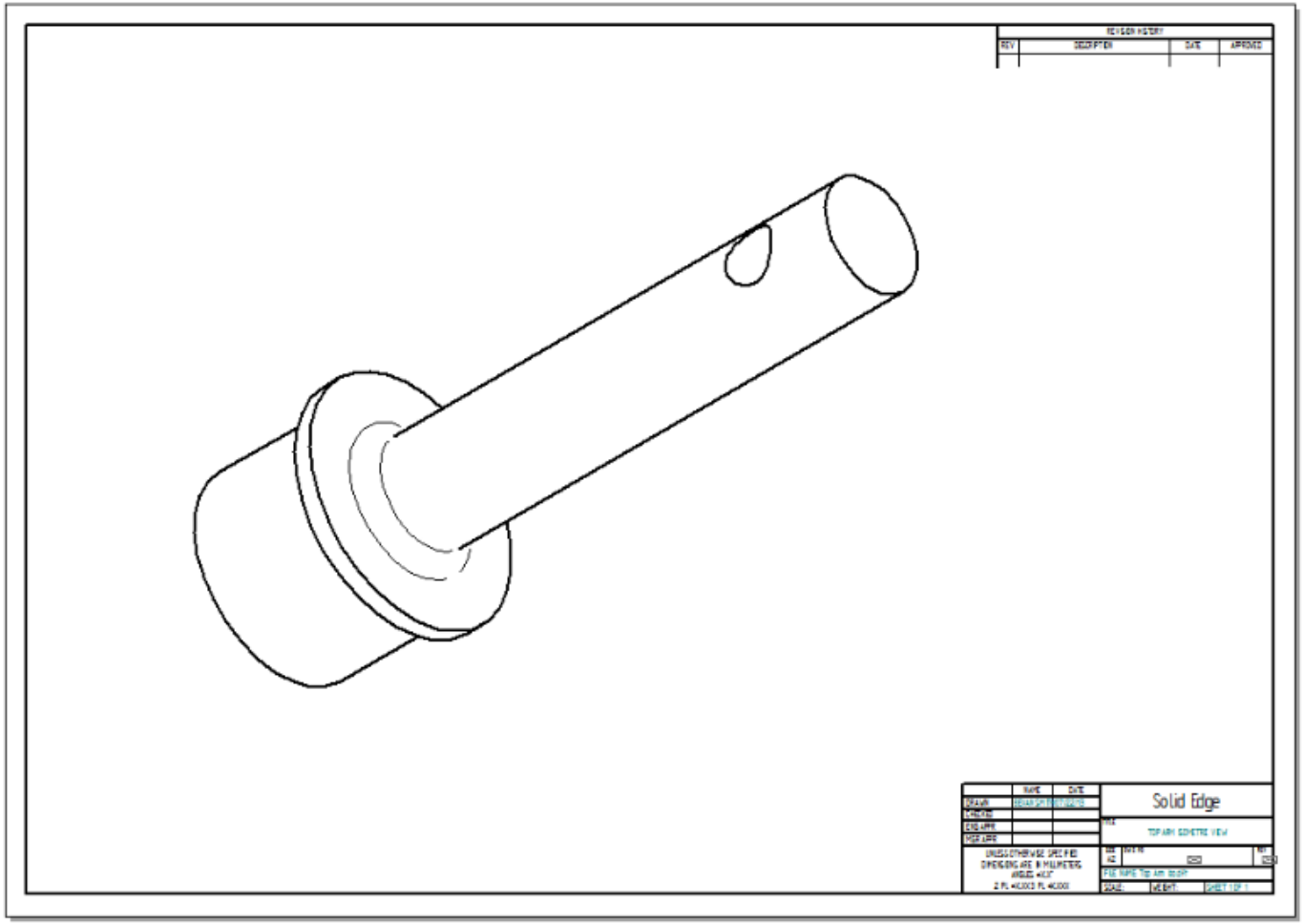


Figure 131. Isometric view of the top part of the steel shaft.

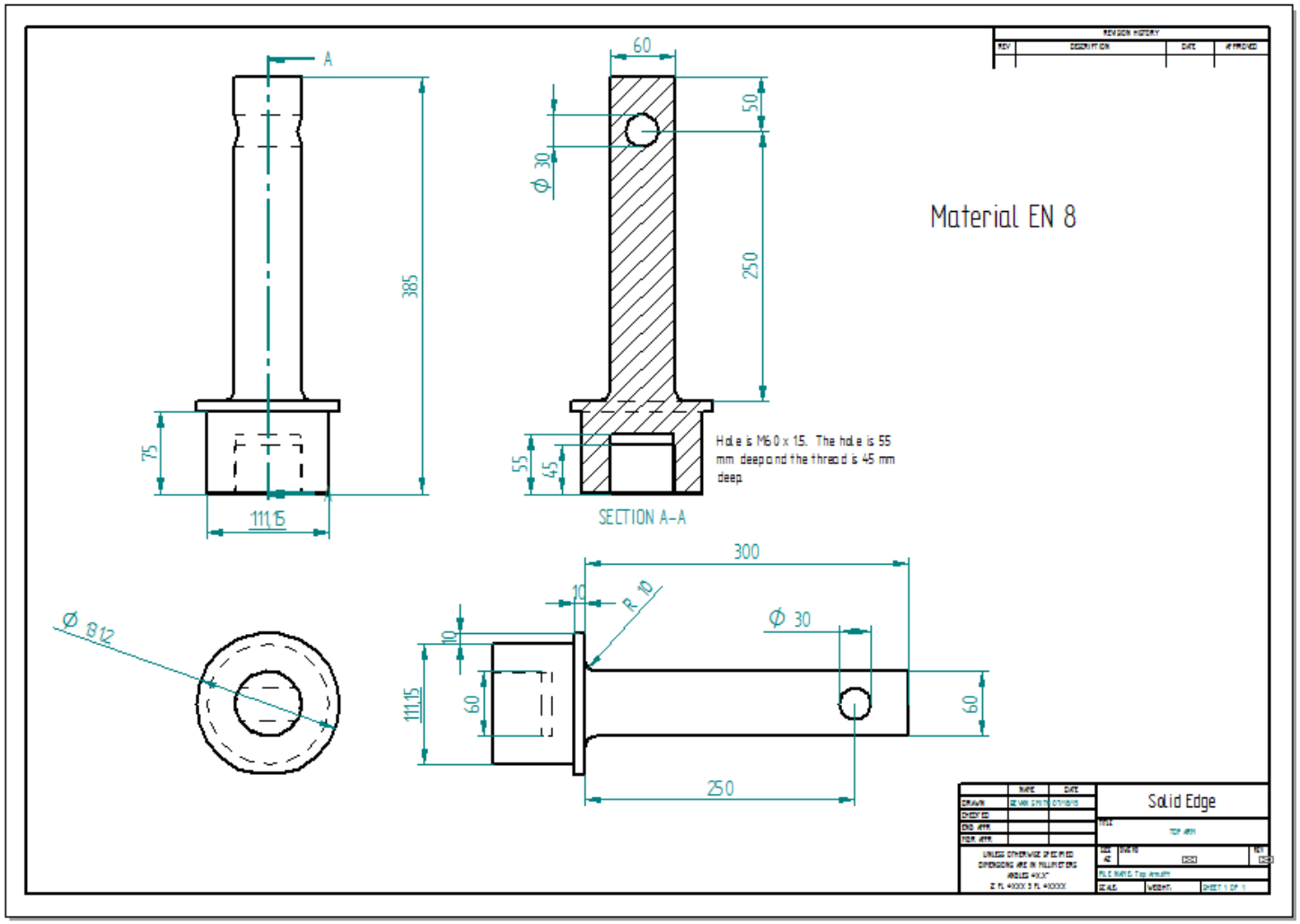


Figure 132. Top part of the steel shaft.

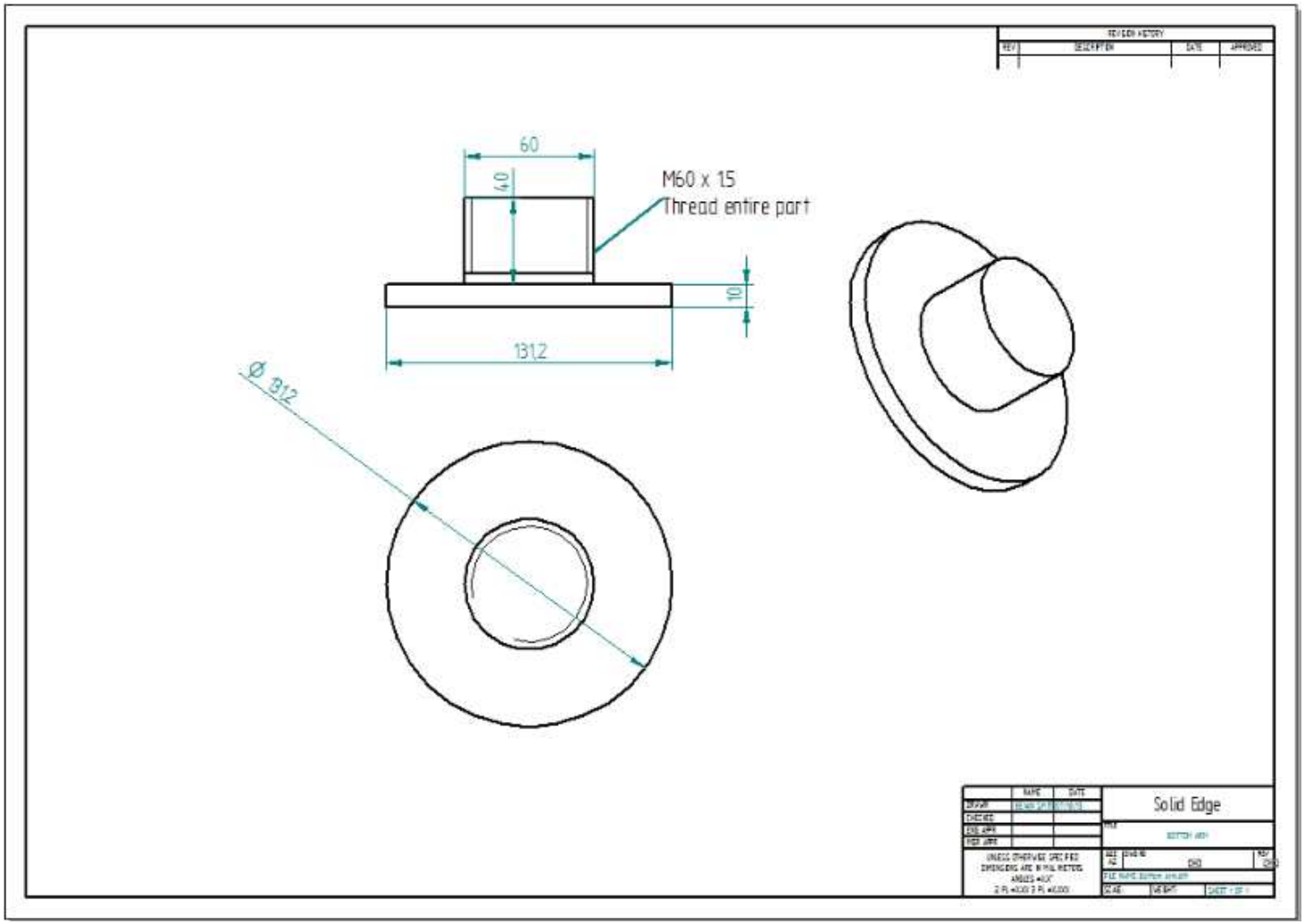


Figure 133. Bottom part of steel shaft.

Appendix F Mesh Dependency

The effect that the mesh has on the results is presented in this section. Figures 134 to 136 present the strain at Position 4 on the finite element model at decreasing element sizes. Figure 134 shows a strain of -1164 $\mu\varepsilon$ using element sizes of 5 mm.

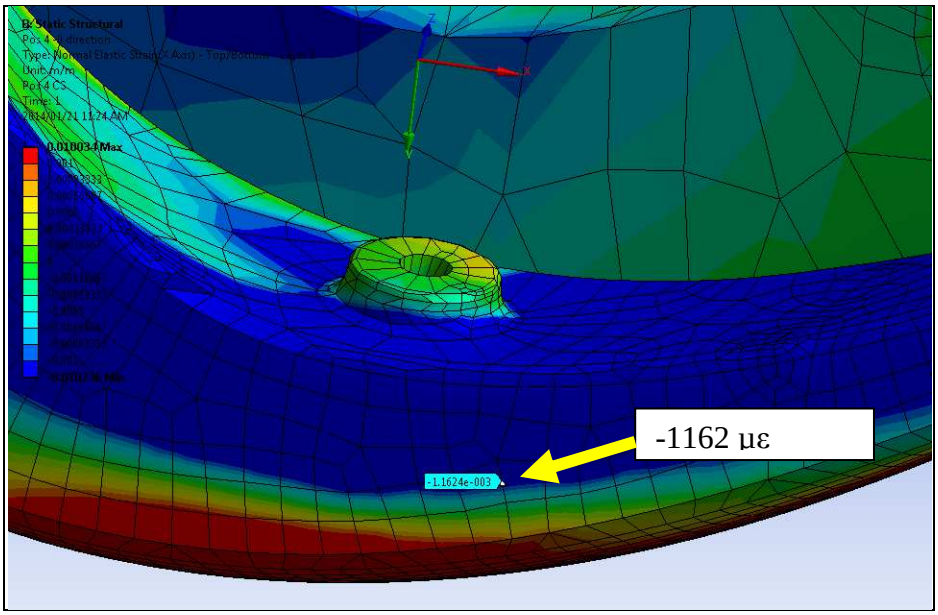


Figure 134. Position 4 with element size of 5 mm.

Figure 135 shows strain of -1164 $\mu\varepsilon$ at Position 4 using element sizes of 3 mm.

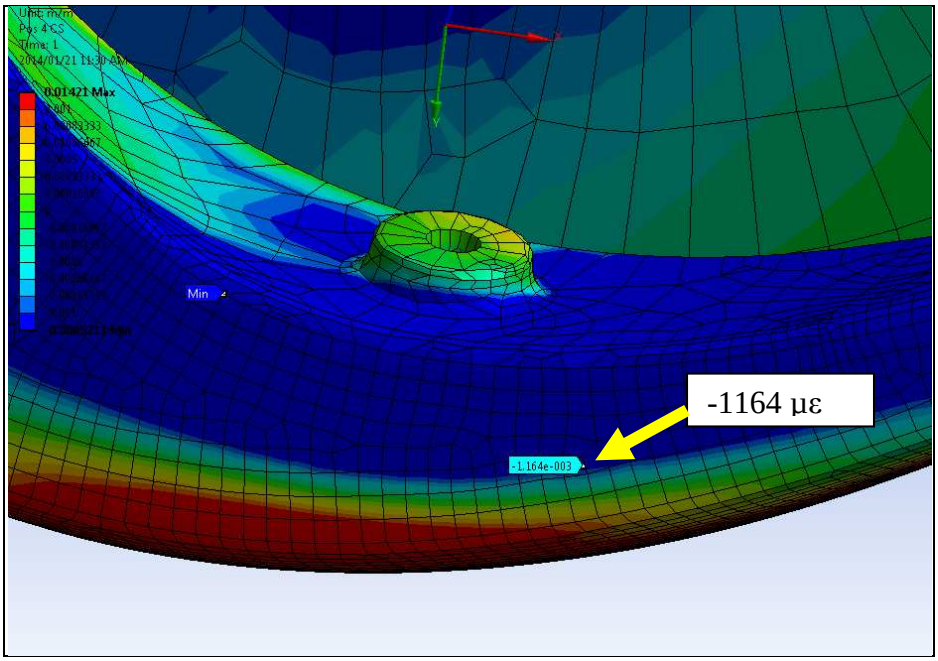


Figure 135. Position 4 with element size of 3 mm.

Figure 136 shows strain at Position 4 of -1162 με with an element size of 1 mm.

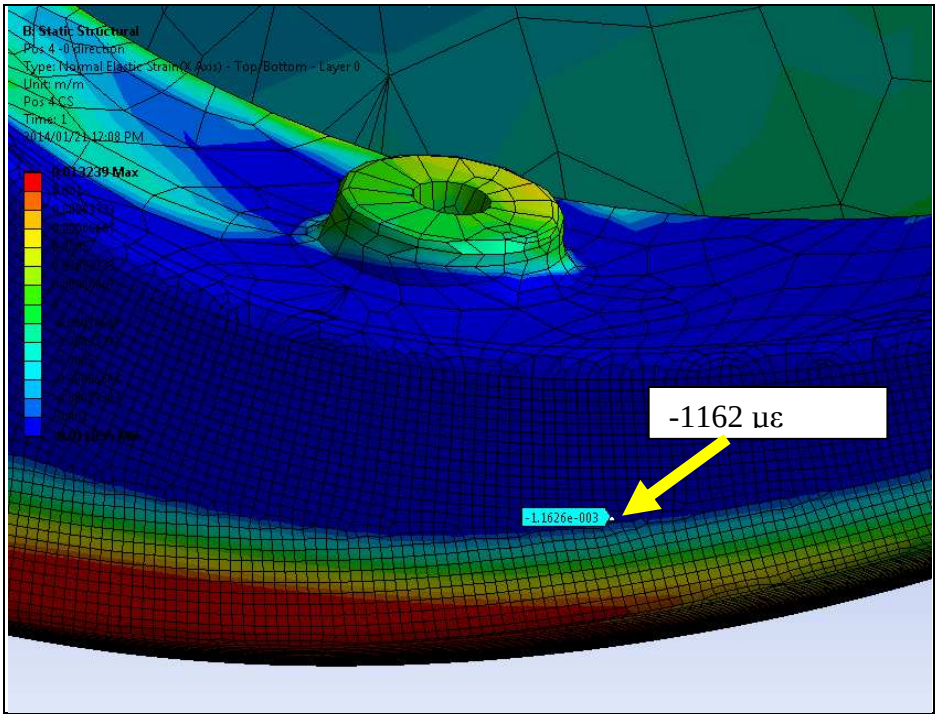


Figure 136. Position 4 with element size of 1 mm.

It can be seen that as the mesh is refined, the results do not significantly change (Table 18). The percentage difference between the strain using element sizes of 5 mm and 3 mm is ((1162-1164)/1162) x 100 = -0.172 % which is negligible. The percentage strain difference between the 3 mm and 1 mm element size mesh is ((11640-11626)/1164) x 100 = 0.12 % which also is negligible. This exercise shows the results are mesh independent.

Table 18. Mesh sensitivity.

Element size [mm]	5	3	1
Strain [με]	1162.0	1164.0	1162.6